NONLINEAR EVOLUTION OF OCEAN EXTREME WAVES OVER VARYING BATHYMETRIES

QIAN WU

PhD

The Hong Kong Polytechnic University

This programme is jointly offered by The Hong Kong Polytechnic University and Southern University of Science and Technology

2024

The Hong Kong Polytechnic University

Department of Civil and Environmental Engineering

Southern University of Science and Technology

Department of Ocean Science and Engineering

Nonlinear Evolution of Ocean Extreme Waves over Varying Bathymetries

Qian WU

A thesis submitted in partial fulfilment of the requirements for the degree of Doctor of Philosophy

September 2024

CERTIFICATE OF ORIGINALITY

CERTIFICATE OF ORIGINALITY

I hereby declare that this thesis is my own work and that, to the best of my knowledge and belief, it reproduces no material previously published or written, nor material that has been accepted for the award of any other degree or diploma, except where due acknowledgement has been made in the text.

__________________________**(Signed)**

Qian WU **(Name of student)**

ABSTRACT

The incidence of anomalously large waves in coastal regions poses serious coastal hazards, particularly to coastal structures and human activities. Of scientific research interest is the formation mechanism of these extreme ocean waves. One of the mechanisms is believed to be the nonlinear wave evolution over abrupt depth transitions (ADTs) in the bathymetry. To elucidate the role of ADTs in triggering extreme waves, it is important to investigate the strong nonlinear wave-wave and wave-bathymetry interactions for large waves. However, few studies have been found in the literature to investigate the nonlinearity of extreme waves over varying bathymetries. Existing linear or weakly nonlinear models may not be able to reveal strongly nonlinear effects. This motivates the development of more advanced models to deal with such problems. This thesis aims to develop a fully nonlinear numerical model to describe the highly nonlinear evolution of waves over varying bathymetries and to investigate the characteristics of higher harmonic elevations induced by bathymetry. A temporal and spatial analysis framework for subharmonics and superharmonics of wave elevations is employed. Focused wave groups, typical representative extreme wave conditions, are adopted in this thesis as the incident

wave.

In the past decade, fully nonlinear numerical models have been developed to confirm that abrupt depth changes can modify the statistical distribution of surface elevations. However, few of them studied the characteristics of each harmonic on the water depth transitions. In addition, most topographies are limited to simplified shapes, such as slopes and infinite steps. To address these issues, an efficient solution framework to the two-dimensional Euler equations by a conformal mapping method is developed, which eliminates the singularity at the corners of the sudden changes. This numerical model is capable of demonstrating nonlinear wave propagation in both temporal and spatial domains. Specifically, it facilitates the evolution of extreme waves and their interaction with the bathymetry. To validate the model, experiments were conducted at the laboratories of the Hong Kong Polytechnic University and the Southern University of Science and Technology. Comparisons of the surface elevation, energy spectrum and wave scattering (wave reflection and transmission) show high confidence in its capability and accuracy.

Significant second-order effects have been identified in the mechanism of occurrence of extreme waves. However, the study of second-order subharmonics and superharmonics (bound and free waves) at ADT is few. Thus, through the experimental and numerical study in this thesis, a detailed evolution of the second-order harmonic elevation is demonstrated. The second-order subharmonics and superharmonics are separated to assess their contributions to the statistical distribution. Additionally, the effects of parameters such as wave steepness and relative wavelength of both the monochromatic and extreme waves are further illustrated. Generation of higher harmonics in the shallower region on the ADT step is demonstrated, where a high asymmetry of surface elevations on the upstream junction is observed. Subharmonics occur due to the increase of mean water level, on the contrary, they weaken the asymmetry of wave profiles. The total increase of kurtosis interprets a physical formation mechanism for a higher probability of extreme waves at ADTs. Results also reveal energy transfer among superharmonics as well as between the subharmonics and superharmonics on the water depth transitions.

With particular bathymetries and wave conditions, there might occur extremely low or high reflection, corresponding respectively to wave trapping and Bragg resonance. These features have been adopted in the design of breakwaters and were studied widely with regular and random waves. However, the resonance of extreme waves and their nonlinear evolution across the entire spatial domain remains largely unexplored. Thus, the wave trapping with monochromatic waves and the Bragg resonance with focused wave groups are investigated in this study. The fully nonlinear numerical model is first validated by linear theories and experimental data in the study of wave resonance. The nonlinearity at the trapped frequencies obtained from the linear model is assessed. Unlike the importance of kurtosis at ADTs, the skewness can be a significant parameter in discussing trapped wave progress. Then, the focused wave propagation over three types of periodic bottoms is simulated, namely ripples, bars, and steps. The optimal conditions of high Bragg reflection are proposed. Nonlinear analysis of the reflection coefficient confirms the existence of a secondary Bragg resonance.

Overall, this research provides methodologies to assess the hydrodynamic characteristics of extreme waves over varying bathymetries. Compared with the traditional numerical models, the developed fully nonlinear numerical model presents the complete interplay between waves and transitions with a very high efficiency. Laboratory experiments validate the simulation results and add measured data to the literature. From the perspective of subharmonics and superharmonics, the analyzed results provide more insights into the mechanism of extreme wave generation. Additionally, the findings highlight the occurrence of Bragg reflection over different topographies and could make contributions to the design of coastal breakwaters and improvement of the potential detection in the future.

PUBLICATIONS ARISING FROM THE THESIS

Academic Journal Papers

Published article

Wu, Q., Feng*, X., Dong, Y., and Dias, F. (2023). “On the behavior of higher harmonics in the evolution of nonlinear water waves in the presence of abrupt depth transitions”. *Physics of Fluids* 35.12.

Zhu, D., Zhang, J., **Wu**, Q., Dong*, Y., and Bastidas-Arteaga, E. (2023). “Predictive capabilities of data-driven machine learning techniques on wave-bridge interactions”. *Applied Ocean Research* 137, p. 103597.

Under review or preparation

Wu, Q., Feng*, X., and Dong, Y. (2024a). “Nonlinear evolution of extreme waves over abrupt depth transitions”. *(In preparation)*.

Wu, Q., Feng*, X., Dong, Y., and Cui, J. (2024b). “Nonlinear propagation of focused wave groups over two sudden depth transitions”. *(Under review)*.

Wu, Q., Feng*, X., Dong, Y., and Ning, D. (2024c). “Bragg reflection of a focused wave group over periodic bars using a fully nonlinear simulation”. *(Under review)*.

Conference paper

Wu, Q and Dong, Y and Feng*, X. (2024). “Bragg resonance study of focused waves over periodic bottoms”. *Proceedings of the 35rd National Conference on Hydrodynamic (NCHD 2024)* (Aug. 02–05, 2024). NCHD. Harbin, P.R. China, pp. 187–191.

Wu, Q., Dong, Y., and Feng*, X. (2023a). “Experimental and numerical study of focused wave groups propagating over sudden depth transitions”. *Proceedings of the 34th National Conference on Hydrodynamic (NCHD 2023)* (Oct. 27–30, 2023). NCHD. Ningbo, P.R. China, pp. 1394–1400.

Wu, Q., Dong, Y., and Feng*, X. (2023b). “Extreme wave statistics of focused wave groups over abrupt depth transitions”. *Proceedings of the 1st PolyU Research Student Conference (PRSC 2023)* (May 8–11, 2023). The Hong Kong Polytechnic University. Hong Kong, P.R. China, pp. 354–359.

Wu, Q., Dong, Y., and Feng*, X. (2023c). “Nonlinear computation for focused wave groups on abrupt depth transitions”. *The 12th International Workshop on Ship and Marine Hydrodynamics (IWSH 2023)* (Aug. 28–Sept. 1, 2023). Vol. 1288. IOP Publishing. Espoo,Finland, p. 012011.

Wu, Q., Dong, Y., and Feng*, X. (2023d). “Numerical simulation and experimental study of nonlinear wave propagation with abrupt depth changes". *Proceedings of the 1st Southern University of Science and Technology Graduate Academic Conference* (Mar. 18–19, 2023). Southern University of Science and Technology. Shenzhen, P.R. China, pp. 354–359.

Wu, Q and Dong, Y and Feng*, X. (2022a). "Numerical and experimental study of trapped waves propagation over a submerged step". *Proceedings of the 33rd National Conference on Hydrodynamic (NCHD 2022)* (Oct. 38-31, 2022). NCHD. Chongqing, P.R. China, pp. 354-359.

Wu, Q and Dong, Y and Feng*, X. (2022b). "Numerical Study of Trapped Waves Propagation over a Submerged Step". *International Ocean and Polar Engineering Conference (ISOPE 2022)* (June 5-10, 2022). ISOPE. Shanghai, P.R. China, pp. 2671-2677.

ACKNOWLEDGEMENTS

First and foremost, I would like to express the highest appreciation to my supervisor Dr. Xingya Feng, for his professional guidance, endless support, patience and kind care during my PhD study. He is always patient in carefully checking the thesis work in every meeting and is generous in providing specific suggestions for each point that I feel puzzled about. His enthusiasm, keen insight and gorgeous guidance always inspire me to pursue the essential research I should do. I am so lucky to have such a responsible and nice supervisor and sincerely grateful for his supervision and encouragement. Without his guidance and support in my PhD study, the thesis work would not be possible. His great quality and morality will also benefit my lifetime.

Next, my earnest thanks must go to Dr. You Dong, my supervisor for his invaluable advice, guidance and encouragement through my research study. His rigorous attitude and creative thinking towards academic research set an example for me to pursue to be a well-educated researcher. Without his immense patience and dedication to my research, I would not have had the chance to reach a higher level of education. Special thanks to Dr. Denys Dutykh, and Prof. Wooyoung Choi for sharing the details and suggestions on the establishment of the numerical model. I am grateful for their patience and encouragement to a fresh PhD student, their selfless guidance created a positive research atmosphere for me.

Then, I would like to thank Dr. Deming Zhu for his guidance on laboratory experiments and revision of the article. His rich expertise guides me to solve many problems and refine my work. Besides, I would like to thank Mr. K.H. Leung for his technical assistance during the experiments. My gratitude also goes to Prof. Lin Lv, my supervisor for my master's study and Dr. Yi Liu, my supervisor for my bachelor's degree. They bring me across the threshold of research and give unconditional support to my research. Special thanks go to PhD fellows in our groups, Dr. Peng Yuan, Dr. Qunbin Chen, and Dr. Junnan Cui for their guidance in the mathematical model and improvement of the quality of thesis work. I also want to thank the opportunities given by the Southern University of Science and Technology and Hong Kong Polytechnic University for my incredible doctoral journey. I would also like to thank my colleagues and friends in mainland and Hong Kong in my PhD life for their warm support and friendship throughout my entire study process, including Mses. Yaohan Li, Menghan Zhao, Dan Wu, Liu Yang, Fangxin Li, Qijiao He, Xiaoying Li, Zhenlu Yu, Yuyu Qin, Jingyi Zhang, Xialu Liu, and Messrs. Siyuan Zhao, Jing Qian, Hongyuan Guo, Ruiwei Feng, Ghazanfar Ali Anwar, Fuhao Deng, Li Lai, Jiaxin Zhang, Dengshuo Chen, Zhiqiang Li, Junpeng Liu, Junru Chen, Lin Yang, Yinwang Yan, Haoheng Luo and many others.

Finally, I am grateful to my family and boyfriend for their unconditional support, love and encouragement throughout my life. Having them is the luckiest thing in my life.

CONTENTS

LIST OF FIGURES

LIST OF TABLES

Chapter 1

Introduction

1.1 Background and motivation

The occurrence of abnormally large waves can bring significant coastal hazards, especially for the coastal industry and human activities (Didenkulova et al., 2022). Large extreme waves, also termed ‘rogue’ or ‘freak’ waves, have been more frequently observed and reported in recent years in the background of global climate change (Teutsch et al., 2020). Rogue waves are typically defined as heights more than twice the local significant wave height. For instance, on January 1, 1995, at Statoil’s Draupner gas platform in the North Sea, the “NewYear Wave” was measured by laser to be 25.6 m. Over the past few decades, the mechanism of large wave occurrences in the ocean has attracted significant engineering and scientific interest. Although the causes resulting in extreme waves are numerous, a definite interpretation of extreme wave occurrence is still under investigation.

Water depth is a key parameter for wave propagation in coastal regions (Figure

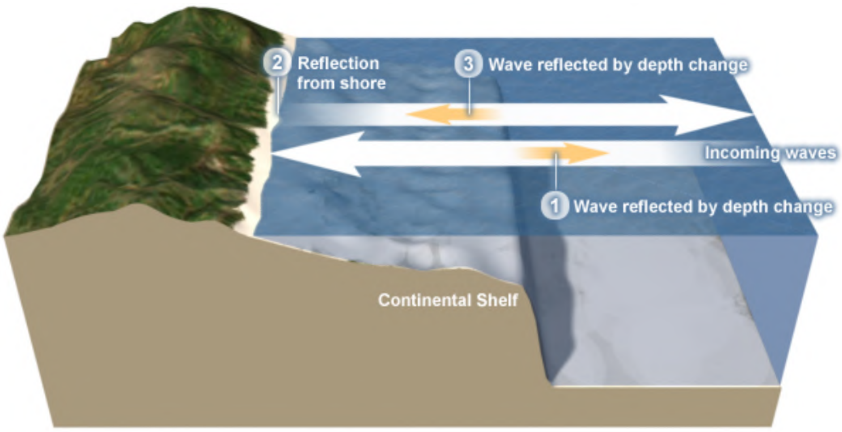

Figure 1.1: A schematic of wave propagation over water depth transitions (Neetu et al., 2011).

1.1). The changes in water depth can be either local, in the form of seamounts and underwater volcanic islands, or continuously changing, such as continental shelves and coastal sandbars (Li and Chabchoub, 2023). Studies of wave evolution over varying bathymetries have been quite active in the past decades. Some studies investigated the wave propagation over the bathymetry with simple shapes, such as the constant slope and infinite step (Majda et al., 2019; Zheng et al., 2020). Most research concentrated on wave scattering over varying bathymetries, especially for the reflection and transmission coefficients of waves (Liu et al., 2013). Recently, the transition in water depth has been certificated as a potential factor in the increased probability of extreme wave occurrences (Gao et al., 2021; Trulsen, 2018). The strong wave nonlinearity induced by ADTs makes the wave profiles highly asymmetric. In particular, the second-order effect of steepness is particularly important in the form of high peaks (Li et al., 2021b), which indicates the potential influence of higher harmonics in extreme wave generation. Therefore, it is necessary to study the propagation of higher harmonics on the depth transitions. The changes in each harmonic component, especially the changes in the second subharmonic and superharmonic, need to be studied in more detail.

Focused wave groups, as a representative of extreme waves, have been recently employed in laboratory studies for studying their influence on coastal structures (Feng, 2019). Due to the complicated wave-wave interaction in nonlinear focused wave evolution, various numerical models have attempted to simulate the nonlinear evolution of focused wave groups in constant water depth, such as the higher-order spectral method (HOSM), Computational Fluid Dynamics (CFD), OpenFOAM, and the Finite Element Method (FEM). Currently, there is a lack of research on the nonlinear focused wave group propagation on transitions. The existing research about the focused wave groups propagation over transitions mainly considered the statistical distribution in space, such as skewness and kurtosis, but overlooked the hydrodynamic performance of higher harmonics during the nonlinear evolution. Thus, investigating the focused wave group propagation over ADTs is necessary. Especially, an understanding of the generation and evolution of superharmonic in space can facilitate explaining the mechanism of extreme wave propagation with a higher probability over sudden depth changes.

Furthermore, specific bathymetries can induce wave resonance in the coastal environment, one unique wave type is known as trapped waves (Koshimura et al., 2001). At a certain water depth change, most transmitted waves are trapped in the shallower regions and induce waves with higher crests. Despite the significance of studying such wave resonance in studying abnormal waves, the existing research is limited to long wave theory due to the difficulty in capturing the trapped waves.

Bragg resonance is also a special wave resonance that occurs when submerged bars' wavelength is half that of incident waves (Hsu et al., 2003). The high reflection coefficients of Bragg resonance make the periodic artificial bars applied in the structural design for coastal breakwaters. Various studies have examined the wave scattering of monochromatic and random waves going through the submerged periodic bottoms. The nonlinearity of the surface waves and the submerged bottoms make a difference in the excitation conditions of Bragg resonance and hence induce the frequency shift and Bragg reflection coefficients. However, the existing research is mainly limited to monochromatic and random waves. Studies of Bragg resonance of focused wave groups are few due to the complicated wave-wave and wave-bathymetry interactions. It is more significant to study the hydrodynamic behavior of focused wave groups over periodic bars for the protection of coastal structures.

Given the discussion above, the lack of research on nonlinear focused wave propagation over varying bathymetries motivates us to investigate the topic further. Studying both the monochromatic and focused waves numerically and experimentally provides an insightful understanding of the hydrodynamic performance of superharmonic wave components on depth transitions. The higher-order resonance over multiple and periodic bottoms will be further investigated by considering Bragg resonance and trapped waves. This thesis will elaborate on the nonlinear wave propagation over various submerged bottoms. The ultimate goal is to elucidate the superharmonic generation during the nonlinear wave evolution and the wave resonance of extreme waves over various nearshore transitions.

1.2 Research objectives

The thesis aims to study the nonlinear wave propagation over varying bathymetries using a nonlinear model and experiments. Within the research scope, four primary objectives of the thesis are summarized as follows:

1) ***To develop a fully nonlinear numerical model using the conformal mapping method.***

   A fully nonlinear numerical model is established within an exact Euler equation. Then, the model serves as a robust tool for investigating the evolution of complex phenomena such as wave-wave and wave-bathymetry interactions through numerical simulations.

2) ***To explore the effects of abrupt depth transitions on monochromatic waves.***

   The generation and evolution of superharmonics over abrupt depth transitions are initially examined using monochromatic waves. Wave scattering, including reflection and transmission, is analyzed experimentally and numerically. The variation of superharmonics is described in spatial and temporal domains with different independent variables (e.g. incident wave steepness, relative water depth).

3) ***To study the nonlinear extreme wave propagation over abrupt depth transitions.***

   Focused wave groups are utilized to investigate nonlinear wave propagation induced by ADTs. A series of hydrodynamic performances of focused wave groups are accessed with experimental and numerical methods. Roles of the higher harmonics, especially for the second harmonics (bound and free waves) are illustrated by analyzing their crests and kurtosis.

4) ***To investigate the wave resonance over the bathymetry with periodic ripples, bars and abrupt depth transitions.***

   This research extends its scope to numerically investigate the wave resonance referring to the wave trapping and Bragg resonance. The coupling effects of monochromatic wave propagation and wave trapping are analyzed. In addition, the study systematically examines and elucidates the influence of various parameters of incident waves and bathymetry on Bragg resonance. Furthermore, the most effective conditions over different bathymetries for the Bragg resonance are determined.

1.3 Thesis layout

The thesis contains a total of seven chapters. The scope of this thesis is presented in Figure 1.2. The background and objectives of the thesis are introduced in Chapter 1, followed by the literature review of nonlinear wave propagation over abrupt depth transitions and wave resonance over periodic bottoms (Chapter 2).

Chapter 3 illustrates the research methods of this thesis, including the numerical model and experiments. The monochromatic waves with second-order Stokes theory and focused waves based on NewWave theory in a constant water depth are introduced. Governing equations and numerical solution methods of the fully nonlinear numerical model are presented. The section on the experiments mainly provides information on facilities and equipment in the wave tank. The pre-processing and post-processing techniques for experimental data are presented in detail.

Chapter 4 investigates the nonlinear wave propagation over ADTs experimentally and numerically. The set-up parameters of testing cases are presented. The decomposition of measured and numerical signals is carried out. The ADTs enhance the higher harmonic amplitudes and they increase with the higher wave steepness. The increased skewness and kurtosis demonstrate the high asymmetry of the surface elevation at the transitions, providing a comprehensive view of the wave dynamics.

Chapter 5 studies the nonlinear evolution of focused wave groups over ADTs experimentally and numerically. The specific decomposition of each harmonic is provided, along with the separation of the second bound and free waves. The ADT causes an increment of crests of focused wave groups and a downstream shift of the corresponding position. The analysis of bound and free waves offers insights into the physical mechanism of the occurrence of freak waves over transitions.

Chapter 6 discusses wave trapping and Bragg resonance over varying bottoms, including the interaction of transitions and monochromatic wave trapping, and the Bragg resonance of focused wave groups over periodic bottoms. The influence of the parameters of incident waves and the submerged bottoms is investigated individually. The variations of resonance peak and frequency shift suggest the effects of superharmonics. The existence of higher-order Bragg resonance is verified by analyzing the resonant reflections of the focused wave group over multiple depth transitions.

Chapter 7 summarizes the general conclusions of Chapter 4 to Chapter 6. Future work is recommended as well.

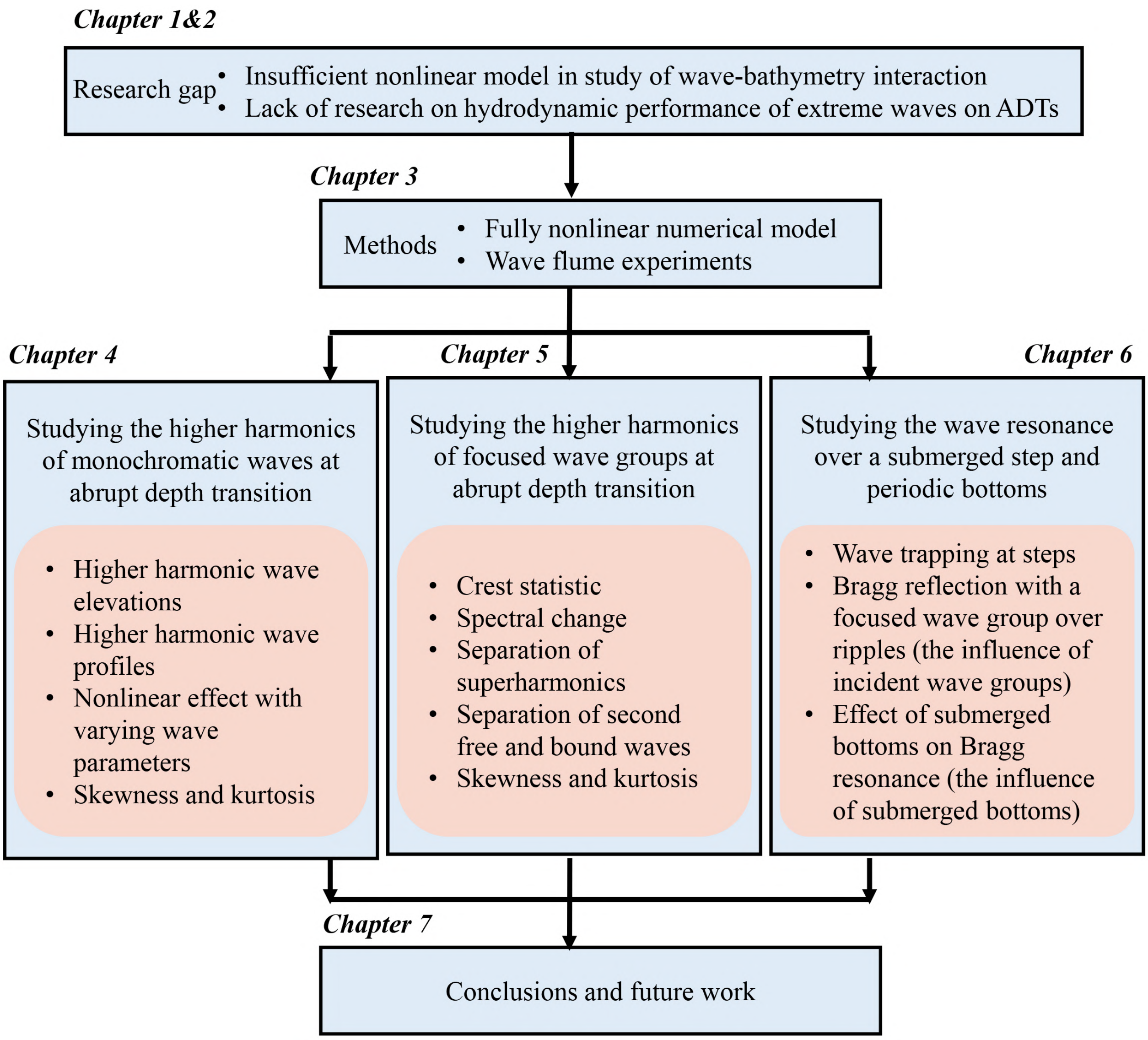

Figure 1.2: The framework for the organization of the main body of the thesis.

Chapter 2

Literature Review

2.1 Introduction

Extreme waves can suddenly occur in rough sea conditions, seriously threatening coastal structures and living conditions. The abrupt depth transition has been identified as a potential cause that increases the likelihood of extreme wave occurrence. However, a detailed explanation of the mechanism from the perspective of hydrodynamic performance remains limited. Therefore, evaluating the nonlinear evolution of harmonics and wave scattering over varying bathymetries has become a major concern for researchers. This chapter provides a review and summary of existing research in hydrodynamic characteristics over varying bottoms, including the different types of incident waves, research methods, wave resonance and a few useful proxies. It also highlights the gaps in current research, pointing the way for the thesis work investigations.

2.2 Wave propagation over abrupt depth transitions

The genesis of extreme waves, also called ‘rogue’ or ‘freak’ waves, has attracted increasing attention over the past decades (Madsen et al., 2008; Ou et al., 2002; Zhang et al., 2022). As ocean waves propagate towards the near-shore region, they can be influenced by the undulating bottom topography, leading to wave refraction, reflection, and shoaling (Lynett et al., 2010; Pelinovsky et al., 2015). Several physical mechanisms have been proposed to explain the dynamic process of extreme waves. One potential mechanism of the formation of extreme waves is the nonlinear interaction between the surface wave and the strong depth transitions (Kharif and Pelinovsky, 2003).

The physical mechanism of extreme waves occurrence over the abrupt depth transitions (ADTs) in the occurrence of extreme waves has been confirmed in the past decade (Gramstad et al., 2013; Li et al., 2021b; Trulsen et al., 2020). In studying the influence of wave evolution over varying bathymetries, the trapezoidal bar (shoal) is commonly employed to study the nonlinear wave propagation (Trulsen et al., 2012; Viotti and Dias, 2014; Zhang et al., 2023a), also includes the infinite, finite steps, slopes etc (Tang et al., 2023; Yang et al., 2023; Zheng et al., 2020). The trapezoidal bar allows for a gradual wave evolution, facilitating the investigation and observation of nonlinear wave propagation. In contrast, studies involving a finite step are minor due to the complexity of wave scattering at the depth changes, which involves wave reflection and transmission in both deeper and shallower water regions (Brossard et al., 2009; Massel, 1983; Mondal and Takagi, 2019). The statistical distribution of wave fields over depth transitions are analyzed from the perspective of kurtosis and probability density functions (Bolles et al., 2019; Li et al., 2021b; Zhang and Benoit, 2021). Skewness and kurtosis correspond to the third and fourth moment of surface elevations, respectively. For a surface elevation that is a Gaussian random process, the skewness is shown to be 0, and the kurtosis is 3. The degree of deviation from the Gaussian random process can indicate the occurrence probability of extreme waves.

Research about wave propagation over the varying bottoms is various and serves different purposes. Most articles consider different submerged breakwaters and aim to explore more effective wave absorption (Chang and Liou, 2007; Ji et al., 2017; Stamos et al., 2003). In addition, some research studies the hydrodynamic characteristics with high wave steepness to propose a higher solution to nonlinear wave equations (Baldock et al., 1996; Galan et al., 2012). Despite the potential mechanism of extreme waves being proposed in recent decades, only a limited number of studies have investigated the superharmonic evolution on the abrupt depth transitions (Moore et al., 2020; Zhang and Benoit, 2021).

Different types of incidence waves have been employed in the studies of extreme wave occurrence in coastal regions. To excite the strong nonlinearity of extreme waves, the common types of incident waves include random waves, solitary waves, and wave packets. The latter two wave types are reviewed in this section. In addition, monochromatic waves are usually used to investigate the basic dynamic process of water waves over varying bathymetries. The analysis relating to the statistical performance is reviewed as well.

2.2.1 Monochromatic waves

In the 1980s, monochromatic waves were typically used to study wave propagation over a submerged obstacle (Kobayashi and Wurjanto, 1989; Massel, 1983). Several numerical models have been developed to account for the nonlinearity of waves propagating over varying bathymetries. A numerical model using the Boundary Integral Element Method (BIEM) was introduced (Gu and Wang, 1993). The model calculates the energy dissipation inside breakwaters with irregular cross-sections for monochromatic waves, focusing primarily on dissipation due to percolation and including breaking effects. Subsequently, Cruz et al. (1993) derived a set of nonlinear vertically integrated equations to predict wave transformation on a one-dimensional arbitrary topography, considering dissipation due to the porous medium and wave breaking. However, these earlier models provide limited insight into the kinematics and dynamics of extreme wave occurrence. Boudjelal et al. (2022) altered the tilting angle of the submerged step and discovered that the maximum velocity occurs at the end of the obstacle. High waves, such as those with a wave steepness of 0.13 and other short-crested waves, have also been used to study the possibility of extreme waves (Latifah et al., 2021).

As waves propagate from deeper to shallower water regions, wave refraction can transform the wavelength to become shorter, while the amplitude and the steepness become larger (Massel, 1983). Two different water depth areas integrated could realize a strong depth change. In such conditions, fully nonlinear wave models with linear and nonlinear dispersion are effective tools to solve the nonlinear dynamic process of water waves. For example, a set of fully nonlinear Boussinesq-type equations (BTEs) was proposed to examine the wave propagation over two areas with the relative water depth $kh < 2$ and $kh < 10$ (k is the wavenumber, h is the water depth), so that both of the weakly and strongly nonlinear performance can be considered (Galan et al., 2012).

2.2.2 Solitary waves

Tsunamis, typically triggered by earthquakes, originate in the deep ocean as extremely long waves with small steepness (Madsen et al., 2008). These waves are transient and non-periodic in nature, and as they propagate from the ocean to the nearshore area, their amplitudes, wavelengths, and wave periods undergo gradual modifications. Since the early 1970s, it has been commonly assumed that solitary or cnoidal waves can be utilized to model key features of tsunamis as they approach the beach and shoreline. Theories stemming from the Korteweg–de Vries (KdV) equation are often used to define the appropriate input waves for physical or mathematical tsunami models. Examples from the literature are numerous, e.g. Synolakis (1987), Lakshmanan (2007).

The slope bottom is commonly employed to change the water depth. It was found before its disintegration, and a wave crest is steeper at the front and flatter at the back (Mandelbrot and Wallis, 1969). This unique phenomenon has spurred further research into the effects of abrupt depth changes on the genesis of extreme waves. Then, Viotti et al. (2014) further investigated whether the extreme waves could be induced by the strong depth transitions (Figure 2.1). They numerically

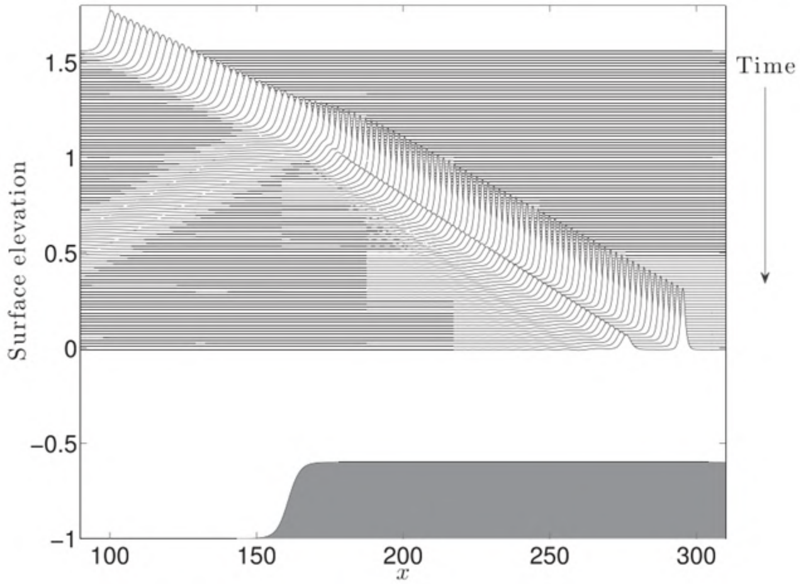

Figure 2.1: Evolution of the solitary wave propagating over a strong depth variation (Viotti et al., 2014).

reproduced the propagation of a solitary wave with a Gaussian distribution travelling on a shoal. By analysing the probability density functions (pdfs), skewness, and kurtosis, they discovered a deviation from the Gaussian process, demonstrating the influence of varying water depth on the incident solitary wave. Beyond two-dimensional research, three-dimensional (3D) studies have also been proposed. For instance, Geng et al. (2021) utilized a parallelized 3D boundary element method to simulate the interaction between a solitary wave and a 3D submerged horizontal plate under the assumption of potential flow, which primarily focused on the vertical and parallel wave force on the plate.

2.2.3 Wave packets

The evolution of a long envelope of short surface waves is a complex process, characterized by the interplay between wave nonlinearity and dispersion. A wavepacket can emit bound solitons in deep water or finite but constant depth conditions. These solitons do not separate but interact with each other, resulting in a phenomenon known as recurrence (Likhachev et al., 2015). These interesting features can be inferred from the exact solution proposed by Shabat and Zakharov (1972). Further elucidation has been provided by Satsuma and Yajima (1974) and Yuen and Lake (1980), who conducted comprehensive surveys of this phenomenon in both theoretical and experimental aspects. The effects of variable depth on wave dynamics have been explored by Djordjevié and Redekopp (1978). They deduced a cubic Schrodinger equation with variable coefficients for bottom slopes that are significantly less steep than the slope of the envelope. Their work predicts that a soliton envelope can undergo fission only if it propagates into deeper water. By making assumptions for the evolution along the slope, they also estimate the number of solitons emitted after a single soliton descends from a shallower shelf.

In 1983, Massel conducted a study on the second harmonics for various finite or infinite submerged steps, analyzing the corresponding reflection coefficients of measurements in a wave tank. The analytical solutions for the second harmonics on a rectangular submerged bar were subsequently extended (Lee et al., 2014; Li et al., 2021c). In 2020, Moore et al. conducted experiments on the propagation of randomized surface waves. The theoretical model derived by Majda et al. aligned well with the experimental results using the truncated Korteweg-de Vries (TKdV) system. Li et al. (2021) considered narrow-bandwidth wavepackets propagating in a region with an abrupt change of water depth within the framework of two-dimensional potential-flow theory (Figure 2.2). The wave propagation over an infinite step in finite water depth demonstrates the strong effects of steps on the bound subharmonics and superharmonics at the second order. However, existing studies primarily focus on the second harmonics or the statistical characteristics at the abrupt depth transitions when studying nonlinear effects (Draycott et al., 2022; Zhang et al., 2022). The characteristics of harmonics higher than the second over a submerged step have not been extensively studied.

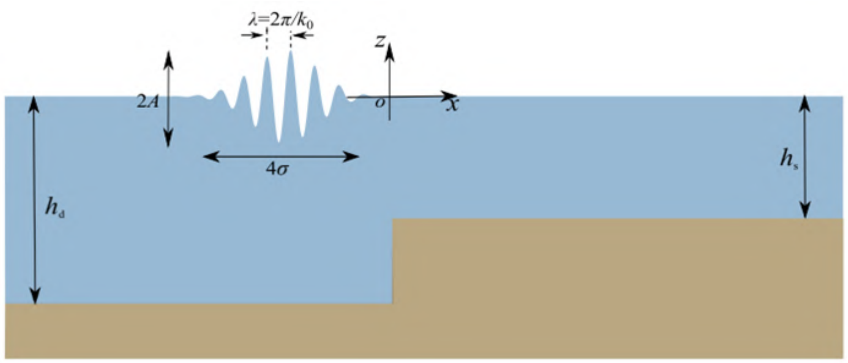

Figure 2.2: Diagram of the bathymetry and coordinate system adopted with a narrow-banded wavepacket (Li et al., 2021a).

2.2.4 Statistical performance assessment

Previous research has confirmed that a significant modification of the wave spectrum can be found at abrupt water depth change (Rey et al., 1992; Viotti and Dias, 2014). To characterize the occurrence of extreme waves, the parameter of kurtosis, which measures the degree of tails of a normal distribution, is used. For a Gaussian process, the value of kurtosis is 3. As a wave propagates from a deeper to a shallower area, the distribution of the wave fails to maintain its original equilibrium. This results in an increase in kurtosis at the depth transitions, exceeding the value of 3. A unidirectional wave field that is normally distributed becomes highly skewed and non-Gaussian when it encounters an abrupt depth change (Bolles et al., 2019; Majda et al., 2019). For different bathymetries, the collection of statistical information, particularly kurtosis and crest exceedance, can help quantify the occurrence of exceptionally extreme waves (Zhang et al., 2019). This higher kurtosis indicates a greater likelihood of rogue wave occurrence. Therefore, the distribution of wave statistics resulting from rapid water depth changes is of fundamental interest in explaining the phenomenon of rogue waves in coastal regions (as illustrated in Figure 2.3).

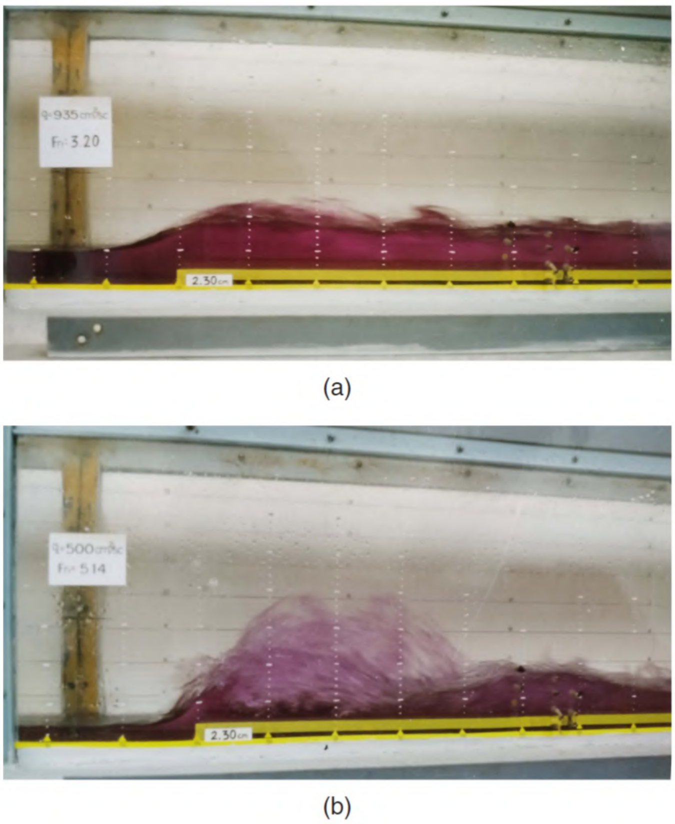

Figure 2.3: Typical wave formation over an abrupt bottom rise: (a) non-aerated wave and (b) aerated wave (Eroğlu and Taştan, 2020).

According to several studies on freak waves offshore, Janssen (2003) theoretically investigated the occurrence of freak waves caused by the interaction of four waves in a short time. It was also found that the nonlinear transfer is associated with an increase in the fourth-order cumulants, equivalent to kurtosis. Similarly, Latifah et al. (2021) investigated the possibility of highly abnormal waves by analyzing the essential change in the statistics measures, particularly skewness, kurtosis, and crest exceedance. They observed high kurtosis in the area of wave transformation over the shoal, indicating a higher probability of extreme wave occurrence. The work of Massel (1983) was extended to elucidate the mechanism behind the observed increases in excess kurtosis at the top of slopes (Li et al., 2021b). This research provides valuable insights into the complex dynamics of wave propagation over varying bathymetries. Furthermore, Trulsen et al. (2012) discovered a local maximum of kurtosis and skewness near the shallower side of the slope. They also found a local maximum probability of a large wave envelope at the same location.

Li et al. (2021) developed a second-order theory and conducted experiments to study the propagation of narrow-banded surface gravity wave packets over a rectangular submerged bar. They observed the release of a superharmonic wave where the in-phase reflected wave packet propagated in the opposite direction, and the out-of-phase transmitted packet travelled in the same direction as the main packet, at a slower speed. Bolles et al. (2019) conducted experimental studies on the surface wave over an infinite step and found a higher probability of rogue waves occurring a short distance downstream. They further studied the effect of water depth and incident wave steepness on the likelihood of rogue waves, both experimentally and using the truncated Korteweg-de Vries (TKdV) system. This work provides a clear dependence on kurtosis to predict the degree of rogue waves.

2.3 Nonlinear focused waver groups

Extreme waves are typically characterized by a maximum amplitude that exceeds twice the significant amplitudes in turbulent seas. Extreme waves have caused severe damage to offshore structures and vessels (Morim et al., 2023). Therefore, accurate estimation of the maximum wave height and prediction of freak wave occurrence is crucial for marine safety and ocean development.

Despite the existence of numerous hypotheses regarding the occurrence of extreme waves, a consensus explanation remains under investigation (Kharif and Pelinovsky, 2006; Li and Chabchoub, 2023). In recent studies, focused wave groups have been widely used to represent extreme waves, particularly in laboratory settings (Chow et al., 2022; Zhang et al., 2021a). The generation of focused wave groups can be regarded as a series of monochromatic waves propagating together and achieving a superposition of wave crests at a prescribed position and time (Sriram et al., 2015). These wave components with different frequencies, phase velocities and initial phases can form new wave groups with high crests. Thus, focused wave groups can be employed to describe the evolution of rogue waves, characterized by a sudden occurrence and emission of a peak wave offshore. Over the past decades, the study of the nonlinear evolution of focused wave groups has emerged as a primary subject in coastal engineering, attracting an increasing number of researchers (Gao et al., 2023; Ransley et al., 2021; Sriram et al., 2015). Apart from the study of nonlinear focused wave propagation in the constant water depth, most research has concentrated on the effects of extreme waves on offshore structures, such as circular cylinders, mooring structures, and floating structures (Chow et al., 2022; Liu et al., 2020; Ransley et al., 2020; Ransley et al., 2021). The study on focused wave groups over breakwaters also started recently (Rodrigo et al., 2021; Zhang et al., 2023b).

NewWave theory is widely accepted as a linear description of the focused wave group (Chow et al., 2022; Sriram et al., 2015). The superharmonic generation during wave propagation over the constant or slowly varying depths has been studied. For instance, in 2017, the second-order analytical solution of NewWave theory was proposed (Sun and Zhang, 2017). To account for strong wave dispersion, Judge et al. (2019) proposed a numerical model with two systems to study the propagation of multi-directional focused wave groups over a plane beach. They employed the Boussinesq equation to model pre-breaking evolution and the nonlinear shallow water equations to simulate the post-breaking. Ko and Lynett (2019) conducted experimental and numerical tests on the run-up of solitary waves and focused wave groups over a bi-linear slope beach. In addition, Abroug et al. (2020) investigated the interaction of focused wave groups with a slope, intending to capture the spatial energy transfer. A limited number of studies have explored extreme wave generation and its interaction with abrupt depth transitions. In this section, the research methods of focused wave groups are reviewed, especially for the application of fully nonlinear numerical models in the nonlinear wave propagation over varying bathymetries.

2.3.1 Experimental studies

Laboratory research on wave propagation over abrupt depth change is not common (Bolles et al., 2019; Trulsen et al., 2012). In 2012, Trulsen et al. conducted experimental studies on the nonlinear rogue wave induced by a non-uniform bathymetry. Prior to this, most laboratory research was related to the pure nonlinear non-Gaussian statistics of extreme waves. Figure 2.4 shows the experimental set-up and the flow path of the wave process on the abrupt depth change.

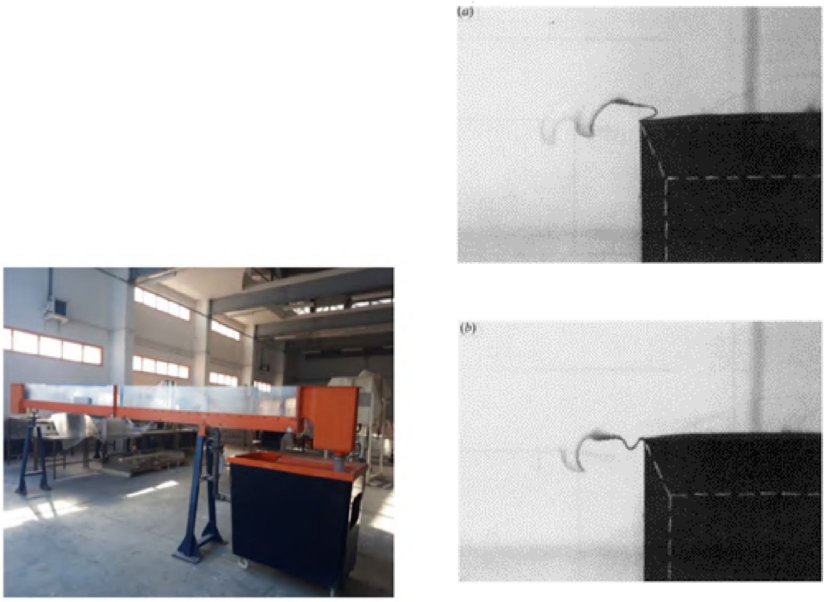

(a) (b)

Figure 2.4: General view of the channel (Boudjelal et al., 2022) and the flow pathlines over the sharp corner bar in (a) the flow is upstream and in (b) the flow is downstream (Rey et al., 1992).

In 1996, Baldock et al. first presented a series of experiments with a group of waves focused and formed a large transient wave amplitude. They found a much higher nonlinearity of wave-wave interaction compared with the linear and second-order solutions. Kway et al. (1998) studied the breaking of focused wave groups in deep water by setting the steady steepness of each wave component in the wave group. Taylor et al. (1997) also experimentally studied the propagation of a focused wave group over a large diameter column. In 2006, Borthwick et al. further researched the breaking characteristics of focused wave groups on a beach, capturing the significance of second harmonic components. Abroug et al. also discussed the influence of the frequency range and steepness on the nonlinear interaction of focused wave groups on the beach (2020). On the other hand, Ko and Lynett (2019) found that low-frequency waves play a more important role in the transient-focused wave groups. Later, researchers paid more attention to the generation of focused wave groups in the experimental measurements. For instance, Banks and Abdussamie (2017) studies the nonlinear effects of the piston-type wavemaker on the quality of waves.

2.3.2 Numerical studies

2.3.2.1 Numerical models of focused wave groups

Given the constraints of laboratory set-up and the escalating need to study extreme waves, various numerical simulations have been developed to capture the intricate and highly nonlinear dynamics of focused wave groups. In 2008, Choi et al. utilize the Navier-Stokes (NS) equations, taking into account viscous effects, which primarily concentrate on wave-structure interactions. Similarly, Westphalen et al. (2012) and Chen et al. (2014) solved NS equations using the finite volume method (FVM) with Computational Fluid Dynamics (CFD) and OpenFOAM, respectively.

These solutions enabled the realization of the fully nonlinear process of focused wave groups. In 2019, Luo et al. employed the Boussinesq equations with FVM. The results were subsequently validated with measured data. Li et al. (2014) later introduced a 3D wave tank that describes the interaction between the focused wave group and a vertical circular cylinder. Orszaghova et al. (2014) emphasized the importance of second-order wave generation, particularly in exploring run-up and overtopping.

In this field, commercial software has been widely used to model and analyze water waves. Popular options include CFD and OpenFOAM, but there are also open-access numerical methods available, such as REEF3D (Bihs et al., 2017). These methods offer a broad and easy-to-use approach to examine the evolution of water waves over varying bathymetries. However, there are limitations to using commercial software for studying water waves. For instance, these methods often require significant computational resources and time, especially when high precision is needed for local wave movements. Additionally, commercial software typically has a limited ability to handle wave nonlinearity in free surfaces (Schmitt et al., 2012; Wang et al., 2020b). In conclusion, while commercial software has been widely used in the study of water waves, it also has its challenges and limitations. To advance the field of water waves, it is essential to continue exploring new approaches and improving existing methods.

2.3.2.2 Fully nonlinear potential flow models in studying ADTs

When viscous effects are not considered, the efficiency of numerical simulations can be improved by solving only the potential theory (Madsen et al., 2006; Viotti and Dias, 2014; Zheng et al., 2020). This approach is particularly useful in the study of fully nonlinear and dispersive models, which are important for understanding nonlinear wave propagation due to depth variations. For instance, Ducrozet and Gouin (2017) investigated directional sea states propagating over a sloping bottom with the higher-order spectral method (HOSM) (Gouin et al., 2016). Their study demonstrated the significant influence of directional spreading on sea-state dynamics. More recently, Zheng et al. (2021) employed a fast multipole boundary element (FMBE) method to simulate the experiments conducted by Trulsen et al. (2012). They tested a wider range of parameter choices, examining the effects of wave steepness, relative water depth and bottom gradient on the length of latency. The length of latency is defined as the distance between the end of the shoal and the position where skewness and kurtosis reach their maximum values. In another work, Zhang et al. (2019) used fully nonlinear and dispersive potential flow code, known as whispers 3D, and compared it with a Boussinesq-type model introduced by Bingham et al. (2009). The high degree of agreement with the measurements taken in a large wave flume attests to the accuracy of Whispers 3D. However, it is important to note that this model requires substantial computational memory.

In recent years, fully nonlinear potential flow models have been developed to study superharmonics in wave evolution over varying bathymetries. For instance, Galan et al. (2012) utilized a fully nonlinear Boussinesq-type equation to investigate waves transitioning from deep to shallow waters on a submerged trapezoidal step. Similarly, Zhang and Benoit (2021) established a fully nonlinear model using a spectral approach to study irregular waves over abrupt depth transitions, with their statistical results aligned well with the experimental results presented by Trulsen et al. (2020). Belibassakis and Athanassoulis (2011) presents a nonlinear coupled-mode system for modelling the propagation of nonlinear water waves in a region of finite water depth and varying topography. They verified its effectiveness under different water depth conditions by numerical methods. Cheng et al. (2017) developed a 2D fully nonlinear numerical model to study the interaction between a focused wave group, a floating elastic plate, and a submerged horizontal layer. In 2019, Chen et al. developed a 3D parallel-particle-in-cell (PIC) model to explore the effects of both a floating and a fixed offshore cylinder. Other studies have also referred to floating structures, such as those by Cheng et al. (2020) and Hu et al. (2020). Notably, the fully nonlinear model solving the potential theory has been validated to achieve computation with less running time and computational memory (Hu et al., 2020).

To improve the accuracy of numerical simulations, another 3D numerical model was proposed that couples the weakly compressible smoothed particle hydrodynamics (SPH) and the fully nonlinear potential theory on the extreme wave-structure interaction (Zhang et al., 2020). However, there remains significant uncertainty over the required level of model fidelity when applied to a wide range of wave-structure interaction problems. In 1970, Smith introduced the conformal mapping method to compute the evolution of waves, which maintains the local hydrodynamic characteristics in the mapping process. To study strong nonlinear effects resulting from water depth transitions, Viotti et al. (2014) improved the solutions to the two-dimensional (2D) Euler equations by a conformal mapping method. Without the loss of generality, it shows a good agreement with the measurements (Choi and Camassa, 1999). The study revealed that the non-equilibrium responses in a local region increase with stronger depth variations, which leads to an intensified occurrence of extreme waves. This method requires less computational effort than direct numerical methods to solve nonlinear models, such as the KdV and Boussinesq equations (Dyachenko et al., 1996). However, it has been limited to the complex establishment of the model. Therefore, It is rarely employed in the study of nonlinear wave propagation, especially for interactions with abrupt depth transitions. In this thesis, we decide to use the conformal mapping method to reproduce the evolution of the focused wave group. This numerical method shows its ability to accurately simulate nonlinear wave propagation over varying bathymetry using the conformal mapping method, which efficiently solves potential theory and allows for the implementation of arbitrary bathymetry.

2.4 Wave resonance with various bathymetries

2.4.1 Wave trapping

Wave propagation on beaches with an alongshore inhomogeneous bathymetry is complicated. For instance, curved sand bars (Lippmann and Holman, 1990) and rip channels in the surf zone (MacMahan et al., 2006), with alongshore length scales of order 100 m, cause alongshore variations in wave heights and directions. Large alongshore gradients in surf zone waves and circulation can also be triggered by irregular bathymetries, such as submarine canyons, in water depths as great as 200 m (Long and Özkan-Haller, 2005). Consequently, understanding and accurately predicting such phenomena pose a significant challenge and have become a contemporary topic of interest in applied mathematics. Wave trapping is a unique phenomenon where certain sinusoidal waves might be trapped on the upper side of a submerged ridge due to wave reflection. In other words, waves may exist at a depth discontinuity but are unable to propagate from shallower to deeper water regions. This phenomenon further increases the complexity of wave dynamics and requires careful study and modelling.

A preliminary study of trapped waves along ridge structures can be traced back to the study by Ursell (1951), who demonstrated that a trapped wave mode could exist over a submerged circular cylinder with a sufficiently small radius. Kowalik et al. (2008) demonstrated that the energy field of the 2006 Kuril tsunami was redistributed by the trapping effect of the Koko Guyot and Hess Rise in the North Pacific Ocean. This resulted in a second large wave packet arriving in Crescent City 2–3 hours later. During the 1996 Irian Jaya earthquake, the resulting tsunami propagated across the Pacific Ocean and caused damage to coastal regions in Japan. This occurred despite Japan being far from the tsunami source and seemingly not on the route of the major tsunami energy. Koshimura et al. (2001) subsequently verified the mechanism of tsunami propagation trapped on an oceanic ridge using a simple ridge model. Rainey and Longuet-Higgins (2006) derived analytical solutions for the trapped waves over a ridge with a step-like profile, which allowed for further analysis of changes in phase speed and group velocity against the wavenumber.

Although both observations and modelling results have demonstrated the existence of wave trapping, the dynamic properties of the trapped waves remain poorly understood, indicating that relevant research is still in its early stages (Neetu et al., 2011). The topic of trapped wave propagation over abrupt depth changes was studied primarily with an emphasis on the influence of the height of the bathymetry (Koshimura et al., 2001). However, the specific excitation conditions of the water depths resulting in wave trapping have not been considered. Figure 2.5 shows the wave profiles of the first four trapped modes on a submerged ridge. Thus, The co-effects of abrupt depth transitions and the resonance induced by the wave-bathymetry interplay are significant to investigate.

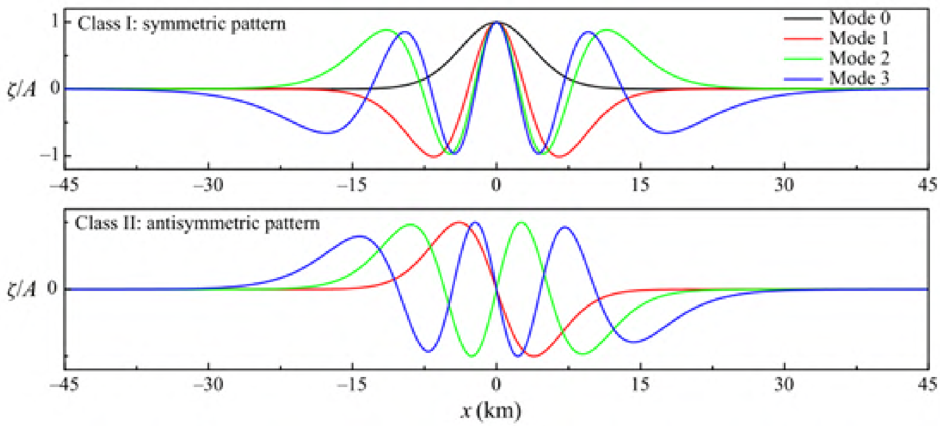

Figure 2.5: Normalized wave profiles for the first four modes over the ridge (Wang et al., 2021).

2.4.2 Bragg resonance

Bragg resonance is a phenomenon of wave reflection that occurs when the wavelength of submerged bars is half of that of incident waves (Belzons et al. 1991; Hsu et al. 2003). The interaction between the wave and the bottom causes a high reflection of propagating water waves. In the past decades, Bragg resonance has been widely studied, and five more types of Bragg resonance have been found (Ning et al. 2022b; Peng et al. 2019; Zhang et al. 2021b). The peak reflection coefficients indicate the ability of coastal breakwaters to shoreline protection. Therefore, the breakwaters with different shapes of periodic bottoms have been designed and studied, such as sinusoidal bars, rectified conoidal bars, and so on (Liu 2023; Xu et al. 2023; Zhang et al. 2021a). Besides, the effectiveness of these breakwaters was widely investigated from the perspective of reflection coefficients (Guo et al. 2021; Liu et al. 2016; Tsai et al. 2011).

Numerous analytical and numerical studies have been conducted on the research of Bragg resonance over periodic bars (Liu et al., 2019a, 2015; Xie and Liu, 2023; Zeng et al., 2017). Most of these experimental studies have been limited to regular waves. For instance, Kirby and Anton (1990) conducted experiments with monochromatic waves propagating over rectified sinusoidal bars, using the same bottoms as in Davies and Heathershaw's study. The data measured in these two studies provide a precise reference for subsequent investigations by numerical simulations. The Bragg resonance of regular waves over trapezoidal bars was also studied experimentally by Jeon and Cho (2006). In addition to regular waves, irregular waves have also been considered (Abbasnia et al., 2017; Ardhuin and Herbers, 2002; Hsu et al., 2007), which have primarily focused on random waves. For example, early studies used the TMA shallow-water spectrum in studying the Bragg resonance with random waves. Suh et al. (1997) considered both narrow and broad-banded frequency spectra and presented the incident and transmitted wave spectra. Later, Hsu et al. (2007) studied the Bragg resonance of random waves using the commonly used JONSWAP spectrum with rectified bars, sinusoidal bars, and trapezoidal bars.

Several commonly theoretical and numerical methods exist in research on the Bragg resonance of irregular waves over periodic bars. In the 2000th, the mild-slope equations were mainly employed in studying Bragg reflection coefficients (Lee et al., 2003; Suh et al., 1997). Hsu et al. (2007) compared the reflection coefficients with the measured data, then extended the mild-slope equation and the Boussinesq-type model. The Boussinesq-type model was found better to capture the exact Bragg resonance. In the subsequent years, the Boussinesq-type model became more commonly used in the study of Bragg resonance (Bingham et al., 2009; Liu et al., 2019b; Madsen et al., 2006). However, the above-mentioned work only considers regular monochromatic waves or random sea states. Given the increasing occurrence of extreme waves in recent years, however, there are rare studies on the hydrodynamic performance of breakwaters in extreme wave conditions. Thus, there is still a significant research gap in the field.

2.5 Summary

This chapter comprehensively reviews the past and present research about abrupt depth transitions, focused wave groups, fully nonlinear models, wave trapping and Bragg resonance. Existing research gaps and challenges are identified and discussed, particularly concerning the harmonics over abrupt depth changes, the nonlinear interaction between waves and bathymetries, and wave resonance. The key points are summarized as follows:

1. The application of a fully nonlinear numerical model utilizing the conformal mapping method for the study of wave propagation over bathymetries with abrupt depth transitions remains an unexplored area of research. The absence of experimental data to validate the accuracy of this approach exists, particularly in the context of focused wave group propagation on depth transitions.

2. Though the effects of abrupt depth transitions have been studied in the mechanism of occurrence of extreme waves, the hydrodynamic performance of superharmonic has been neglected. Moreover, there is a pressing need to delve into the detailed evolution of fundamental and higher harmonics in the spatio-temporal domain.

3. Limited research has been conducted on the nonlinear propagation of a focused wave group on ADT, particularly in the context of superharmonic superposition. There is also a lack of literature on the dynamics of bound and free waves and their impact on wave propagation. The difference between the focused wave

groups and monochromatic waves in wave propagation over ADTs still needs investigation.

4 Furthermore, the consideration of higher-order effects in wave resonance has received limited attention in existing literature. Specifically, the calculation of reflection coefficients for focused wave groups has not been thoroughly developed. Additionally, the higher-order Bragg reflection of focused wave groups over periodic bars has been rarely explored.

The following chapters will discuss these issues and present the detailed work and key findings to fill these gaps.

Chapter 3

Methodology

3.1 Introduction

This chapter presents a detailed description of the numerical model, laboratory techniques and data processing method in researching the nonlinear evolution of extreme waves and their interaction with varying bathymetries. The theoretical models of incident waves are explicated for both monochromatic and focused wave groups. The development of a fully nonlinear numerical model is detailed, outlining the governing equations, the conformal mapping method and the solving method. The model has been validated with measured data before being applied to the study of nonlinear wave propagation. The chapter also introduces the laboratory wave tank and associated facilities. Three distinct decomposition methods of superharmonics are introduced, including the Fast Fourier Transform (FFT), the phase-manipulation approach and the continuous wavelet transform (CWT). The selection of the method depends on the specific research objective. In the study of wave reflection, Goda's two-point and four-point methods are employed to compute the fundamental reflection coefficients and that of superharmonics, respectively. Lastly, the calculation of skewness and kurtosis of surface elevations can be examined.

3.2 Theoretical model

A 2D fully nonlinear potential flow model is established within the framework of the free-surface Euler equations (in Figure 3.1). The fluid is assumed to be inviscid and incompressible, with the flow being irrotational. The flow field can be characterized using a velocity potential $\phi(x, y, t)$. To simulate monochromatic wave propagation over varying bathymetries, the conformal mapping method is utilized (Choi and Camassa, 1999; Viotti et al., 2014). The governing equation and the boundary conditions read

$$\bigtriangledown^2\phi = 0 \quad \text{for} \quad b(x) \leq y \leq \eta(x,t), \tag{3.1}$$

$$\eta_t + \phi_x\eta_x - \phi_y = 0 \quad \text{at} \quad y = \eta(x,t), \tag{3.2}$$

$$\phi_t + \frac{1}{2}\left({\phi_x}^2 + {\phi_y}^2\right) + g\eta = 0 \quad \text{at} \quad y = \eta(x,t), \tag{3.3}$$

$$\phi_y = 0 \quad \text{at} \quad y = b(x), \tag{3.4}$$

where (x, y) is a Cartesian coordinate system, with x being the horizontal coordinate and y the upward vertical one. $\phi(x, y, t)$ denotes the velocity potential of the fluid flow and is governed by the Laplace equation shown in Eq. 3.1. Eqs. 3.2-3.3 represent the kinematic and dynamic boundary conditions at the free surface $y = \eta(x, t)$. The kinematic boundary condition at the bottom is given by Eq. 3.4 where

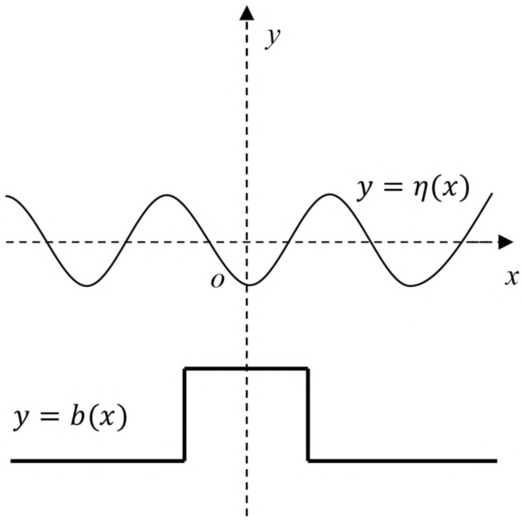

Figure 3.1: Schematic of the water-bathymetry problem.

$b(x)$ is the bottom profile. g is the acceleration due to gravity, and the subscripts denote differentiation. It should be noted that while the conditions imposed by η and $\bigtriangledown\phi$ must be periodic, the periodicity of ϕ is not a necessity.

3.3 Numerical model

3.3.1 The conformal mapping method

The conformal mapping method realizes a transformation from the physical domain bounded by the free surfaces and the bathymetries into a strip in the mathematical domain (in Figure 3.2). With the solution of the Dirichlet boundary-value problem, a complex analytic function $Z = X(\xi, \zeta, t) + iY(\xi, \zeta, t)$ is introduced to map the physical plane (x, y) into the mathematical one (ξ, ζ). The surface elevation in the mathematical plane $Y(\xi, 0, t)$ is assumed to be periodic with $l = 2\pi/k$, where l is the spatial period of solution in the mathematical plane. Thus, the boundary conditions of the free surface and bathymetry profile for the function Y can be expanded in the

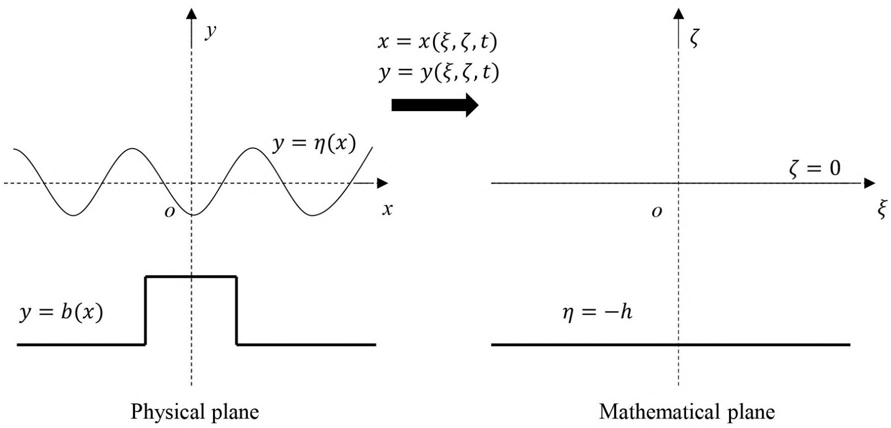

Figure 3.2: The mapping transformation between the physical and the mathematical planes.

Fourier series as

$$Y(\xi,0,t) = y(\xi,t) = \sum_{n=-\infty}^{n=\infty} \tilde{Y}_n e^{ink\xi} \quad \zeta = 0, \tag{3.5}$$

$$Y(\xi,-h,t) = b(\xi,t) = \sum_{n=-\infty}^{n=\infty} \tilde{B}_n e^{ink\xi} \quad \zeta = -h, \tag{3.6}$$

where $\tilde{Y}_n$ and $\tilde{B}_n$ denote the Fourier coefficients of the surface elevation and the bathymetry, respectively. The subscripts n represent the total number of Fourier terms. In Section 4.3.1, the proper number of the Fourier discrete points per wavelength is discussed. By using the Cauchy-Riemann relations $X_\xi = Y_\zeta$ and $X_\zeta = -Y_\xi$, the new general forms of (X, Y) can be easily obtained to satisfy Eqs. 3.5-3.6, which can be written

$$Y(\xi,\zeta,t) = \tilde{Y}_0 + \frac{\zeta}{h}(\tilde{Y}_0 - \tilde{B}_0) + \sum_{n=-\infty}^{n=\infty} \tilde{Y}_n \frac{\sinh nk(\zeta+h)}{\sinh nkh} e^{ink\xi} + \sum_{n=-\infty}^{n=\infty} \tilde{B}_n \frac{\sinh nk\zeta}{\sinh nkh} e^{ink\xi}, \tag{3.7}$$

$$X(\xi,\zeta,t) = x_0(t) + \frac{\xi}{h}(\tilde{Y}_0 - \tilde{B}_0) - \sum_{n=-\infty}^{n=\infty} \tilde{Y}_n \frac{i\cosh nk(\zeta+h)}{\sinh nkh} e^{ink\xi} - \sum_{n=-\infty}^{n=\infty} \tilde{B}_n \frac{i\cosh nk\zeta}{\sinh nkh} e^{ink\xi}, \tag{3.8}$$

where $x_0(t)$ is the origin of the coordinate in the physical plane. Let $h = \tilde{Y}_0 - \tilde{B}_0$ in the above equations Eqs. 3.7-3.8. The first Fourier coefficient will be equal to 1, and therefore, the boundary conditions in the physical plane become periodic with the same period as in the mathematical plane. Note that the mathematical depth h varies with time but $b(x)$ is fixed in the computation. To further simplify the transformation between the two planes, a Hilbert-like operator is used on the harmonic conjugate variables. When ζ tends to 0, Eqs. 3.7-3.8 are written as

$$x_\xi - 1 = \hbar_m[y_\xi, b_\xi], \quad y_\xi = \hbar_n[x_\xi - 1, b_\xi], \tag{3.9a, b}$$

by using the principal-value integral $\oint$ over the real axis. The two operators $\hbar_m$ and $\hbar_n$ are

$$\hbar_m[z, s] = \frac{1}{h} \oint_{-\infty}^{\infty} z(\theta) \coth[\pi(\theta - \xi)/(2h)] d\theta + \frac{1}{h} \oint_{-\infty}^{\infty} (s(\theta) - h) \times \tanh[\pi(\theta - \xi)/(2h)] d\theta, \tag{3.10}$$

$$\hbar_n[z, s] = \frac{1}{h} \oint_{-\infty}^{\infty} z(\theta) \operatorname{csch}[\pi(\theta - \xi)/(2h)] d\theta + \frac{1}{h} \oint_{-\infty}^{\infty} (s(\theta) - h) \times \operatorname{sech}[\pi(\theta - \xi)/(2h)] d\theta, \tag{3.11}$$

where $z(\theta)$ and $s(\theta)$ denote the input functions of θ. The two integral operators $\hbar_m[\cdot, \cdot]$ and $\hbar_n[\cdot, \cdot]$ are an inverse pair where $\hbar_m[\cdot, s] = \hbar_n^{-1}[\cdot, s]$. The same procedures are employed in terms of the velocity potential ϕ and the stream function ψ, the mapping is achieved by the operator $\wp_s[\cdot]$. They are obtained as

$$\phi_\xi - p = -\wp_s[\psi_\xi], \quad \psi_\xi = -\wp_s[\phi_\xi - p], \tag{3.12a, b}$$

$$\wp_s[z] = -\frac{1}{h} \oint_{-\infty}^{\infty} z(\theta) \operatorname{csch}[\pi(\theta - \xi)/(2h)] d\theta, \tag{3.13}$$

where p is the mean free-surface elevation in the physical domain given by $p = \frac{m[y]}{h}$, $m[\cdot]$ computes the mean value. Thus, the original Euler equations (3.1-3.4) are mapped into

$$x_t - x_\xi \left\{ \overline{h}_m \left[\frac{\psi_\xi}{J}, 0 \right] + q(t) \right\} - y_\xi (\frac{\psi_\xi}{J}) = 0, \tag{3.14}$$

$$y_t + x_\xi (\frac{\psi_\xi}{J}) - y_\xi \left\{ \overline{h}_m \left[\frac{\psi_\xi}{J}, 0 \right] + q(t) \right\} = 0, \tag{3.15}$$

$$\phi_t + \frac{1}{J} \left\{ \frac{1}{2} (\phi_\xi^2 - \psi_\xi^2) - J \phi_\xi \overline{h}_m \left[\frac{\psi_\xi}{J}, 0 \right] \right\} + gy = C(t), \tag{3.16}$$

where $J = x_\xi^2 + y_\xi^2$ is the Jacobian on the free surface, and $C(t)$ is an arbitrary function of time that can be absorbed in ϕ_t. The part $q(t)$ is given by $q(t) = m \left\{ x_\xi \overline{h}_m [\frac{\psi_\xi}{J}, 0] + y_\xi (\frac{\psi_\xi}{J}) \right\}$. Therefore, the initial Euler equations in the physical plane are discretized and then mapped into the mathematical plane shown in Eqs. 3.14-3.16.

3.3.2 Solving method with time stepping

A pseudo-spectral method is introduced with an assumption of periodic boundary conditions to solve Eqs. 3.14-3.16. Initial surface elevations are discretized using the Discrete Fourier Transform. Given the variable nature of the bathymetry $h(\xi, t)$, which requires updating during the mapping process, a fixed-point iteration is initially provided. Specifically, the initial estimate $h^{(0)}$, derived from the most recent function value obtained in the preceding time step, is employed to update the bathymetry. The iteration can be written as

$$\Omega^{(n)} = \xi - \overline{h}_m [y(\xi), h^{(n)}(\xi)], \tag{3.17}$$

$$h^{(n+1)} = b(\Omega^{(n)}) \tag{3.18}$$

where $\Omega^{(n)}$ denote the boundary condition for $X(\xi, -h, 0)$. If the residue of $|h(\Omega^{(n)}) - h(x)|$ decreases below a tolerance $1e^{-10}$, the time n can proceed to the next step. Time integration is accomplished using an adaptive algorithm based on the Adams-Bashforth-Moulton method in MATLAB. The multi-step algorithm features a strict error tolerance and a 13th-order formula is used to form the error estimate, making it suitable for problems of dynamic wave evolution. The solving method for the numerical simulation involves a mapping conversion process that quickly computes nonlinear wave propagation, taking only a few seconds to achieve results, even for varying bathymetry with abrupt depth transitions or wavy bottoms.

3.3.3 Wave generation

Surface profiles $y(\xi)$ in Eq. 3.17 depend on the types of incident waves. To simulate the propagation of different types of waves, the surface profiles should be first employed in Eq. 3.17. Then, the iteration of the adaptive algorithm starts to process. The nonlinear results at the target regimes can finally be achieved within the Euler equations. For the same reason, the incident waves can be altered according to different types of incident waves at $n = 0$. It should be noted that this generation method is not like the wave maker in the laboratory tank. Since only the steady-state numerics near the varying bottoms are used for analysis, the linear wave profile generation method at the initial time will not affect the analyzed results. The theoretical models of monochromatic waves and focused wave groups are introduced, which are employed in this thesis work investigation.

3.3.3.1 Generation of monochromatic wave

Two primary theories are utilized to generate monochromatic waves: the linear wave theory and the second-order Stokes theory within the context of the linear wave theory (Airy, 1845). The ratio of wave height H to water depth h is deemed infinitesimal. Similarly, the wave steepness $\varepsilon = kH/2$ (k is the wavenumber) is considered infinitesimal. The fluid flow is hypothesized to be an inviscid, incompressible, and homogeneous fluid. This assumption allows for the linearization of both the dynamic boundary condition and the kinematic boundary conditions. Thus, the surface elevation η is written

$$\eta = \frac{H}{2} \cos\left(kx - \omega t\right) = \frac{H}{2} \cos k(x - ct), \tag{3.19}$$

where ω is the angular frequency. The phase is denoted by $kx - \omega t = \theta$. The phase speed $c = \frac{\omega}{k} = \frac{gT}{2\pi} \tanh kh$ is derived from the dispersion relation $\omega^2 = gk \tanh kh$.

When considering the strong nonlinearity on the free surface, there are many types of nonlinear wave theories, including Stokes waves, solitary waves, cnoidal waves, etc. The second-order Stokes theory is employed in this thesis, where the water wave is in the intermediate water regime. In contrast to linear wave profiles (symmetric crests and troughs), nonlinear surface profiles exhibit sharper crests and flatter troughs. This is a key characteristic of nonlinear waves and is a direct result of the nonlinearity of the free surface. To describe the nonlinear characteristics of free surface boundary conditions, an assumption is made that the velocity potential

ϕ and the wave surface η can be expanded in terms of a small parameter perturbation ϵ,

$$\Phi = \epsilon\Phi_1 + \epsilon^2\Phi_2 + ..., \tag{3.20}$$

$$\eta = \epsilon\eta_1 + \epsilon^2\eta_2 + ..., \tag{3.21}$$

due to the effect of the small parameter ϵ, the latter term $\epsilon^2\Phi_2$ is smaller than the former term $\epsilon\Phi_1$, and each term Φ_n satisfies both the Laplace equation and the associated boundary conditions. This expanded form is then substituted into the free surface boundary conditions given by Eqs. 3.2 and 3.3. Then second-order Stokes surface elections are obtained

$$\eta = \frac{H}{2}\cos(kx-\omega t) + \frac{\pi H^2}{4L}(1+\frac{3}{2\sinh^2 kh})\coth kh \cos 2(kx-\omega t), \tag{3.22}$$

$$L = \frac{gT^2}{2\pi}\tanh kh, \tag{3.23}$$

and the corresponding phase speed c_2 considering the second order is updated with the equation (c_0 is the linear wave speed)

$$c_2 = c_0 * (1 + (9 - 10\sigma^2 + 9\sigma^4)/16/\sigma^4 k^2 a^2), \tag{3.24}$$

$$c_0 = \sqrt{g/k * \sigma}, \quad \sigma = \tanh kh \tag{3.25}$$

3.3.3.2 Generation of focused wave group

The focused wave group is a typical wave type used in the study of extreme waves, especially in experimental studies (Feng, 2019; Wang et al., 2020a). The wave group is characterized by a sudden occurrence of high crests, which effectively mimics the characteristics of freak waves in a physical environment (Ransley et al., 2021).

The linear theory of focused wave groups (NewWave theory) was proposed by Rapp and Melville (1990), based on the assumption of a superposition of a group of monochromatic waves. Thus, the surface elevation and velocity potential of focused wave groups can be determined

$$\eta_0(x,t) = \textstyle\sum_{n=1}^{N} A_n \cos[k_n((x - x_p) - c_n(t - t_p))], \tag{3.26}$$

$$\phi_0(x,t) = \textstyle\sum_{n=1}^{N} A_n c_n \frac{\cosh(k_n h_d)}{\sinh(k_n h_d)} \sin[k_n((x - x_p) - c_n(t - t_p))], \tag{3.27}$$

where the focused position x_p and focused time t_p are parameters that determine where and when the maximum wave amplitudes occur. The two parameters control the key features of focused wave groups. The symbol n is the nth wave component in a focused wave group. In this study, the total number of wave components is $N = 2000$. This means that each focused wave group comprises 2000 individual wave components, each with its own wave number k_n, angular velocity ω_n and phase speed c_n. The frequency range is considered a narrow spectrum bandwidth, a JONSWAP-type spectrum

$$S(f_n) = \beta H_s^2 T_p^{-4} {f_n}^{-5} exp[-\frac{5}{4}(T_p f_n)^{-4}]\gamma^{exp[-(f_n/f_p-1)^2/2\sigma^2]}, \tag{3.28}$$

$$\beta = \frac{0.06238}{(0.23 + 0.0336\gamma) - 0.185(1.9 + \gamma)^{-1}}[1.094 - 0.01915\ln(\gamma)], \tag{3.29}$$

$$A_n(f_n) = A_{in}\frac{S(f_n)(f_s)}{\sum S(f_n)(f_s)}, \quad f_s = \frac{(1.8 - 0.3)f_p}{2000 - 1} \tag{3.30}$$

with the significant wave height H_s. The T_p and f_p are the peak wave period and frequency, respectively. The peak enhancement parameter γ is set to 3.30. The spectral width parameter σ is defined as 0.07 for $\omega_n \leq \omega_p$ and 0.09 for $\omega_n > \omega_p$. The linear amplitude of the focused wave group denoted as $A_{in} = \sum_1^N A_n$, a sum of each wave component A_n, is found to be less than the realistic amplitude due to the nonlinear wave-wave interaction. The focused wave groups in the experimental tank are generated using the linear NewWave theory for the initial estimate, which is then input into the tank to produce nonlinear focused wave groups through wave-wave interaction near the prescribed focused position.

3.3.4 Wave absorption

To minimize the reflection of waves at the end of the numerical model, an absorber P_s is added as a liner damping to the free surface boundary condition Eq. 3.3 with a relaxation function $s(x)$, hence Eq. 3.3 is rewritten as

$$\phi_t + \frac{1}{2}\left({\phi_x}^2 + {\phi_y}^2\right) + g\eta + P_S/\rho = 0, \tag{3.31}$$

$$P_S/\rho = s(x)\phi(x, \eta(x,t), t), \tag{3.32}$$

$$s(x) = e^{-[(x-2L)/2]^2}, \tag{3.33}$$

where L denotes half of the length of the numerical tank and ρ is the fluid density. The selection of the damping function $s(x)$ should account for the spurious effects, including the wave reflection and accumulation of fluid inside the damping layer. This accumulation can markedly influence the water depth throughout the remainder of the wave tank. To mitigate both wave reflection and pile-up effectively, it is advantageous to implement weak damping over an extensive area. However, this approach necessitates the allocation of a substantial portion of the computational domain for the damping layer.

3.4 Experiments

3.4.1 Sketch of experimental tank

Two experimental campaigns were conducted in the Hydrodynamic Laboratory of the Hong Kong Polytechnic University and that of the Southern University of Science and Technology, respectively (in Figure 3.3). Details of the wave tank are presented in the next two sections. The wave tanks have a stainless steel bottom and glass walls on both sides. The left top of the tank is equipped with a piston-type wave generator. At the end of the tank, a permeable stainless steel bump minimizes the reflected waves from the tank as shown in Figure 3.4(a). Detailed descriptions of the set-up for both experiments are presented in the next two chapters.

(a) (b)

Figure 3.3: (a) Hydraulics Laboratory of the Hong Kong Polytechnic University; (b) Hydraulics Laboratory of Southern University of Science and Technology.

(a) (b)

Figure 3.4: (a) Wave absorber at the end of a wave tank and (b) wave gauges at the first depth transition.

3.4.2 Experimental facilities

Along the direction of wave propagation, a submerged step is placed to realize two depth transitions. Wave gauges are arranged unevenly over the submerged step to capture the surface elevations, with narrower intervals of gauges near the edges of the step (in Figure 3.4(b)). The step is set a certain distance away from the wave-maker to form two sudden ADTs. By adjusting the water depth, the ratio of the water depth in the shallower regions to that in the deeper ones can be changed. The generated waves are controlled with the Biésel Transfer Function, which adjusts the difference between the input piston displacements and output wave elevations.

3.4.3 Repeatability and correction

With the consideration of the nonlinear wave-wave interaction during the wave evolution, the incident wave heights were obtained from cases without a step in the wave tank. Figure 3.6 compares the input parameters H_{in} and the actual wave height H_{out}.

This allows for the use of more precise incident waves generated in the laboratory for subsequent investigations. In addition, each case is repeated at least three times to ensure the accuracy of measured results (in Figure 3.5).

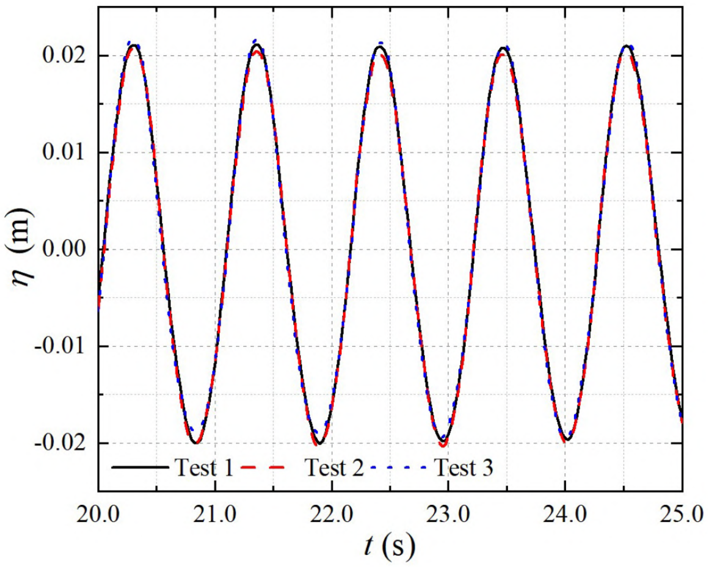

Figure 3.5: Surface elevations with three repeated measured data.

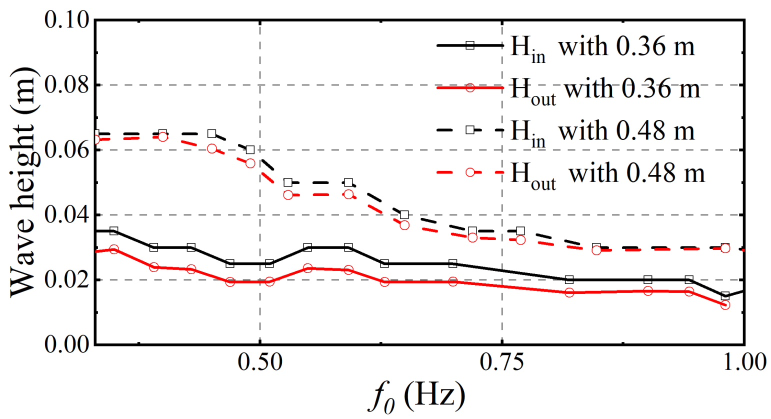

Figure 3.6: Wave heights with input parameters and physical outputs.

3.5 Signal and data processing technique

3.5.1 Time window for spectra analysis

To process the spectral analysis, the surface elevations in the temporal domain are calculated with the Fast Fourier Transform (FFT) to obtain the wave spectrum. The time window of surface elevations needs to be selected appropriately. It should avoid the start-up of incident waves before the arrival of steady regular waves and the reflected waves coming from the back of the wave tank. We take one case with monochromatic waves (frequency of 0.94 Hz and steepness of 0.06) for example to examine the results of FFT with different ranges of the time window (in Figure 3.7). It is found that both the unsteady incident waves and the reflected wave from the backside of the wave tank affect the results of amplitude spectra. Meanwhile, only a small difference is found between the results with the total Fourier discrete points $N = 940$ and those with $N = 1024$. Thus, avoiding the unsteady waves at the beginning and reflected waves from the tank is enough to obtain the spectra.

3.5.2 Separation of the incident and reflected waves

The reflection coefficient obtained from the linear long-wave could provide a good benchmark for us before the numerical and experimental studies. However, isolating these two types of propagating waves is necessary for the numerical and experimental surface elevation results which consist of reflective and transmitted waves. After the isolation, the corresponding reflection coefficients can be figured out through the

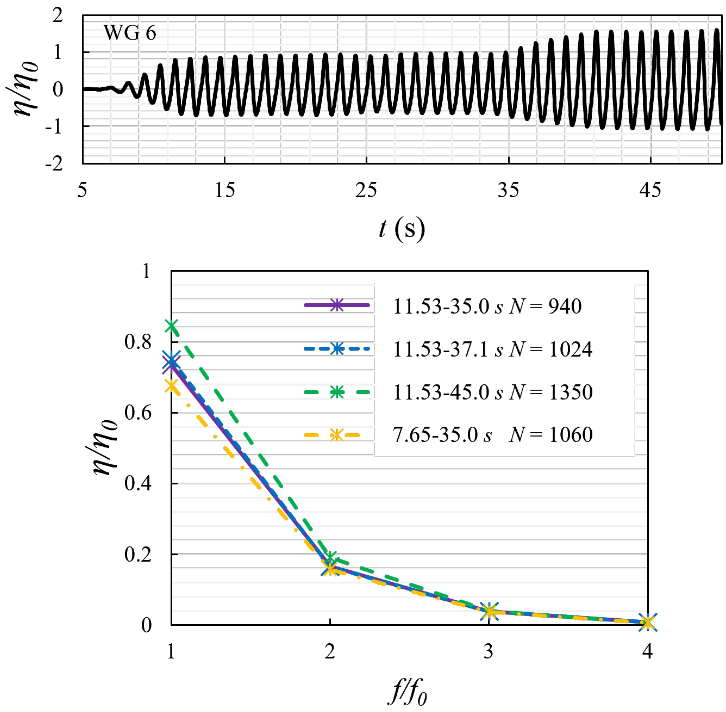

Figure 3.7: Selections of surface elevations and harmonic amplitudes.

definition. In the following part, Goda's two-point method (Goda and Suzuki, 1976) for experimental results and Wang et al.'s isolation method for numerical results are introduced (2003), respectively.

The two-point method is typical for solving the reflection coefficients where complex surface elevations are obtained. Two wave gauges should be placed before the submerged obstacle to collect the surface elevations, especially considering those propagating past the obstacle. Accurate wave profiles usually contain irregular waves so that some higher harmonics would be included. Thus, the waves are described as having the general form of

$$\eta_I(x,t) = \sum_{m=1}^{M} a_{Im} \cos(k_m x - 2\pi f_m t + \epsilon_{Im}), \tag{3.34}$$

$$\eta_R(x,t) = \sum_{m=1}^{M} a_{Rm} \cos(k_m x - 2\pi f_m t + \epsilon_{Rm}), \tag{3.35}$$

where η_I and η_R are the surface elevations of incident and reflected waves, k_m is the wave number of $2\pi/L_m$ with L_m being the wavelength of the mth regular wave, f_m is the wave frequency of the mth regular wave, and ϵ_{Im} and ϵ_{Rm} are the phase angles of the mth incident and reflected regular waves.

So, the surface elevations recorded at two adjacent stations of x_1 and $x_2 = x_1 + \Delta l$ will be

$$\eta_1 = (\eta_I + \eta_R)_{x=x_1} = \sum_{m=1}^{M} (A_{1m} \cos 2\pi f_m t + B_{1m} \sin 2\pi f_m t), \tag{3.36}$$

$$\eta_2 = (\eta_I + \eta_R)_{x=x_2} = \sum_{m=1}^{M} (A_{2m} \cos 2\pi f_m t + B_{2m} \sin 2\pi f_m t), \tag{3.37}$$

where

$$\begin{aligned} a_I(m) = (\eta_I + \eta_R)_{x=x_1} = \frac{1}{2|\sin k_m \Delta l|} [&(A_{2m} - A_{1m} \cos k_m \Delta l - B_{1m} \cos k_m \Delta l)^2 \\ &+ (B_{2m} + A_{1m} \sin k_m \Delta l - B_{1m} \cos k_m \Delta l)^{1/2}], \end{aligned} \tag{3.38}$$

$$\begin{aligned} a_R(m) = (\eta_I + \eta_R)_{x=x_1} = \frac{1}{2|\sin k_m \Delta l|} [&(A_{2m} - A_{1m} \cos k_m \Delta l - B_{1m} \cos k_m \Delta l)^2 \\ &+ (B_{2m} - A_{1m} \sin k_m \Delta l - B_{1m} \cos k_m \Delta l)^{1/2}], \end{aligned} \tag{3.39}$$

where the amplitude of A_{1m}, B_{1m}, A_{2m} and B_{2m} can be solved with the use of Fourier analysis for the fundamental frequency as well as for higher harmonics. By the definition of reflection coefficients, which is the ratio of the amplitude of reflected waves a_R to that of the incident waves a_I, the mean reflection coefficient can be written

$$K_R = [\sum_{m=1}^{M} a_R^2(m) / \sum_{m=1}^{M} a_I^2(m)]^{1/2}, \tag{3.40}$$

For monochromatic waves, the wave frequency is a fixed value, so the equation can be simple where $M = 1$. One point that should be noticed is that the distance between the two locations of x_1 and x_2 needs to be designed correctly. Goda's two-point method is useful only when $\Delta l \neq nL/2$ or the results would diverge. The spacing between two wave gauges should be varied from 0.05 L_{max} to 0.45 L_{min}, hence the maximum wavelength (minimum wave frequency) and minimum wavelength (maximum wave frequency) could be measured. Moreover, three wave gauges can be adopted for more complicated wave conditions, where the surface wave elevation at three locations is recorded. Then the incident and reflected wave can be analyzed using the least squares method.

The other computation of the reflection coefficients is based on the analytical method method (Wang et al., 2003). This method is not limited by the phase difference and two wave gauges $\eta(x_1, t)$ and $\eta(x_2, t)$ are enough to process the calculation. For regular waves, the incident and reflected waves are assumed to be

$$\eta_I = a_I \cos(\omega t - kx + \theta_I), \tag{3.41}$$

$$\eta_R = a_R \cos(\omega t - kx + \theta_R), \tag{3.42}$$

where θ_I and θ_R refer to the phase angles. Due to the linear superposition of surface elevations, $\eta(x_1, t)$ and $\eta(x_2, t)$ are expressed as

$$\eta(x_1, t) = a_I \cos(\omega t - kx_1 + \theta_I) + a_R \cos(\omega t + kx_1 + \theta_R), \tag{3.43}$$

$$
\begin{aligned}
\eta(x_2,t) &= a_I\cos(\omega t - kx_2 + \theta_I) + a_R\cos(\omega t + kx_2 + \theta_R) \\
&= a_I\cos(\omega t - kx_1 + \theta_I - k\triangle x) + a_R\cos(\omega t + kx_1 + \theta_R + \triangle x),
\end{aligned}
\tag{3.44}
$$

Let $x_2 = x_1 + \triangle x$, so that Eqs.3.43-3.44 can be reduced to the equation with x_1. Besides, They can be written in the complex form as

$$
\eta(x_1,t) = a_I e^{i(\omega t - kx_1 + \theta_I)} + a_R e^{i(\omega t + kx_1 + \theta_R)}, \tag{3.45}
$$

$$
\eta(x_2,t) = a_I e^{i(\omega t - kx_1 + \theta_I)} e^{-ik\triangle x} + a_R e^{i(\omega t + kx_1 + \theta_R)} e^{ik\triangle x}, \tag{3.46}
$$

From Eqs.3.45-3.46, we obtain the surface elevation of the incident and reflected waves:

$$
\eta_I(x,t) = a_I e^{i(\omega t - kx_1 + \theta_I)} = \frac{e^{ik\triangle x}\eta(x_1,t) - \eta(x_2,t)}{2i\sin(k\triangle x)}, \tag{3.47}
$$

$$
\eta_R(x,t) = a_R e^{i(\omega t + kx_1 + \theta_I)} = \frac{e^{-ik\triangle x}\eta(x_1,t) - \eta(x_2,t)}{-2i\sin(k\triangle x)}, \tag{3.48}
$$

$$
K_r = \frac{a_R}{a_I} = \frac{\left\|e^{-ik\triangle x}\eta(x_1,t) - \eta(x_2,t)\right\|}{\left\|e^{ik\triangle x}\eta(x_1,t) - \eta(x_2,t)\right\|}, \tag{3.49}
$$

It should be noticed that the surface elevations recorded at positions x_1 and x_2 need to be transformed into a complex form by taking a Hilbert transform. The reflection coefficients of the higher harmonic waves can also be computed similarly as long as the input surface elevations $\eta(x_1,t)$ and $\eta(x_2,t)$ are replaced by $\eta_m(x_1,t)$ and $\eta_m(x_2,t)$ where m denotes the mth harmonics. Note that the higher harmonic reflection coefficients are defined by the ratio of the harmonic amplitudes to the nonlinear wave amplitude. Extraction of the harmonics can be realized by the FFT technique and the reflection coefficients of the harmonics can be written as

$$K_{rm} = \frac{a_{Rm}}{a_I} = \frac{\left\| e^{-ik_m \triangle x} \eta_m(x_1, t) - \eta_m(x_2, t) \right\|}{\left\| e^{ik \triangle x} \eta(x_1, t) - \eta(x_2, t) \right\|}, \tag{3.50}$$

3.5.3 Separation of superharmonics

In order to examine the subharmonics and superharmonics in the temporal domain's evolution at different locations, we separate the signals using frequency-domain filtering. This part assesses the release of wave harmonics due to nonlinear monochromatic waves transitioning over a submerged step. It validates the numerical model by comparing the extracted superharmonics from the simulations to those from experimental observations.

Frequency domain filters were applied to separate the linear, subharmonic and superharmonic components of the surface elevations. These were implemented by taking a single-sided Fast Fourier Transform (FFT) of the surface elevation and then an inverse FFT (IFFT) of the frequency components allocated to the harmonics. The lower and higher frequency bounds of these harmonics are taken, considering the range of the input spectrum, as

$$f_N = N f_0 \pm 2\sigma, \tag{3.51}$$

where $N = 0, 1, 2$ for subharmonic, linear, and superharmonic wave components, respectively. σ refers to the selected range of the frequency.

The decomposition of higher components is significant for investigating the variation of superharmonics. The Fast Fourier Transform (FFT) is a common method for transforming temporal data into spectral data, especially for monochromatic waves, where the higher harmonics can be found with $f = nf_p$ ($n = 2, 3...$). However, each harmonic overlaps in the focused wave groups due to a wide frequency range. For instance, the frequency range of the second superharmonics $f_2 = (0.6 - 3.6)f_p$ contains part of the fundamental ones $f_1 = (0.3 - 1.8)f_p$. Thus, the phase-manipulation approach is employed to decompose each harmonic. It enables the separation of at least the first fourth harmonics.

The nonlinear surface elevation η contains the superharmonics ($m = n$) and the subharmonics ($m - n = 2$). An expansion of free surface can be written

$$\eta = AS_{11}\cos\phi + A^2(S_{20} + S_{22}\cos 2\phi) + A^3(S_{31} + S_{33}\cos 3\phi) \\ + A^4(S_{40} + S_{42}\cos 2\phi + S_{44}\cos 4\phi) + O(A^5), \tag{3.52}$$

where the coefficients S_{mn} denote the value of harmonics, $\phi = \omega t + \phi_0$ refers to the phase of the linear component, and ϕ_0 is the initial phase set at the beginning. The phase-manipulation approach extracts each harmonic with a certain increment in the initial phase $\phi_0 = 0°, 90°, 180°$ and $270°$. Then, the combination of surface elevations with different can separate superharmonic waves, the decomposed surface elevation of the first four superharmonics are

$$\eta_1 = (A_{in}S_{11} + A_{in}^3 S_{31})\cos\omega t = (\eta_0 - \eta_{90}^H - \eta_{180} + \eta_{270}^H)/4, \tag{3.53}$$

$$\eta_2 = (A_{in}^2 S_{22} + A_{in}^4 S_{42})\cos 2\omega t = (\eta_0 - \eta_{90} + \eta_{180} - \eta_{270})/4, \tag{3.54}$$

$$\eta_3 = A_{in}^3 S_{33}\cos 3\omega t = (\eta_0 + \eta_{90}^H - \eta_{180} - \eta_{270}^H)/4, \tag{3.55}$$

$$\eta_{20} + \eta_4 = A_{in}^2 S_{20} + A_{in}^4 S_{40} + A_{in}^4 S_{44}\cos 4\omega t = (\eta_0 + \eta_{90} + \eta_{180} + \eta_{270})/4, \tag{3.56}$$

where the superscript H denotes the Hilbert transform of the surface elevations. Note that the fourth harmonics contains the subharmonics η_{20}, referring to the variation of the mean water line. Based on the phase-manipulation method, the components of subharmonics and fourth harmonics are easily separated with FFT and the subharmonics are identified near 0 Hz.

3.5.4 Separation of second bound and free waves

Except for separating superharmonics, the decomposition of the higher free and bound waves is also a problem to solve. The superharmonics normally represent the higher bound (locked) waves with the same velocity as the fundamental components. Water depth variation leads to higher bound waves (locked waves) and free waves. For the former, the frequency is the n times peak frequency $f_{n,b} = nf_p$, the higher superharmonics normally mentioned. The bound waves have the same phase speed as fundamental harmonics $c_{n,b} = c_1$, and the wavenumber $k_{n,b}$ equals n times nk_1. Newly free waves are generated in the spatial domain by meeting the relation $(n\omega_1)^2 = gk_{n,f}\tanh(k_{n,f}h_s)$, h_s is the water depth in the shallower region. As a result, the phase speed of higher free waves is slower than that of bound waves $c_{n,f} < c_{n,b}$, which have the same frequencies $f_{n,f} = f_{n,b}$. For instance, the ADT induces higher components of the same frequency of bound waves but different velocities ($f_{2,b} = f_{2,f} = 2f_1, c_{2,b} \neq c_{2,f}$). The dispersion relations $D(\omega)$ calculating the wavenumber of second bound $k_{2,b}$ and free waves $k_{2,f}$ in the shallower regions

h_s are $2D(\omega)$ and $D(2\omega)$, respectively

$$k_{2,b} = 2k_1, \tag{3.57}$$

$$(2\omega)^2 = gk_{2,f} \tanh k_{2,f} h_s, \tag{3.58}$$

due to the same frequency of the free and bound waves, the higher free and bound waves cannot be separated from the frequency domain with the FFT or phase-manipulation method. Only the fundamental wave components and higher free waves meet the dispersion relation, while higher bound waves have angular frequencies and wavenumbers that are multiples of the fundamental components, and the characteristics of free waves vary with water depth.

A separation technique based on surface elevations at four wave gauges are adopted (Lin and Huang, 2004). The surface elevations $\eta(x,t)$ at each position can be expressed as

$$\begin{aligned}
\eta(x_p,t) = {} & A_I^1(\cos kx_p - \omega t + \phi_I^1) + A_R^1(\cos kx_p + \omega t + \phi_R^1) \\
& + \sum_{m\geq 2} A_{I,B}^m \cos\left[m(kx_p - \omega t) + \phi_{I,B}^m\right] + \sum_{m\geq 2} A_{R,B}^m \cos\left[m(kx_p + \omega t) + \phi_{R,B}^m\right] \\
& + \sum_{m\geq 2} A_{I,F}^m \cos\left[m(kx_p - \omega t) + \phi_{I,F}^m\right] + \sum_{m\geq 2} A_{R,F}^m \cos\left[m(kx_p + \omega t) + \phi_{R,F}^m\right] + e_p(t),
\end{aligned} \tag{3.59}$$

where A denotes the amplitude of waves, the subscripts B and F denote the bound and free wave components, respectively. x_p represents the location in the spatial domain. The subscript m ($m = 1, 2, ...$) refers to the mth harmonic waves. ϕ^m denotes the phase difference in an arbitrary time domain. The final $e_p(t)$ is associated with the extra signal noise of nonlinear wave interactions. Then, the surface elevations

$\eta(x_p, t)$ can be decomposed with FFT as

$$\tilde{\eta}^m(x_p) = \frac{\omega}{2\pi}\int_0^{(2\pi/\omega)} \eta(x_p, t)e^{-im\omega t}dt, \tag{3.60}$$

By substituting Eqs. 3.59 into 3.60 and assume $m = 1$, the transformed surface elevations can be written as

$$\tilde{\eta}^1(x_p) = C_I^1 X_I^1 + C_R^1 X_R^1 + T_p^1, \tag{3.61}$$

where

$$X_I^1 = A_I^1 e^{-i(kx_1+\phi_I^1)}, \quad X_R^1 = A_R^1 e^{-i(kx_1+\phi_R^1)},$$

$$C_I^1 = \frac{e^{-ik\Delta x_p}}{2}, \quad C_R^1 = \frac{e^{ik\Delta x_p}}{2},$$

The fast Fourier transform of $e_m(t)$ at $m = 1$ and the position of wave gauge x_1 is displayed as T_p^1. Δx_p denotes the distance between the first wave gauge and the mth wave gauge. The sum of T_p^1 can be minimized using the least squares method to choose the parameters X_I^1 and X_R^1, namely the minimum sum

$$\sum_p [T_p^1]^2 = \sum_p [\tilde{\eta}^1(x_p) - C_I^1 X_I^1 - C_R^1 X_R^1]^2, \tag{3.62}$$

The solution of parameters X_I^1 and X_R^1 can be obtained by minimizing their total errors,

$$\frac{\partial \sum_p [T_p^1]^2}{\partial X_I^1} = O, \quad \frac{\partial \sum_p [T_p^1]^2}{\partial X_R^1} = O, \tag{3.63}$$

where the algebraic equations can be simplified as

$$\begin{bmatrix} A_{11} & A_{12} \\ A_{21} & A_{22} \end{bmatrix} \begin{bmatrix} X_I^1 \\ X_R^1 \end{bmatrix} = \begin{bmatrix} B_1 \\ B_2 \end{bmatrix}, \tag{3.64}$$

The study by Lin and Huang provides the solution for components $A_{i,j}$ and B_i. The amplitudes of the first harmonics can be determined

$$A_I^1 = \left|X_I^1\right|, \quad A_R^1 = \left|X_R^1\right|, \tag{3.65}$$

Similarly, the singularity should be avoided in the physical application. For four different wave gauges before the first depth transition, the Eq. 3.66 is determined

$$[\frac{1}{4} + \frac{e^{-2ik\Delta x_2}}{4} + \frac{e^{-2ik\Delta x_3}}{4}\frac{e^{-2ik\Delta x_4}}{4}] \times [\frac{1}{4} + \frac{e^{2ik\Delta x_2}}{4} + \frac{e^{2ik\Delta x_3}}{4}\frac{e^{2ik\Delta x_4}}{4}] - 1 = 0, \tag{3.66}$$

To achieve the amplitude of the first harmonics, the same steps are employed for the superharmonic waves by substituting Eq. 3.59 into 3.60 with $m \geq 2$. Consequently, the transformation of $\eta(x_p, t)$ is modified to

$$\tilde{\eta}^m(x_p) = C_{I,B}^m X_{I,B}^m + C_{R,B}^m X_{R,B}^m + C_{I,F}^m X_{I,F}^m + C_{R,F}^m X_{R,F}^m + T_p^m, \tag{3.67}$$

$$A_{I,B}^m = \left|X_{I,B}^m\right|, \quad A_{R,B}^m = \left|X_{R,B}^m\right| A_{I,F}^m = \left|X_{I,F}^m\right|, \quad A_{R,F}^m = \left|X_{R,F}^m\right|, \tag{3.68}$$

Through the phase-manipulation approach, amplitudes of higher harmonics can be obtained. To further extract the wave profiles of second bound and free waves, the continuous wavelet transform (CWT) is introduced to process the data in both temporal and frequency domains. The different times of generation and velocities of free and bounds make it possible to separate them from the spatio-temporal information with the CWT.

In the time domain, the wavelet coefficients can be obtained by comparing the window signals at different positions one by one by moving the wavelet in time. The larger wavelet coefficient shows a better fitting degree between the wavelet and the segment signal. In the calculation, the convolution of the wavelet function and the signal in the window is used as the wavelet coefficient under the window. The length of the window and the length of the wavelet are the same. In addition, in the frequency domain, by stretching or compressing the length of the wavelet, the length and frequency of the wavelet are changed, and the wavelet coefficients under different frequencies are realized. Accordingly, the window length also varies with the wavelet length. Since the wavelets are compressed at high frequencies, the time window becomes narrower, resulting in a higher temporal resolution. The spatio-temporal wavelet coefficient map is obtained by combining the wavelet coefficients at different frequencies. In wavelets, scale is generally used to measure the frequency f of wavelets, and the conversion relationship between the two is as follows

$$s * f = f_s * wcf, \tag{3.69}$$

where the sample frequency $f_s = 1/\Delta t$, the wcf denotes the wave central frequency. With the decomposed second harmonics above, the spatio-temporal data of second superharmonics is obtained with the CWT. Then the separated second bound and free harmonics in the time domain can be inverted to the surface elevations. The CWT and inverse continuous wavelet transform (ICWT) adopt the adaptive solver available in many common software packages.

3.5.5 Skewness and kurtosis of surface elevations

The parameters skewness and kurtosis can be useful in describing the degree of deviation of the surface elevations and wave heights. In terms of the surface elevation η, the definitions of skewness and kurtosis are

$$\lambda_3 = \left\langle (\eta - \langle\eta\rangle)^3 \right\rangle / \eta_{std}^3, \quad \lambda_4 = \left\langle (\eta - \langle\eta\rangle)^4 \right\rangle / \eta_{std}^4, \tag{3.71}$$

where η_{std} is the standard deviation of the surface elevation, $<>$ represents the averaged value. The values are $\lambda_3 = 0$ and $\lambda_4 = 3$ for Gaussian waves. There is a clear increase in the values in the shallower regions (Li et al., 2021c), inducing a higher probability of the occurrence of extreme waves during the abrupt depth transitions. Note that the values of these two parameters vary with the type of wave.

3.6 Summary

This chapter first reviews and presents the theoretical model of different types of waves in constant water depth and the establishment of the fully nonlinear numerical model. A detailed description of the laboratory wave tank and associated facilities is introduced. The numerical model is well validated with the measured data before its application in studying nonlinear wave propagation. Various methodologies to decompose the subharmonics and superharmonics are provided. In addition, the FFT is utilized specifically for monochromatic waves. For wave groups that encompass a wide frequency range, the implementation of a phase-manipulation approach is necessitated. The CWT serves as an additional approach in cases where the separation of the second bound and free waves is required. The Goda two-point method calculates the reflection coefficients of waves. Moreover, with the inclusion of sub and superharmonics, the four-point method can capture more comprehensive spectra of each harmonic. Lastly, the skewness and kurtosis values provide a statistical perspective on the degree of wave profile asymmetry. It provides solid mathematical, numerical and experimental backgrounds for the following studies.

Chapter 4

Behavior of superharmonics of monochromatic waves on ADTs

4.1 Introduction

In the past ten years, there has been considerable engineering and scientific interest in the probability of large waves occurring on the coastline. A number of studies have suggested that a transition of water depth could play an important role in an enhanced occurrence probability of extreme waves (Majda et al., 2019; Trulsen, 2018). Research about the wave propagation over the varying bottom is various and quantitative. However, these studies refer to different purposes. For instance, most articles with different bottoms mainly focus on the breakwater to explore a more effective shape (Chang and Liou, 2007; Ji et al., 2017; Stamos et al., 2003). In addition, some research observes the wave propagation over a certain water depth area or two continual transmitted areas like shallow water, shallow-to-deep water (Baldock et al., 1996; Galan et al., 2012). These groups mainly focus on the parameters and characteristics of the wave propagation to improve the wave nonlinear analysis and propose a higher solution to nonlinear wave equations. As this new potential mechanism of extreme waves was proposed in the past decades, only limited studies investigated the nonlinear wave propagation on the ADTs (Moore et al., 2020; Viotti and Dias, 2014; Zhang and Benoit, 2021). To investigate the hydrodynamic characteristic of transition is necessary.

The objective of the work is to investigate the importance of higher harmonics of nonlinear water waves propagating on abrupt depth transitions with efficient numerical simulations and an experimental campaign. Within the framework of potential flow theory, a fully nonlinear model is established to describe the wave evolution on varying bathymetries by a conformal mapping method. Monochromatic waves with varying incident frequencies and steepness are studied to examine the changes in the superharmonics on the lee side and top of the submerged step, especially for the second and third harmonics. We analyze the evolution of wave spectra in both the time and spatial domains to extract the higher harmonics. Two different water depths are employed to study the effects of the water depth ratio of the sea bed to the step on the superharmonics. In addition, the nonlinear evolution of wave elevations over the step is discussed regarding kurtosis and skewness. The study of monochromatic waves was conducted to facilitate the extraction and analysis of each harmonic's propagation, providing a clearer understanding of superharmonics evolution during strong nonlinear wave propagation, which was later applied to more complex nonlinear wave groups.

The organization of the chapter is as follows. The experimental set-up and the numerical model based on the conformal mapping method are described in Sections 4.2 and 4.3, respectively. Convergence and validation of the numerical model are also presented. Wave reflection considering the fundamental and the higher harmonics are present in Section 4.4. Then, the results of the nonlinear propagation of superharmonics are discussed (in Section 4.5), in particular, the dynamic characteristics of the higher harmonics over the abrupt depth transitions in both the time and spatial domains with both experimental measurements and numerical simulations. Section 4.6 focuses on the distribution of the wave profile parameters in the spatial domain and discusses the effects of water depth on the nonlinear wave evolution. The evolution of skewness and kurtosis of monochromatic waves on ADTs is described in Section 4.7. Section 4.8 presents the concluding remarks.

4.2 Experimental set-up

The experiments were conducted in the wave tank located at the Hydraulics Laboratory of the Hong Kong Polytechnic University with a length of 27 m, a width of 0.75 m and a depth of 1.5 m. A piston-type wavemaker is equipped to generate both monochromatic and irregular waves. At the end of the physical tank, a wave absorber is arranged to dissipate energy, as shown in Figure 4.1. The front face of the submerged step was installed 4 m away from the wavemaker providing two depth transitions in the x-axis (same direction as the wave propagation). The water depth in the deeper region is denoted as h1, and in the shallower region as h2. The size of the submerged step is fixed with a length of 2.4 m, a width of 0.75 m and

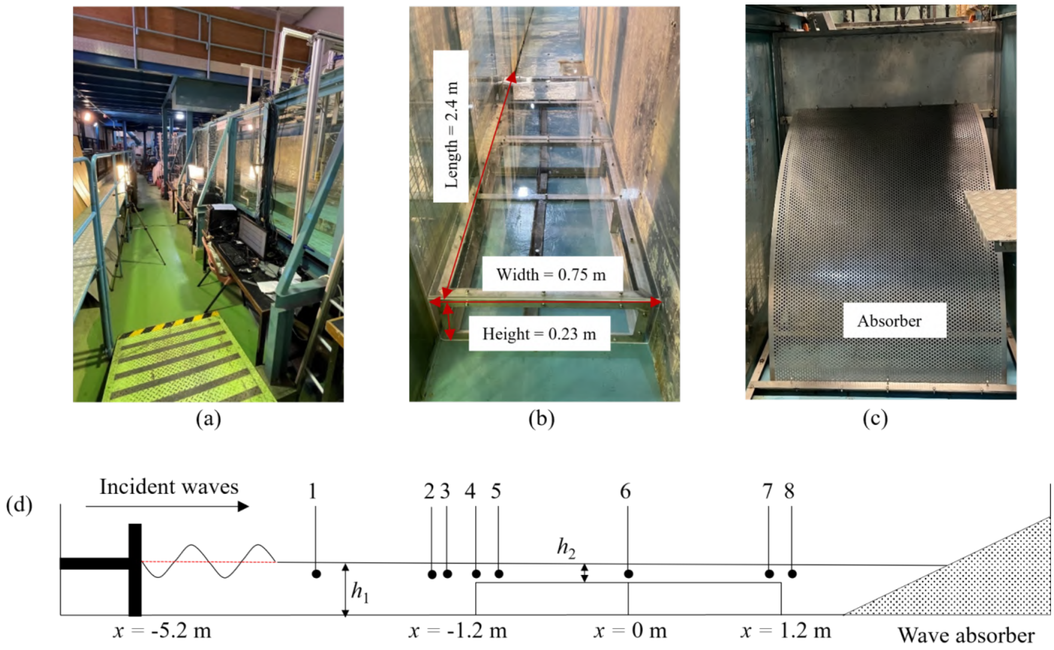

Figure 4.1: (a) Laboratory wave tank; (b) stainless rectangular step; (c) wave absorber and (d) sketch of the experimental set-up (not in correct scale for tank length).

a height of 0.23 m. The value of h_2/h_1 is thus adjusted with the water depth h_1. Eight capacitive wave gauges were used. The origin of the coordinate system is at the center of the step. The positions of WG 1 to WG 8 are listed in Table 4.1. We set h_1 to be 0.36 m or 0.48 m. The detailed parameters of the tested cases are shown in Table 4.2.

Let f_0 be the incident wave frequency, k_1 the wave number on the deeper region and k_2 the wave number on the shallower one. Then $k_1 a$ denotes the wave steepness where the wave amplitude a is half the wave height $a = H/2$. The cases with $h_1 = 0.48$ m are denoted with a star (cases 5* and 6*). A high-resolution camera was placed along the tank to capture the wave profiles. The evolution of monochromatic waves, as depicted in Figure 4.2, is examined using a higher frequency of $f_0 = 1.33$ Hz to clearly illustrate the changes in wave shapes at the shorter wave-

Table 4.1: Locations of the eight wave gauges shown in Figure 4.1.

WG No.	WG 1	WG 2	WG 3	WG 4	WG 5	WG 6	WG 7	WG 8
Position (m)	-2.2	-1.56	-1.4	-1.2	-1.0	0	1.1	1.3

length. A comparison with the incident wave profile reveals that the profiles in shallower regions exhibit an asymmetric crest with increased sharpness at the first depth transition. This observation underscores the nonlinear effects in the spatial domain. A comprehensive analysis of the nonlinear characteristics, utilizing both experimental and numerical results, is elaborated upon in the subsequent sections.

4.3 Numerical method

This section presents the numerical set-up and the validation with experimental measurements. In the pre-processing, the equations are non-dimensionalized by using g as unit acceleration and h_1 as unit length. Thus the two dimensionless input parameters, amplitude and wavelength, are a/h_1 and L/h_1. In this case, the dimensions in the numerical simulation have been reduced. This pre-processing is required before analyzing the numerical results. In the fully nonlinear numerical model, an absorbing condition is added to minimize the influence of periodic boundary conditions. A linear damping is implemented by a shape function, which reduces the velocity potential at the right boundary (wave absorption). Hence rare influence will be on the surface waves propagating from the left side (wave generation).

The main tested cases are shown in Table 4.2. It consists of two steps with the ratio $h_2/h_1 = 0.36$ and 0.52. The incident wave frequency ranges from 0.94 Hz to 1.64 Hz. The incident wave steepness k_1a was carefully selected and tested to make sure the effects on the higher harmonics can be captured. For all the tested

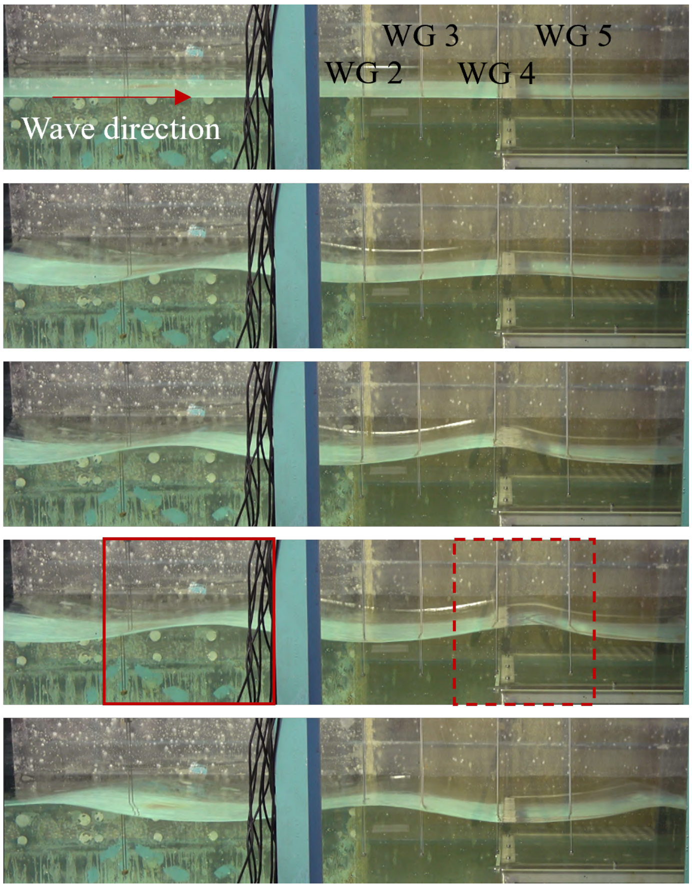

Figure 4.2: Surface profiles of the monochromatic wave along with the tank at the first ADT.

cases with the step in the wave flume, we have also generated pure waves without the step. This is to ensure we can obtain accurate information on the incident wave. The physical amplitude a has been modified with the experiments on the constant depth.

4.3.1 Convergence of numerical model

To capture strong nonlinearities during wave evolution, a sufficient number of Fourier terms or points per wavelength should be used in numerical simulations. The variation of surface elevations η is shown in Figure 4.3 with 6 different num-

Table 4.2: Test parameters. The ratios h_2/h_1 of water depths in the shallower region h_2 to that of the deeper region h_1 are 0.36 and 0.52, respectively. f_0 is the incident frequency. The wave number k_1 for the monochromatic waves is computed from the stream function using the wave conditions on the deeper region with h_1. a is the incident measured wave amplitude. k_2 is derived by the stream function with the incident amplitude a and shallower region h_2. (* refers to the cases with h_1 = 0.48 m.).

Case	h_1(m)	h_2/h_1	f_0(Hz)	k_1a	k_1h_1	k_2h_2
1	0.36	0.36	0.94	0.06	1.434	0.736
2	0.36	0.36	0.94	0.10	-	-
3	0.36	0.36	1.21	0.13	2.783	1.001
4	0.36	0.36	1.45	0.15	3.059	1.280
5*	0.48	0.52	0.91	0.10	1.708	1.059
6*	0.48	0.52	1.64	0.23	5.196	2.725

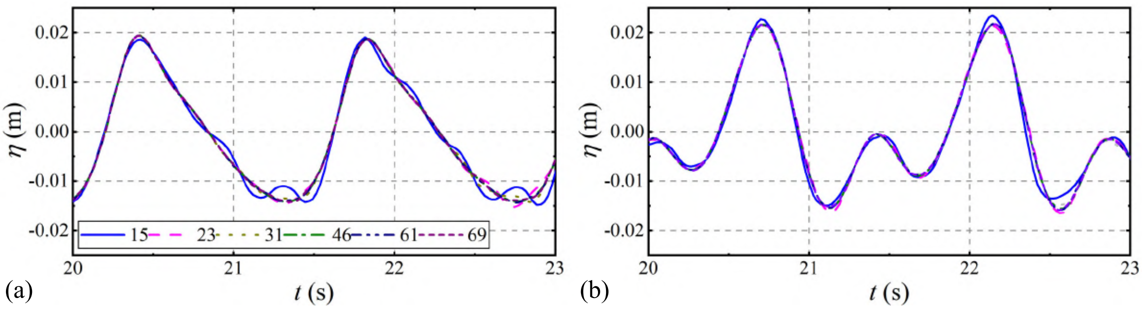

Figure 4.3: Model convergence with different numbers of Fourier terms per wavelength: (a) $x = -0.35$ m and (b) $x = 1.42$ m.

bers (10 to 70) of Fourier discrete points per wavelength The wave profiles over two wave periods indicate that the results with 31 and 69 discrete numbers show good agreement. These wave profiles are highly nonlinear because they are located on the shallower region ($x = 12.05$ m and $x = 13.82$ m), which shows the capability of the numerical model for fully nonlinear simulations. In this study, 52 Fourier terms are chosen to investigate the wave evolution over the varying bathymetries. Further study of numerical convergence for higher harmonics is demonstrated.

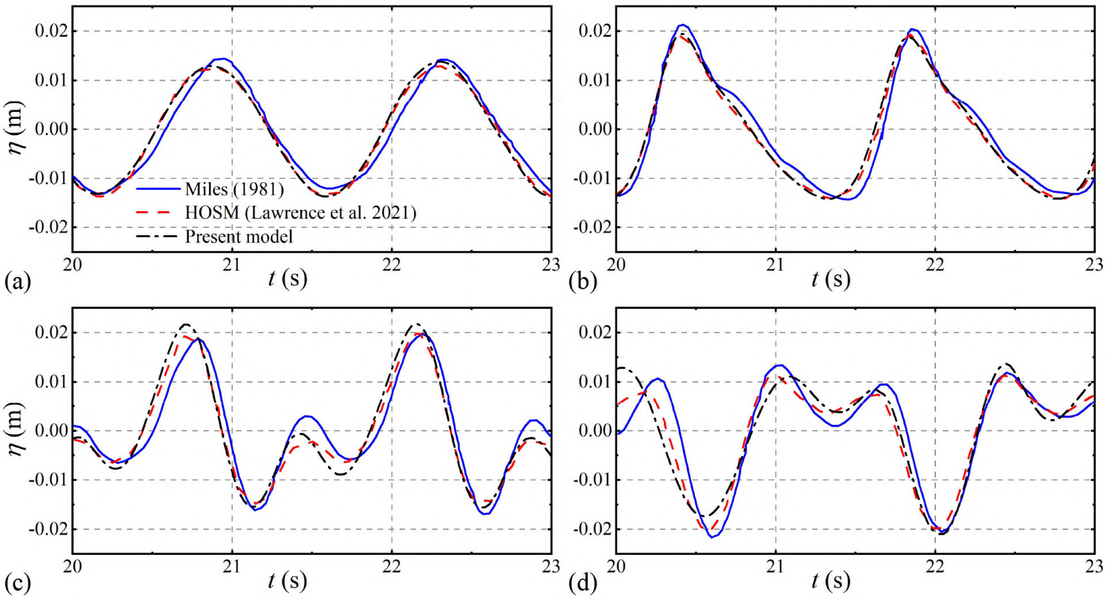

Figure 4.4: Surface elevations over a shoal (Lawrence et al., 2021) with $f_0 = 0.70$ Hz, $a = 0.0135$ m (a) $x = -1.57$ m; (b) $x = -0.35$ m; (c) $x = 1.42$ m and (d) $x = 2.45$ m.

4.3.2 Validation of numerical model

To verify our numerical model, wave profiles propagating over a shoal arising from the experimental measurements, numerical simulations using a higher-order spectral method (HOSM) and numerical simulations using the conformal mapping method are compared in Figure 4.4(a-b) at four different positions. Overall, the simulated data show good agreement with the numerical and experimental results. There are small discrepancies in the trough as can be seen in Figure 4.4(c-d). This can likely be attributed to the effects of bottom friction and dissipation from the sidewalls.

In addition, the nonlinear wave evolution for case 1 with a step of $h_2/h_1 = 0.36$ is compared between the experimental measurements and numerical simulations in Figure 4.5. The surface elevations at the 8 wave gauges are all shown in a time win-

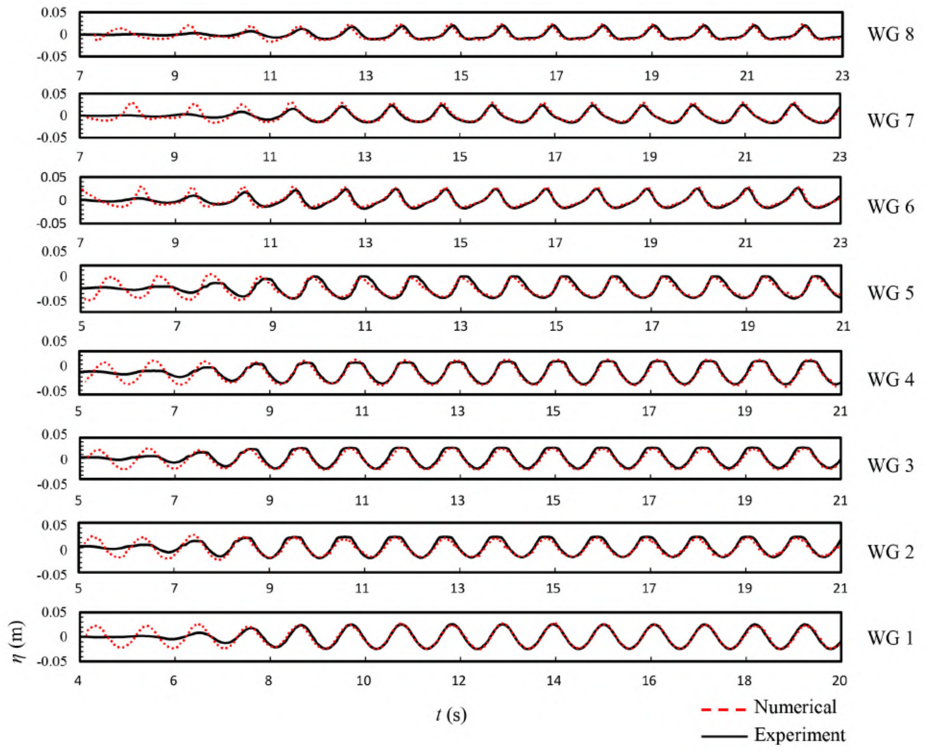

Figure 4.5: Comparison of experimental measurements and numerical results for the surface elevation at the 8 wave positions along the tank for case 1 $f_0 = 0.94$ Hz, $k_1 a = 0.06$.

dow covering 16 s. The agreement between the simulated and measured profiles is excellent. The characteristics of the surface elevations compare well with those of the experiments, especially for the sharp crests and flat troughs. We see that the wave is nearly linear at WG 1, and the nonlinearity increases in front of the step at WG 2-4. Near the center of the step, the nonlinearity becomes much stronger with distorted surface shapes. Note that there are discrepancies in the initial stage at each wave gauge position. The transient part at the beginning of the measurements is due to the build-up of the physical wavemaker motion, which is not modeled in the numerical simulations. Moreover, the comparison of wave profiles achieved by the experiments and numerical simulation is presented in Figure 4.6. The measured

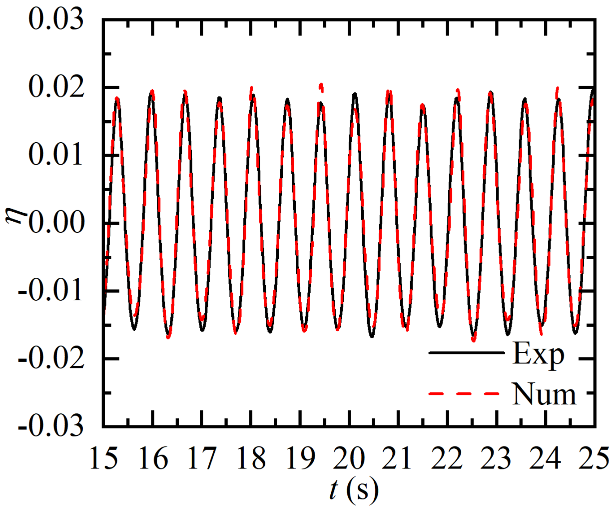

Figure 4.6: Comparison of wave profiles on the condition with the constant depth for case 4 $f_0 = 1.45$ Hz, $k_1 a = 0.15$.

data on the constant depth also well validate the numerical model. The possible unphysical flat crests in several measurements might be due to the unstable wave gauge performance. In all our tests, we repeated three times to reduce the errors as possible. In terms of computing reflection coefficients and spectral analysis of higher harmonics, comparisons in the later sections show that these might have minor effects on the linear reflection coefficient, and higher harmonics are not much influenced.

4.4 Reflection of monochromatic waves on ADTs

4.4.1 Fundamental wave reflection

This section presents the harmonic wave amplitudes of the experimental measurements and numerical simulations in the frequency and time domains. To access the wave nonlinearity induced by the abrupt depth transitions, the harmonic amplitudes are nondimensionalized by the incident wave amplitude measured at WG 1. In addition, all the tested cases refer to waves propagating over finite water depths with a time window of 10 to 30 seconds. This time window ensures sufficient wave records for a stationary state over the submerged step and no disturbance from the reflected waves from the end of the wave tank.

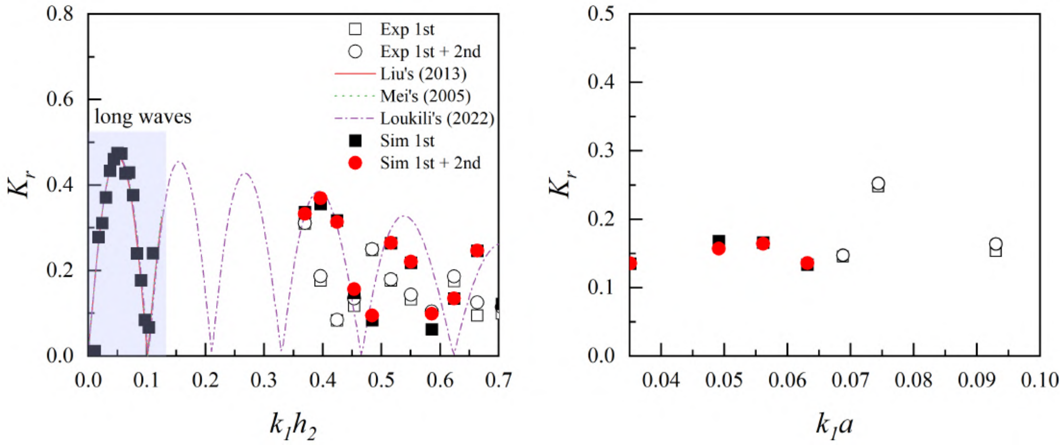

Figure 4.7: Reflection coefficients as a function of k_1h_2 and amplitude k_1a with $h_2/h_1 = 0.36$.

Figures 4.7 and 4.8 present the variation of reflection coefficients with increasing k_1h_2 and steepness k_1a. The wave reflection considers the linear and the second harmonics, respectively. The computation of the reflection coefficients with measured and numerical results is different. The experimental coefficients are obtained using the Goda two-point method, while the numerical simulations employ four wave gauges (Lin and Huang, 2004; Wang et al., 2003). The relative water depth k_1h_2 ranges from $0.35 - 0.70$ for $h_2/h_1 = 0.36$, and from $0.5 - 2.0$ for $h_2/h_1 = 0.52$. Compared with the theory of (Loukili et al., 2022), a good comparison can be found with the reflection coefficients obtained with numerical simulations and experiments. Meanwhile, the theoretical results from (Mei et al., 2005)

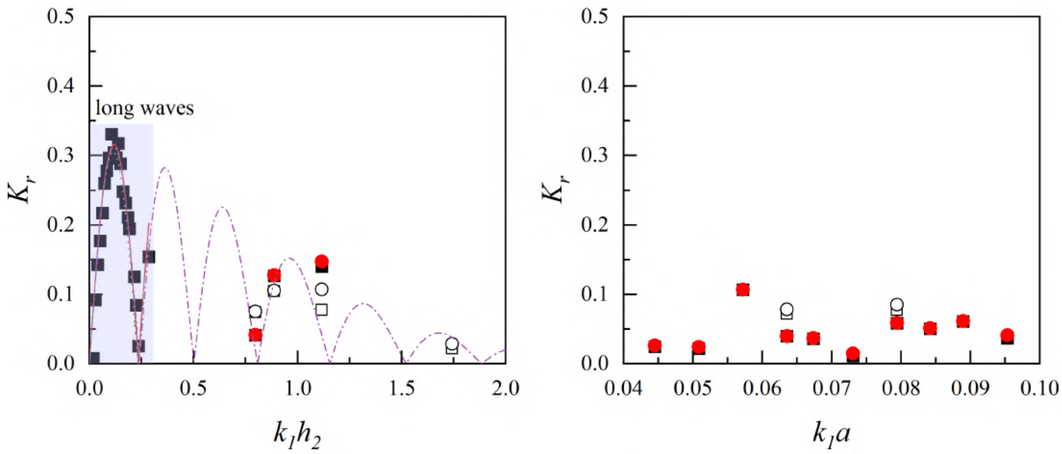

Figure 4.8: Reflection coefficients as a function of k_1h_2 and amplitude k_1a with $h_2/h_1 = 0.52$.

have also validated the numerical results and Loukili et al.' theory with long waves. The observed shift between the numerical and theoretical models is attributed to the distinct impacts of bottom and free-surface nonlinearities on frequency (Peng et al., 2022). These discrepancies arise from the assumption of a small wave amplitude in (Loukili et al., 2022)'s study. In contrast, this study employs a higher wave steepness. Specifically, bottom nonlinearity instigates a downshift, while free-surface nonlinearity provokes an upshift. The frequency shifts exhibit a quadratic dependence on steepness, inducing more pronounced upshifts. Thus, an increase in wave steepness augments nonlinearity. The increased incident steepness, k_1a, has a minor effect on the value of reflection coefficients. This could explain the slight discrepancy in coefficient values, rather than the trend of variation with increasing k_1h_2.

4.4.2 Wave reflection and transmission with second harmonics

The second components can be further categorized into bound (locked mode) and free waves (Andersen et al., 2017). The free waves propagate at their individ-

Table 4.3: Reflection and transmission coefficients for the linear and the first two harmonic components with varying $k_1 h_2$.

f_0(Hz)	$k_1 h_2$	a	$k_1 a$	K_{r1}	$K_{r1,2}$	K_{t1}	$K_{t1,2}$	E_1	$E_{1,2}$
0.74	0.370	0.018	0.05	0.337	0.332	1.026	0.678	1.165	0.570
0.78	0.396	0.011	-	0.356	0.369	1.035	0.816	1.200	0.802
0.82	0.424	0.015	-	0.317	0.314	1.032	0.742	1.166	0.649
0.86	0.453	0.014	-	0.147	0.156	1.093	0.771	1.217	0.619
0.90	0.484	0.013	-	0.084	0.095	1.075	0.761	1.162	0.588
0.94	0.516	0.015	0.06	0.265	0.265	1.043	0.758	1.158	0.645
0.98	0.550	0.014	-	0.218	0.221	1.036	0.750	1.121	0.611
1.06	0.624	0.015	0.07	0.135	0.135	1.047	0.742	1.114	0.569
1.10	0.664	0.014	-	0.246	0.247	0.981	0.695	1.023	0.543
0.85*	0.797	-	0.060	0.041	0.041	1.000	0.705	1.000	0.705
0.91*	0.888	-	0.068	0.127	0.128	0.997	0.706	1.009	0.515
1.04*	1.116	-	0.085	0.140	0.148	0.978	0.691	0.976	0.499

ual phase velocities as dictated by the dispersion relation. Due to the minor frequency difference between free and bound waves, separation from the spectrum using FFT is insufficient. The amplitudes of the second bound and free waves are separated using the four-wave gauges method to study the reflection and transmission of superharmonics (Lin and Huang, 2004). Table 4.3 and 4.4 present the results of transmission coefficients considering only the first and the sum of the first two harmonics. The transmission coefficients are defined as the ratio of the amplitude of transmitted waves to that of incident waves. The parameter E_1 is calculated as $E_1 = {K_{r1}}^2 + {K_{t1}}^2$, considering only the linear components.

Concerning the nonlinear effect, another parameter $E_{1,2}$ is defined as the sum of the first and second harmonic coefficients, $E_{1,2} = {K_{r1,2}}^2 + {K_{t1,2}}^2$. We see that E_1 is close to 1 for most cases, and $E_{1,2}$ is significantly less than 1, nearly half of E_1. Regarding the second harmonic waves, there are seldom any second components in the incident waves. However, the existence of abrupt depth triggers superharmonics.

Table 4.4: Reflection and transmission coefficients for the linear and the first two harmonic components with varying $k_1 a$.

f_0(Hz)	$k_1 h_2$	a	$k_1 a$	K_{r1}	$K_{r1,2}$	K_{t1}	$K_{t1,2}$	E_1	$E_{1,2}$
0.86	0.455	0.010	0.035	0.135	0.136	1.085	0.765	1.194	0.604
-	-	0.014	0.049	0.147	0.156	1.093	0.771	1.217	0.619
-	-	0.016	0.056	0.166	0.164	1.082	0.759	1.198	0.602
-	-	0.018	0.063	0.134	0.136	1.035	0.7221	1.089	0.540
0.85*	0.595	0.010	0.032	0.088	0.088	1.013	0.716	1.034	0.521
-	-	0.014	0.045	0.025	0.026	1.005	0.710	1.011	0.505
-	-	0.016	0.051	0.022	0.024	1.007	0.711	1.015	0.506
-	-	0.018	0.057	0.107	0.107	1.010	0.714	1.031	0.520
-	-	0.020	0.064	0.040	0.040	1.003	0.708	1.007	0.503
-	-	0.0212	0.067	0.036	0.037	1.006	0.710	1.013	0.505
-	-	0.023	0.073	0.011	0.015	1.003	0.707	1.005	0.500
-	-	0.025	0.079	0.058	0.059	1.003	0.708	1.010	0.505
-	-	0.0265	0.084	0.050	0.051	1.001	0.706	1.004	0.501
-	-	0.028	0.089	0.061	0.061	0.996	0.703	0.995	0.498
-	-	0.030	0.095	0.038	0.041	1.001	0.707	1.004	0.502
-	-	0.035	0.111	0.079	0.079	0.962	0.682	0.932	0.472

As mentioned before, bound waves dissipate after propagating over the second depth transition, but free waves continue to evolve forward. The reflection coefficients are nearly identical, whether considering only the first harmonic wave or both the first and second harmonic waves. However, considering second harmonics might lower the value of coefficients $K_{t1,2}$ and $E_{1,2}$.

4.4.3 Wave reflection of second bound and free waves

Table 4.5 shows the components of the second order, including the second super-harmonics (two points method) and the second free and bound waves (four points method). It is observed that the amplitudes of the isolated second bound $A^2_{I,B}$ and free waves $A^2_{I,F}$ surpass those of the general second harmonic components A^2_I. A disparity is also noticeable when comparing the ratio of reflected to incident waves, but it is found that the value of second components A^2_R/A^2_I is closer to the free waves

Table 4.5: The separated free and bound components in three cases.

f_0 (Hz)	k_1a	A_I^2 (mm)	A_R^2 (mm)	$A_{I,B}^2$ (mm)	$A_{R,B}^2$ (mm)	$A_{I,F}^2$ (mm)	$A_{R,F}^2$ (mm)	A_R^2/A_I^2	$A_{R,B}^2/A_{I,B}^2$	$A_{R,F}^2/A_{I,F}^2$
0.94	0.06	0.824	0.192	3.836	1.059	2.664	0.707	0.233	0.276	0.265
1.06	0.07	0.851	0.376	2.352	0.216	1.303	0.514	0.442	0.092	0.395
0.91*	0.10	1.407	0.324	3.277	0.613	1.608	0.710	0.230	0.187	0.442

$A_{R,F}^2/A_{I,F}^2$. This may be attributed to that the generation of superharmonics is predominantly concentrated in regions characterized by abrupt depth transitions and shallower areas, leading to less reflection before the step.

4.5 Nonlinear evolution of superharmonics

The spatial characteristics of the measured and simulated waves over the abrupt depth transitions are discussed in this section. Figure 4.9 displays the spatial evolution of wave profiles over a distance of 15 m with numerical simulations for four selected cases. $(x, \eta/\eta_0)$ is a Cartesian coordinate system where the left vertical axis η/η_0 shows the normalized surface elevation and the right axis indicates the time instants. In the simulations, the steady state is achieved after about 5 seconds. For the case $f_0 = 0.94$ Hz with the water depth ratio $h_2/h_1 = 0.36$, the depth change is relatively large at the first ADT such that linear dispersion relation might dominate the wave profile change for a non-deep water wave. We can see the profile distortion on the step and behind the step at 5 s, consistent with the study of (Massel, 1983). A similar trend is observed for $f_0 = 1.21$ Hz though it is a shorter wave. The distortion and large profile transformation of waves over an ADT have been reported by several authors (Giniyatullin et al., 2014; Kurkin et al., 2015). For the larger water depth ratio $h_2/h_1 = 0.52$, the profile transformation over the ADT seems insignificant

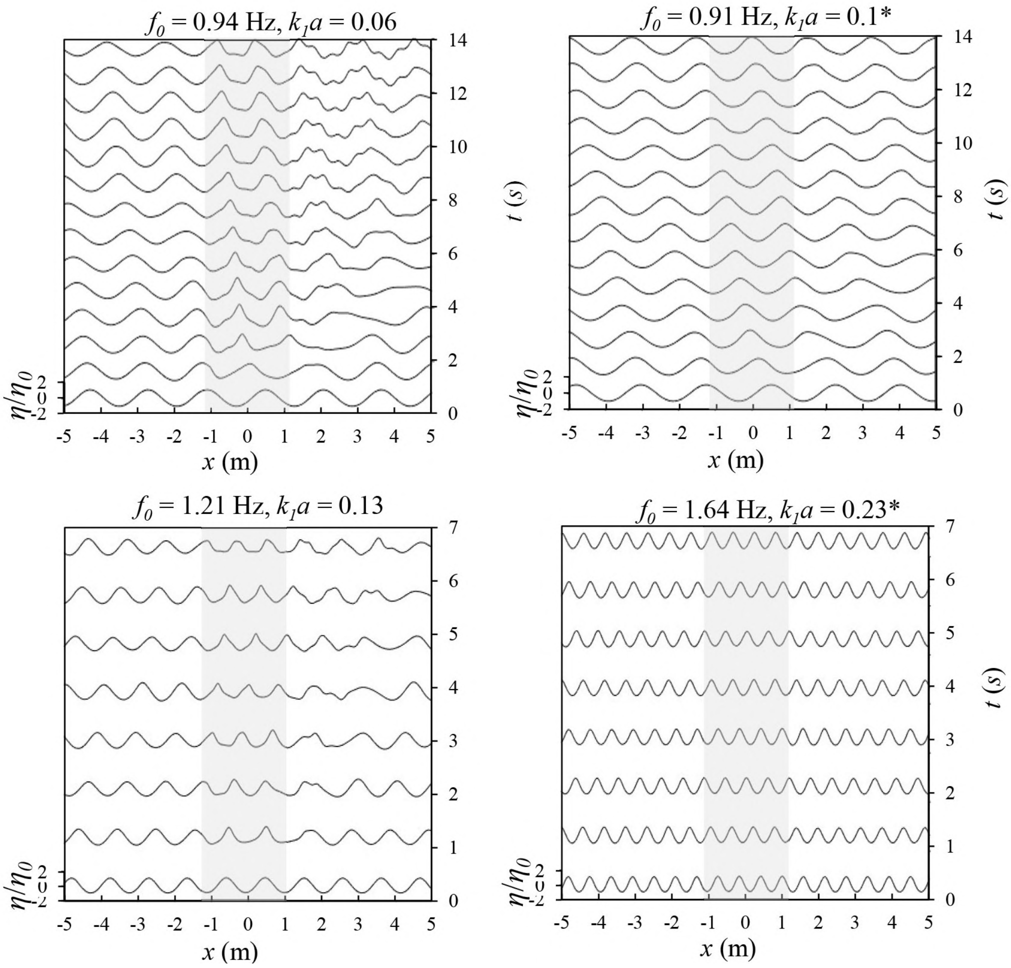

Figure 4.9: Wave evolution along the submerged step of several incident wave cases with numerical simulations (* refers to h_2/h_1 = 0.52).

due to the smaller wavelength change over the ADT. The complex wave evolution exhibits the strong effect of the small ratio of the water depths on the wavelengths, especially for the cases with long wavelengths. It results in clear nonlinear wave profiles on the shallower region and longer wavelengths at the back side of the step.

4.5.1 Wave spectrum in the spatial domain

The energy spectra (in log scale) of the surface elevations for four cases are shown in Figure 4.10, where the latter two cases refer to the case with h_2/h_1 = 0.52. Figure

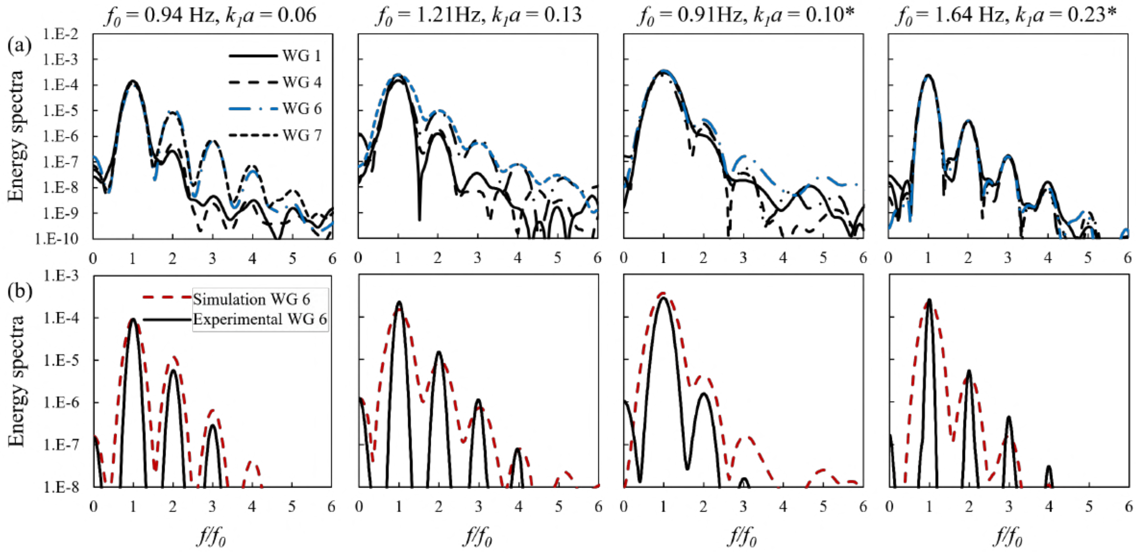

Figure 4.10: (a) Results of energy spectrum along the step and (b) comparison of experimental measurements and numerical simulation on WG 6.

4.10(a) describes the energy spectra of the numerical results at four different wave gauge positions with two before the step (WG 1 and 4) and two above the step (WG 6 and 7). In terms of the wave energy in front of the step (WG 1 and 4), it is found that the values at the first harmonic $1 \cdot f_0$ are similar and just over 1e-4. Then the energy at $2 \cdot f_0$ is about 2 orders of magnitudes smaller than that at $1 \cdot f_0$. The energy at $3 \cdot f_0$ is less than 1e-7 and that of the $4 \cdot f_0$ component is even 2 orders of magnitude smaller, which can be ignored. A great difference is found between the wave energy before and above the step in the case $h_2/h_1 = 0.36$. Specifically, the wave energy at $2 \cdot f_0$ is 1 to 2 orders higher than before the step. The maximum increase of $3 \cdot f_0$ is 3 orders of magnitude in the case $f_0 = 0.36$ Hz, $k_1 a = 0.06$. Figure 4.10(b) compares the wave energy of measurements and numerical simulations at WG 6. They show good agreement for the values at the harmonic frequencies. Here the harmonic analysis shows that the ADT effectively enhances the wave energy of superharmonics on the shallower regions (WG 6 and 7) on the step, especially for the second and third harmonics. Secondly, since there is no obvious change in the superharmonic amplitudes at the ADT (WG 4), a possible explanation for the increase of the energy near $2 \cdot f_0$ and $3 \cdot f_0$ is that the wave nonlinearity is more influenced by wave-wave interactions than by wave-structure interactions. It suggests that the wave nonlinearity is gradually enhanced rather than precisely on the abrupt depth transitions. Thus, the step length might also be a key factor for the higher harmonics in the wave elevations.

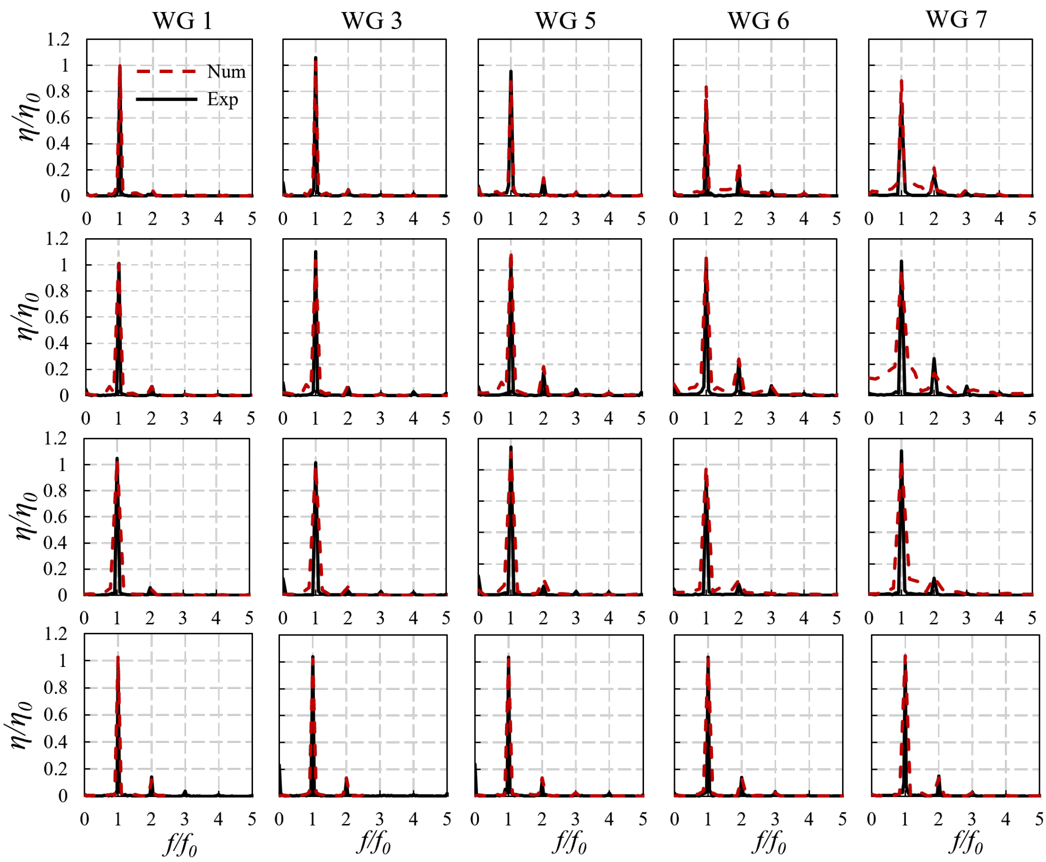

Figure 4.11: Discrete amplitude spectra of the surface elevations measured at the different gauge positions in the experiments compared to the numerical results in cases 1, 2, 5*, 6* (* refers to $h_2/h_1 = 0.52$).

The amplitude spectra of the four selected cases are analyzed and presented in

Figure 4.11. In each case, the surface elevations at five wave gauge positions are computed with the Fast Fourier Transform (FFT) to obtain the normalized amplitude spectra η/η_0, which is calculated as the ratio of the surface elevations η to the linear amplitudes η_0 propagating over the constant depth. In front of the first ADT (WG 1 and 3), it can be seen that there are mainly the first harmonics with small second components. It is likely related to the wave nonlinearity resulting from the interaction with the reflected waves. When the monochromatic waves propagate over the depth transition (WG 5, 6 and 7), it is found that the higher harmonic amplitudes (second and third) gradually increase. Besides, the second harmonic amplitude increases continually along the submerged step. These findings in all four cases demonstrate that the ADT can trigger obvious second harmonic components. A good agreement is shown between the experiments and numerical simulations, especially for the spectra near the first depth transition. Consequently, a possible explanation for enhancing the superharmonic amplitudes is an energy transfer from the first harmonic to the superharmonics induced by the abrupt depth transitions. Indeed, Mei and Unluata suggested that the energy could be transferred from the first harmonic to the higher harmonics.

4.5.2 Wave profiles of superharmonics

To illustrate the harmonics propagating over the submerged step, Figure 4.12 describes the normalized total surface elevation η/η_0 and the first to third harmonic evolution η_m/η_0 ($m = 1, 2, 3$) at four-wave gauge positions (case 1). The time windows (14 to 18 seconds) are properly chosen where the waves have passed over the submerged step but with no disturbance from the reflected waves. The separated harmonics are obtained by the FFT and inverse FFT (IFFT) of the surface elevations at each wave gauge position. No clear difference is observed on WG 1 and 5 for the first harmonic amplitude. However, the amplitudes are reduced by about 33 % on WG 6 and 7. By contrast, there is a clear increase of the second and third harmonic amplitudes on top of the submerged step (WG 5, 6 and 7) where the amount increases up to 2 to 3 times that on WG 1. The superharmonic amplitudes on WG 7 are slightly smaller than those on WG 6. This will be further discussed in Section 4.5.3. To sum up, except for the decrease of the first harmonic, the ADT effectively increases the superharmonic amplitudes on the shallower regions on the step, which is consistent with the recent study of Draycott et al. Moreover, the free-surface elevations on WG 6 and 7 with sharper crests and flatter troughs further demonstrate the strong effects of the sudden water depth transitions on wave nonlinearity.

Figure 4.13 displays the normalized surface elevations and the first three superharmonic amplitudes in space for cases f_0 = 0.94 Hz with wave steepness k_1a = 0.06 and 0.1 on water depth h_2/h_1 = 0.36. The experimental and computed results show a good agreement for the higher harmonics in both cases. The surface elevations at each position are calculated with the FFT to extract the superharmonics in space. At the same time windows are used for the elevation signals. The start points of the time windows 16.2 and 16.6 s are chosen when three to four wavelengths have passed over the first ADT. It can be found that the crest with the higher wave steepness (k_1a = 0.1) is sharper in the middle of the step. In terms of the first harmonic amplitude, it is observed that the normalized surface elevations η_1/η_0 decrease along

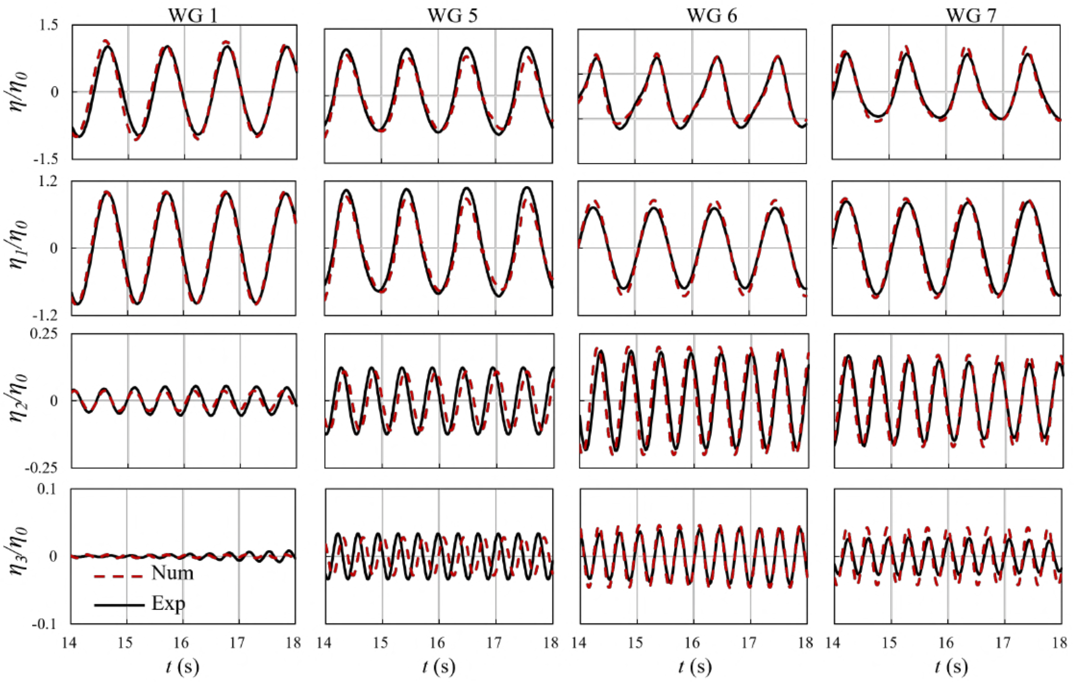

Figure 4.12: Comparison of separated harmonic time series for case 1 showing experimental and numerical results at several gauge positions.

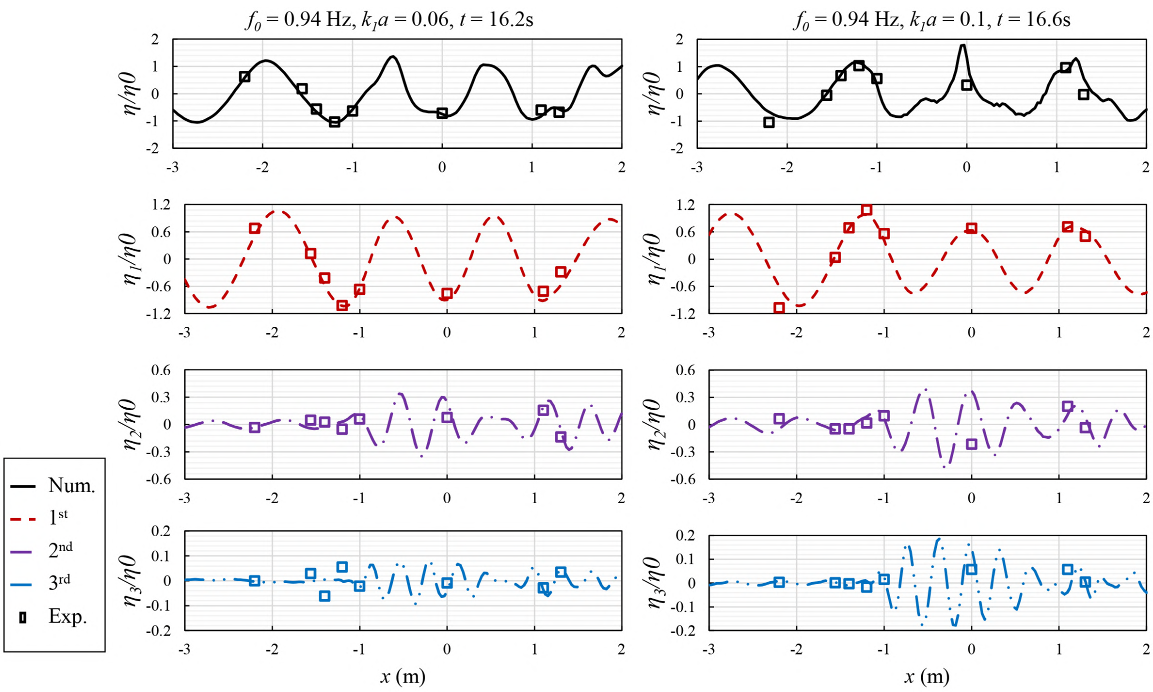

Figure 4.13: Separated harmonics from numerical simulations as a function of space and compared to experiments for two selected cases at the wave gauges.

the submerged step in both cases. The normalized amount of the crest of the first harmonic is about 1.1 times the incident wave amplitude a. However, it decreased to 0.84 after propagating over the submerged step ($x > 1.2$ m). The result is mainly attributed to the wave reflection at the first ADT, leading to a partial transmission of the waves over the step. The amplitudes of the second harmonic on the shallower regions are about 20% of that of the first terms but this amount is 2 to 3 times larger than that on the deeper side ($x = -2.2$ m). Similarly, there are relatively larger components of the third harmonic wave focusing on the shallower regions on the step. Notably, the third harmonics in front of the step is much smaller and negligible. The profiles of the second and third harmonic waves for the second case are similar to those for the first, except that the third harmonic is twice higher than the first. There is a small discrepancy in the measured and simulated results in the second case at x = 0 on the step attributed to the disagreement at the second harmonic. The overall agreement between the experiments and the numerical results is excellent.

4.5.3 Spatial distribution of superharmonics

The normalized amplitudes of the first to fourth harmonics in the spatial domain are presented in Figure 4.14 for six selected cases. The $y-$axis refers to the ratio of harmonic amplitude to the incident wave amplitude; the $x-$axis is the spatial range where the location of the step is from -1.2 m to 1.2 m (see the shaded area). The experimental results agree with those of the numerical simulations. For the cases of the water depth with h_2/h_1 = 0.36, a clear decrease of the first harmonic amplitude is found along the submerged step. For instance, the first harmonic amplitude at the second ADT (x = 1.2 m) is 0.4 smaller than that at the first ADT ($x = -1.2$ m) in case 1 with f_0 = 0.94 Hz and k_1a = 0.06. Then, the amplitude keeps decreasing and becomes only half of that at x = 2.5 m. With a larger steepness k_1a = 0.1, the first harmonic amplitude decreases at the first ADT but returns before the second ADT (at $x = 1.0$ m) and reaches $2/3$ of the incident amplitude at x = 2.5 m. The features of the first harmonic are the result of reflection by the submerged step and the interaction of the incident wave with the reflected wave. A linear model is able to capture the local variations on the step. By contrast, the second harmonic amplitudes increase in the shallower regions for all the cases with the water depth h_2/h_1 = 0.36. The fluctuations of the second harmonic are stronger than that of the first harmonic, but their amplitudes can grow up to 2 to 5 times at the front side of the step. Strong effects on the second harmonics can be observed in case 2 with f_0 = 0.94 Hz, k_1a = 0.1. For the cases with higher incident frequency (f_0 = 1.21 Hz and 1.45 Hz in Figure 4.14), the amplitudes of the second harmonic are much lower on the step since the influence of the abrupt depth transitions is less significant for the waves with shorter wavelengths.

The third and fourth harmonic amplitudes have been found to have the same trend for oscillations as that of the second. For the case f_0 = 0.94 Hz, the amplitudes of the third harmonic are about 30% to 40% of that of the second harmonic and the fourth harmonic is nearly zero which can be ignored. The amplitudes of these two superharmonics grow at the first ADT and vary regularly on the shallower region. Both amplitudes return to the incident conditions after propagating over the second ADT. For the water depth h_2/h_1 = 0.52, the evolution of the superharmonics is simi-

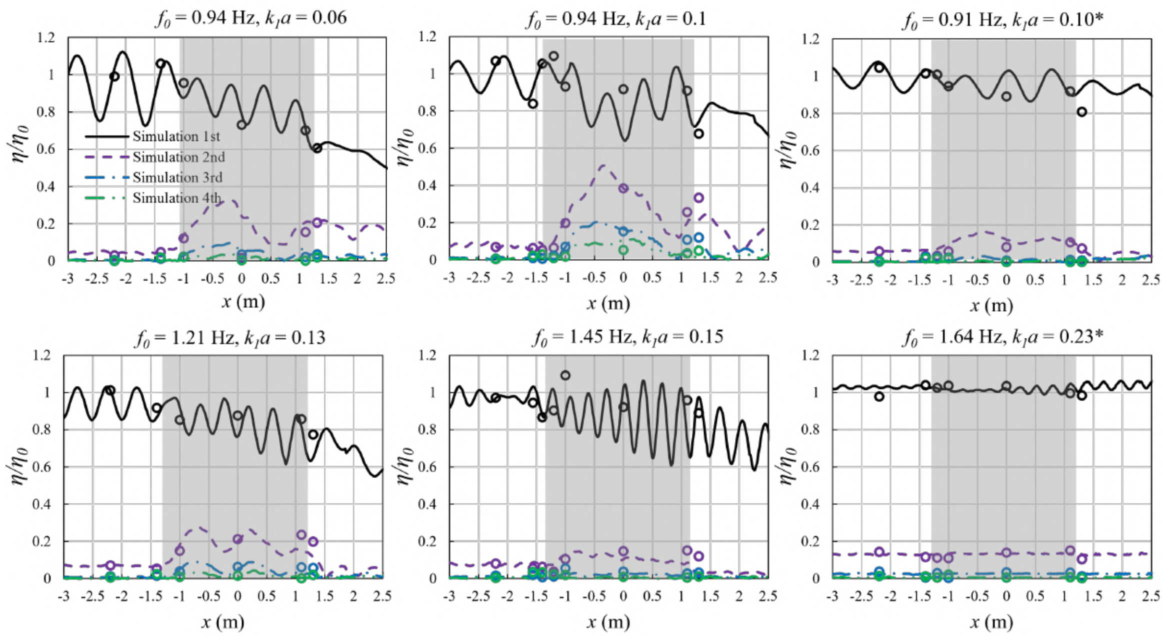

Figure 4.14: Spatial distribution of the amplitude of wave harmonics for selected cases (* refers to h_2/h_1 = 0.52). Lines: numerics; Circles: experimental data.

lar to that in the water depth $h_2/h_1 = 0.36$. Consequently, the abrupt depth transitions reduce the first harmonic amplitude resulting from the wave's partial reflection. The superharmonic amplitudes increase suddenly at the first ADT and remain high on the step, and their amplitudes decrease after the second ADT, making the superharmonics localized on the step. These results are attributed to a smaller influence of the abrupt depth transitions, leading to smaller reflection coefficients of the superharmonics, which agrees well with the findings in Christou et al.'s work. It can be concluded that the influence of the water depth ratio is dominant on the induced higher harmonics. The nonlinear effect due to the incident wave steepness in general plays a less important role in this case. It is noteworthy that the second harmonic amplitude can reach the same magnitude as that of the first harmonic (in case 2 f_0 = 0.94 Hz, k_1a = 0.1), which was also reported in the work of Draycott et al. They confirmed that the wave breaking on the top of the step was attributed to the second harmonic terms being higher than that of the first harmonic.

4.6 Nonlinear effect with varying wave parameters

To further study the nonlinear effects on the waves over a submerged step, this section presents the results of experiments and numerical simulations with varying water depth, wave frequency and wave steepness.

4.6.1 Effects of normalized water depth

Figure 4.15 displays the variation of the harmonic amplitudes for the cases with two water depth transitions h_2/h_1 = 0.36 and h_2/h_1 = 0.52 with a range of incident wave frequencies k_1h_1. The experimental and numerical results show good agreements for both the first and second harmonics at the selected wave gauge positions. Figure 4.15(a) shows the nondimensionalized amplitudes of the first and second harmonics with k_1h_1 = 1∼2 for h_2/h_1 = 0.36 and $H = 0.03$ m. It can be found that the mean amplitudes of the first harmonic are about 1 at the locations in front of the first ADT (WG 3 and 5), though the amplitude variation at WG 5 is slightly higher presumably due to the influence of reflection at the submerged step. The second harmonic components remain low for all k_1h_1 values, which is expected since the nonlinearity in the incident wave is not significant. On the step at WG 6 and WG 7, the amplitudes of the first harmonic are mostly less than 1, attributed to the reflection at the step. However, the second harmonic components become significantly larger, especially when $k_1h_1 < 1.5$. In the previous section, the higher harmonics induced by the

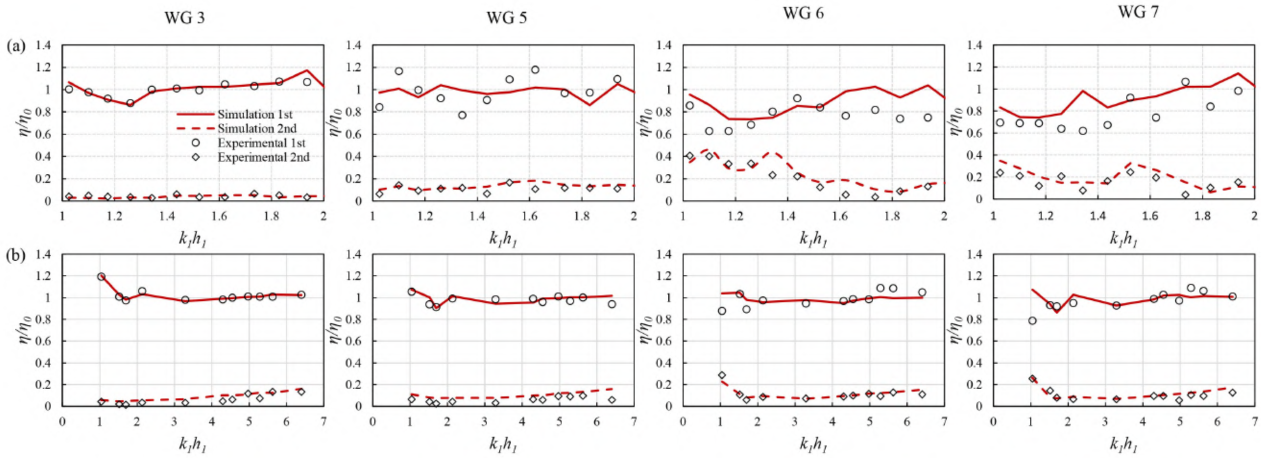

Figure 4.15: Normalized amplitudes of the first and second harmonics over the different gauge positions on two water depths with (a) $h_2/h_1 = 0.36$, $H = 0.03$ m and (b) $h_2/h_1 = 0.52$, $H = 0.04$ m.

step were shown to be triggered by the ADT for waves with longer wavelengths. For $k_1h_1 > 1.5$, the nonlinear effect at the step becomes less important hence the second harmonics reduce to less than 0.2.

In contrast, the results for the case $h_2/h_1 = 0.52$ in Figure 4.15(b) illustrate that a weaker nonlinear effect is present in deeper water depth. Note that the incident wave heights are slightly larger with $H = 0.04$ m. The variations of the first and second harmonics are small in the entire range of k_1h_1 ($k_1h_1 = 1\sim7$). Except for a small variation when the wavelength is long ($k_1h_1 < 1.5$), the first harmonic amplitudes are near 1 for all four wave gauges. The second harmonics remain low, except for small values of k_1h_1. The results with varying wave frequencies (k_1h_1) for the two water depths demonstrate again that wave dispersion dominates the nonlinear effects at the abrupt depth transitions for relatively long waves. In addition, our nonlinear numerical model shows robustness across the shallow and deep water regions.

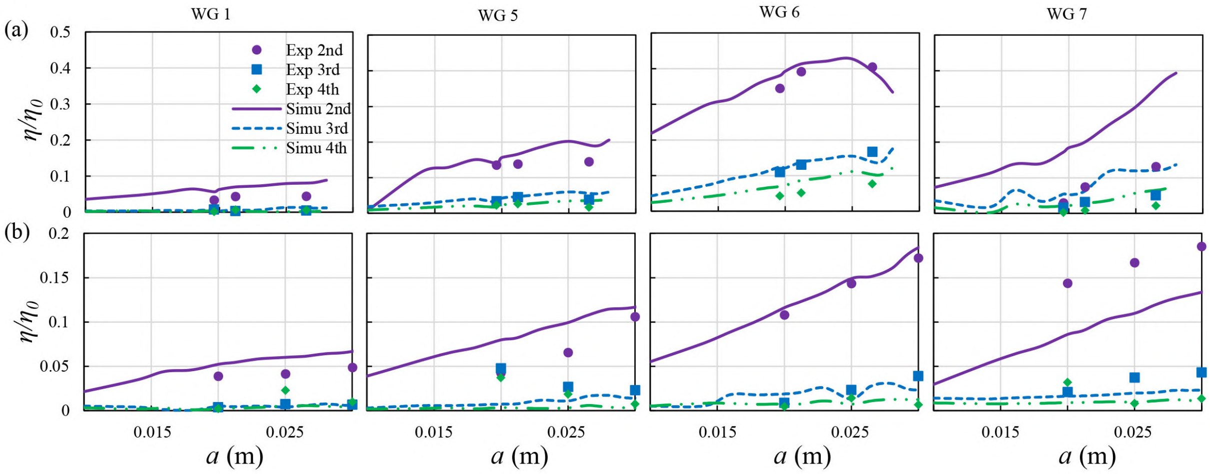

Figure 4.16: Extracted higher harmonic amplitudes at different gauge positions as a function of input amplitude $k_1 a$ comparing experiments and numerical simulations for the case $f_0 = 0.86$ Hz: (a) $h_2/h_1 = 0.36$ and (b) $h_2/h_1 = 0.52$.

4.6.2 Effects of incident wave steepness

We now examine the nonlinear effects associated with increased wave steepness. In Figure 4.16, the superharmonic amplitudes are shown with increasing $k_1 a$, ranging from 0.03 to 0.1 for $f_0 = 0.86$ Hz on the two water depths. Both measurements and numerical results are plotted. The overall agreement between the experiments and numerical simulations is acceptable. Note that the first harmonics are not shown here which are close to 1 for all the cases. It is found that generally the non-dimensional superharmonics increase with steepness at the selected wave gauge positions. The nondimensional elevations on WG 6 at the step center are mostly the highest as expected. Note that there is a slight drop in the second harmonics when the input wave steepness is larger than 0.09 in the case with $h_2/h_1 = 0.36$. There is a disagreement about the second harmonics between the experimental and the numerical results on WG 7. A possible reason is that there might be an influence of the second free waves when the nonlinearity increases (Christou et al., 2008).

For the case h_2/h_1 = 0.52, steeper waves also induce higher harmonics but with smaller amplitudes of these harmonics than that for h_2/h_1 = 0.36. The increasing incident wave steepness effectively enhances the superharmonic amplitudes along the submerged step. However, the influence is much more significant on the shallower side.

4.7 Skewness and kurtosis of nonlinear waves

The skewness and kurtosis are parameters that can be used to measure the nonlinearity of the wave profiles. In particular, the skewness measures the level of asymmetry (horizontal) of wave elevation; and the kurtosis measures the growth of the elevation peak or the sharpness–both reflect the influence of nonlinearity. For any Gaussian distribution, the skewness is 0 and the kurtosis is 3 from the properties of a normal distribution. Sea surface elevation kurtosis is often taken as an important indicator of rogue wave activity. Even when there is no definitive occurrence of extreme waves, increased skewness can indicate an increased probability of the occurrence of suddenly appearing large waves (Trulsen et al., 2020; Zhang and Benoit, 2021). This section discusses the distribution of skewness and kurtosis along the x-axis.

Skewness and kurtosis are used to describe monochromatic waves because, despite their lack of random characteristics, these parameters still reflect the asymmetry and extreme wave occurrence probability, verifying the effects of abrupt depth transitions on wave nonlinearity. For a single (monochromatic) linear wave component, the skewness and kurtosis are 0 and 1.5, respectively. The value of kurtosis of

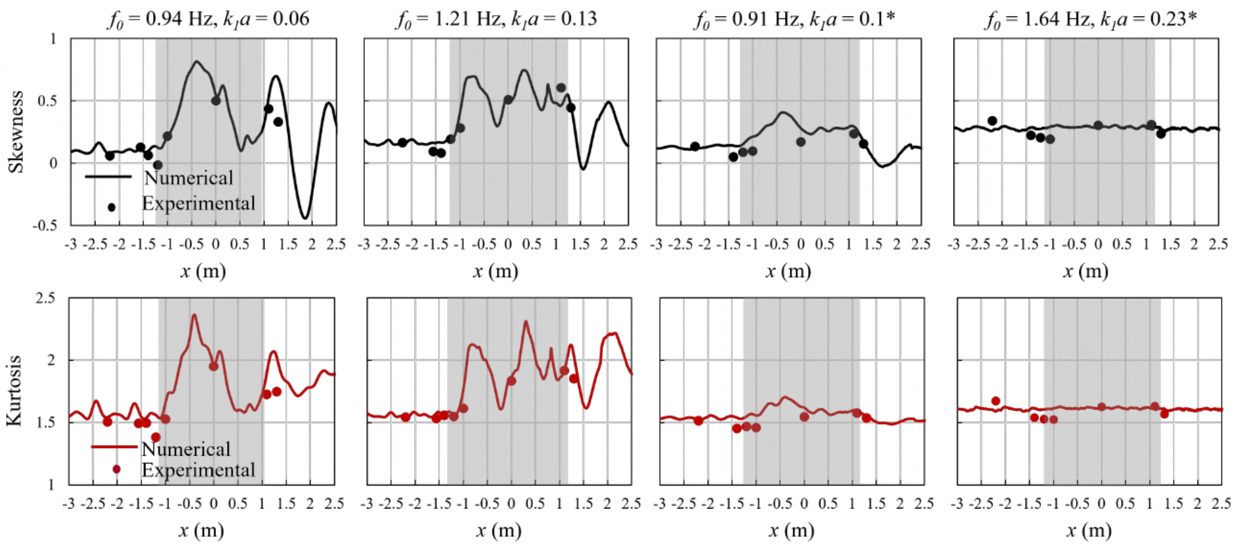

Figure 4.17: Spatial evolution of wave skewness and kurtosis in measurements and simulations (* refers to h_2/h_1 = 0.52).

regular waves is only half of that of the Gaussian random waves. It can be indeed found that the skewness is about 0.15 and kurtosis is about 1.6 for the incident wave cases. Figure 4.17 shows the evolution of the skewness and kurtosis for four selected cases in the spatial domain where the shaded area represents the submerged step. It is noticed that both the skewness and kurtosis have grown when the waves propagate through the first ADT and then reach the maxima at the top of the submerged step. The two parameters gradually decrease at the second ADT and return to the incident conditions for several cases. In terms of the skewness, a rise in values is found after the first ADT and an oscillation exists on the shallower region on the step. The oscillation suggests some distortion of the wave shape on the step. For instance in the case with $f_0 = 0.94$ Hz and $k_1 a = 0.06$, it is found that the maximum point of the skewness is located at nearly $x = -0.5$ m. Then a drop of skewness is found after the second ADT, where the value even becomes negative. This phenomenon indicates larger wave troughs are present in the deeper regions and the horizontal surface elevations remain asymmetry. The sudden increase of the skewness clearly shows the horizontal asymmetry of the surface elevation due to the presence of the submerged step. The variation of the skewness is minor for cases with a larger water depth h_2/h_1 = 0.52.

Similar trends are found for the evolution of kurtosis. The sudden increase of the kurtosis on top of the step suggests that the wave crest is sharpened. This is directly attributed to the increase of the higher harmonics, as demonstrated in Figure 4.13. The oscillation may also indicate that the higher harmonics on the step evolve at a different speed than that of the fundamental harmonics. Again, the kurtosis remains constant for the relatively deeper water. In summary, the existence of the submerged step changes the wave profiles on the step. The skewness and kurtosis suggest that the abrupt depth transitions make the shape's asymmetry more obvious and the crest sharper, a clear result of nonlinear effects.

4.8 Conclusions

The nonlinear wave propagation over a submerged step was investigated experimentally and numerically. We focus on the evolution of higher harmonics when waves pass the abrupt depth transitions. The experiment was carried out in a long wave flume with varying wave frequencies and amplitudes. Two water depths were tested. A high-speed camera was installed to capture the wave passing the first ADT, and no obvious flow separation was observed at the edge of the step, suggesting minor viscous effects. A fully nonlinear potential flow model was developed to solve the nonlinear boundary value problem. A conformal mapping method was employed to deal with the free-surface boundary conditions and the varying bottom boundaries. A mapping function was proposed to realize the transformation between the physical plane and a mathematical plane. With the aid of nonlinear simulations, it is possible for us to extract the higher harmonics (from second up to fourth) in time and space. With the abrupt depth transitions, direct comparisons of wave surface elevations at all probing locations were made between the simulations and the measurements. The agreement is excellent. The nonlinear model by the conformal mapping method was demonstrated to be suitable for simulating wave propagation over varying bathymetries including the abrupt depth transitions.

We focus on the higher harmonics triggered by the wave interaction with the abrupt depth transitions. The FFT technique is used to extract the higher harmonic components of the wave elevation. A second-harmonic reflection coefficient is defined to show the effect of the presence of the submerged step on the second harmonic waves. It is found that with increasing wave steepness, the nonlinear effect leads to increased second-harmonic reflection coefficients, as expected. Spectral analysis of the time histories of the elevations shows the importance of superharmonics, especially near the middle of the step. For the cases of relatively longer waves with $h_2/h_1 = 0.36$, the significant change of water depth at the first ADT makes the wave profile on the step distorted where the wave dispersion plays an important role. The associated higher harmonics also become considerable. With a higher $h_2/h_1 = 0.52$, both the dispersion and nonlinear effects become less significant.

The evolution of the separated harmonics along the step is investigated. This is obtained by performing FFT on the time signal of every point on the entire free surface. The sudden increase of the higher harmonics at the first ADT shows the clear interaction of the propagating wave with the submerged step. Some oscillations of the harmonic amplitudes are seen on the step. This might be due to the influence of higher harmonic free waves that can transmit to the downstream side of the step. However, for cases with higher frequency or deeper water depth, the superharmonic components return to the incident amplitudes. It demonstrates that the sudden enhancement of the ADT on the superharmonic amplitudes may be localized in the shallower regions.

The effects of the incident wave frequency $k_1 h_1$ and amplitude are studied on the first harmonics and superharmonics (second to fourth). At a lower frequency of the incident wave, we see considerable superharmonic components near the middle of the step (WG 6). Steeper incident waves generally produce larger superharmonics among which the second is the most significant.

The evolution of skewness and kurtosis is computed to evaluate the nonlinear effects at the step. For cases where there is a sudden increase of the skewness over the step, the horizontal asymmetry of the surface elevation can be found as a clear indication of nonlinearity. The similar sudden increase of the kurtosis on top of the step reflects that the wave crest is sharpened due to the increase of the higher harmonics. The asymmetry of the wave profiles and sharpened crest resulting from nonlinear effects may indicate the increase in the possibility of the occurrence of extreme waves at abrupt depth transitions. This chapter demonstrates the capability of a nonlinear numerical model to study the nonlinear wave dynamics of abrupt depth transitions. The numerical model with the conformal mapping method provides effective prediction methods for the nonlinear evolution of wave profiles and more accurate inputs for the physical problem of wave-bottom interactions. More investigations that incorporate the developed model into a multiple wave gauges assessment should be conducted in future studies.

Chapter 5

Behavior of focused wave groups on ADTs

5.1 Introduction

Up to now, the scientific explanation of the generation mechanism of extreme waves has not been confirmed. One proposed mechanism involves the enhancement of kurtosis due to abrupt depth transitions (ADTs). This theory has been substantiated to increase the probability of the occurrence of extreme waves (Salonen and Rautenbach, 2021). However, research on the interaction between focused wave groups and structures or bathymetries has not considered the influence of ADTs on the superharmonic of focused wave groups. From the perspective of the nonlinearity of focused wave group propagation, the study of the evolution of focused waves on ADTs is of considerable significance in coastal engineering.

This chapter aims to investigate the superharmonic evolution of strong nonlinear incident wave groups over abrupt depth transitions. The research employs both experiments and numerical simulations, utilizing the conformal mapping method to simulate the nonlinear evolution of waves over varying bathymetries (refer to Sections 5.2 and 5.3). The organization of this chapter is presented as follows. Section 5.4 displays the spatial distribution of wave crests and the evolution of wave spectra. A detailed analysis of superharmonics is performed in Section 5.5, considering two bathymetries with constant depth and ADTs. Section 5.6 elaborates the existence of second free waves and discusses the crests of separated second bound and free waves in the spatial domain. Then, a statistical analysis concerning exceedance probability, skewness and kurtosis is illustrated in Section 5.7. The effects of parameters of incident waves on each harmonics are also discussed. Finally, the conclusions are drawn in Section 5.8.

5.2 Experimental set-up

A series of experiments were conducted in the Hydrodynamic Laboratory at the Southern University of Science and Technology. The experiments were carried out in a wave tank with the following dimensions: 20 m long, 1.2 m deep, and 0.8 m wide, as displayed in Figure 5.1. The tank was equipped with a piston-type wavemaker and a porous absorber at the end to minimize the influence of reflected waves. A stainless steel step was positioned in the middle section of the tank, with its lee side 7.5 m away from the wavemaker. The step had a length of 2.4 m and a height of 0.24 m. For ease of observation, we place the origin of the coordinate system at the mid-section of the step (8.7 m away from the wavemaker), on the free surface

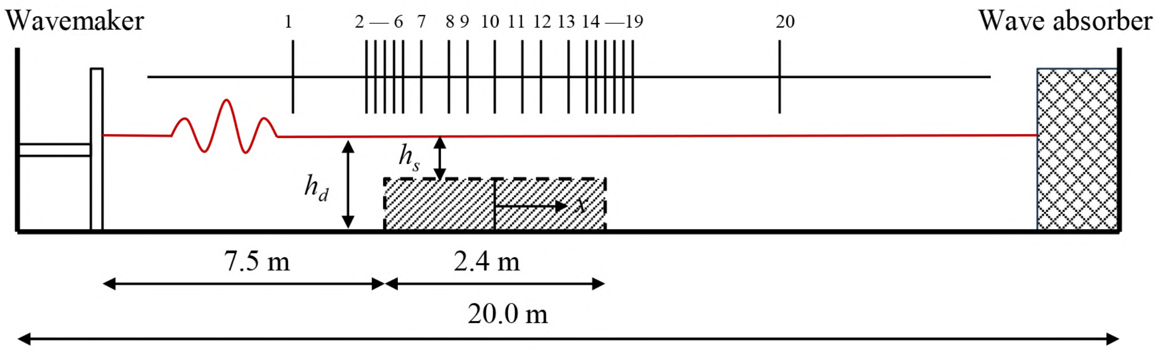

Figure 5.1: Sketch of the experimental tank with 20 wave gauges

Table 5.1: Positions of wave gauges shown in Figure 5.1.

WG No.	1	2	3	4	5	6	7	8	9	10
Position (m)	−2.2	−1.4	−1.3	−1.2	−1.1	−1.0	−0.8	−0.5	−0.3	0.0
WG No.	11	12	13	14	15	16	17	18	19	20
Position (m)	0.3	0.5	0.8	1.0	1.1	1.2	1.3	1.4	1.5	3.0

with x-axis pointing upwards. Two water depths of $h_d = 0.36$ m and $h_d = 0.48$ m are considered, achieving ratios of shallower region depth to deeper region depth of 1/3 and 1/2, respectively. The positions of 20 capacitive-type wave gauges were carefully chosen with half of them placed at the transitions and two more gauges near both ends of the tank. The positions are listed in Table 5.1 with WG 10 at the middle of the step.

The study investigates the propagation of focused wave groups over both constant water depth and varying depth conditions. Specifically, we set the linear theoretical focused position as $x_p = -1.0$ m (i.e. 7.7 m away from the resting position of the wavemaker) and the focused time at $t_p = 30$ s. Due to nonlinearity, the actual focused position and time will vary slightly depending on the wave conditions. Two

Table 5.2: Selected case parameters with a submerged step. h_d and h_s represent the water depth in deeper and shallower regions, respectively. f_p and k_p refer to the wave frequency and wavenumber for the peak frequency component. The value a is the physical crest of focused wave groups obtained from the experiments with constant water depth, which has considered the nonlinear wave-wave interaction. All cases are repeated at least three times.

No.	h_d (m)	h_s/h_d	f_p (Hz)	k_pa	k_ph_d	k_ph_s		h_d (m)	h_s/h_d	f_p (Hz)	k_pa	k_ph_d	k_ph_s
1	0.36	$1/3$	0.8	0.08	1.139	0.380	10	0.48	$1/2$	0.8	0.08	1.397	0.699
2	0.36	$1/3$	0.9	0.06	1.345	0.448	11	0.48	$1/2$	0.9	0.06	1.678	0.839
3	0.36	$1/3$	0.9	0.08	-	-	12	0.48	$1/2$	0.9	0.08	-	-
4	0.36	$1/3$	0.9	0.10	-	-	13	0.48	$1/2$	1.0	0.08	2.003	1.002
5	0.36	$1/3$	0.9	0.12	-	-	14	0.48	$1/2$	1.1	0.08	2.378	1.189
6	0.36	$1/3$	0.9	0.14	-	-							
7	0.36	$1/3$	1.0	0.08	1.578	0.526							
8	0.36	$1/3$	1.1	0.08	1.843	0.614							
9	0.36	$1/3$	1.2	0.08	2.144	0.715							

water depths are considered in the thesis work ($h_d = 0.36$ and $h_d = 0.48$m). Table 5.2 provides detailed parameters for selected cases, specifically related to water depth h_d and incident wave number k_p.

5.3 Numerical model

5.3.1 Convergence of numerical model

In the numerical model, the choice of an appropriate number of discrete Fourier points is crucial for accurate simulations. An inappropriate number of Fourier points can lead to divergence or excessively time-consuming computations. As mentioned in Section 5.2, the conditions are set with $t_p = 30$ s and $x_p = -1.0$ m, the frequency range $(0.3 - 1.8)f_p$, the middle position of step is at $x = 0.0$ m and half the length of the rectangle is 1.2 m.

To assess the convergence of our numerical model, we carry out simulations with different numbers of discrete Fourier points per peak wavelength, ranging from 20

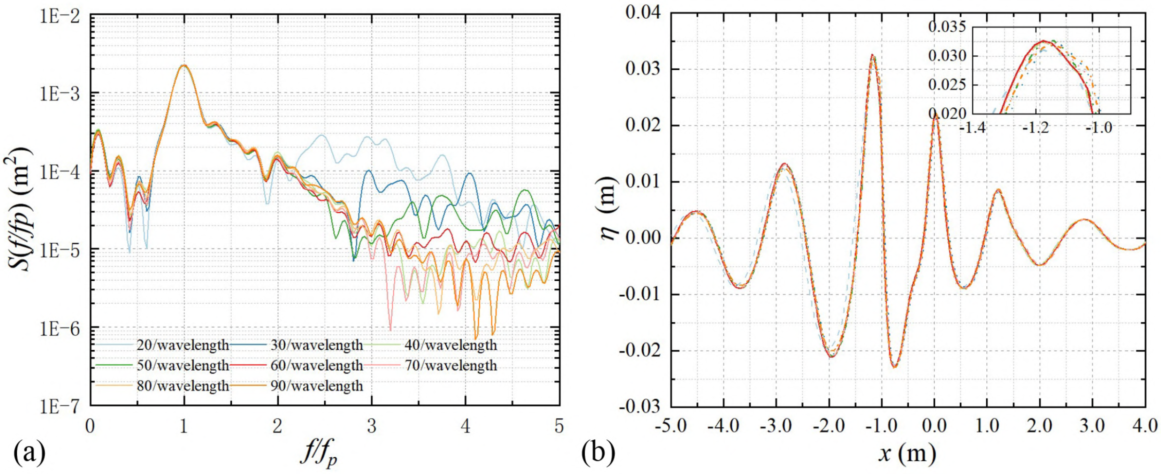

Figure 5.2: Convergence of numerical model for Case 4 with different Fourier points per wavelength: (a) wave spectra with different Fourier points per wavelength and (b) comparison of focused wave groups on ADTs with different Fourier points per wavelength.

to 90. Figure 5.2 exhibits the amplitude spectrum and surface profiles at the focused time with a submerged step for Case 4. The x-axis represents the normalized frequency. The fundamental components at $f/f_p = 1$ exhibit almost no variation. Discrepancies become pronounced when $f/f_p > 2$. The superharmonics can be reflected in the crests of wave groups, so the corresponding focused wave profiles are compared. Optimal convergence is found when using 60-70 points per wavelength; fewer than 40 or more than 70 points per wavelength result in a deviation from the peak of the wave. The settings with approximately 60 points per peak wavelength yield are found to generate consistent profiles. Consequently, we choose 60 discrete Fourier points per peak wavelength. In addition, the whole length of the numerical tank is designed to be long (60 peak wavelengths) to minimize wave reflection as well as allow the complete propagation of the longest wave component. The influence of the number of discrete Fourier points on skewness and kurtosis is analyzed, as illustrated in Figure 5.3. The results indicate that kurtosis stabilizes at a value of

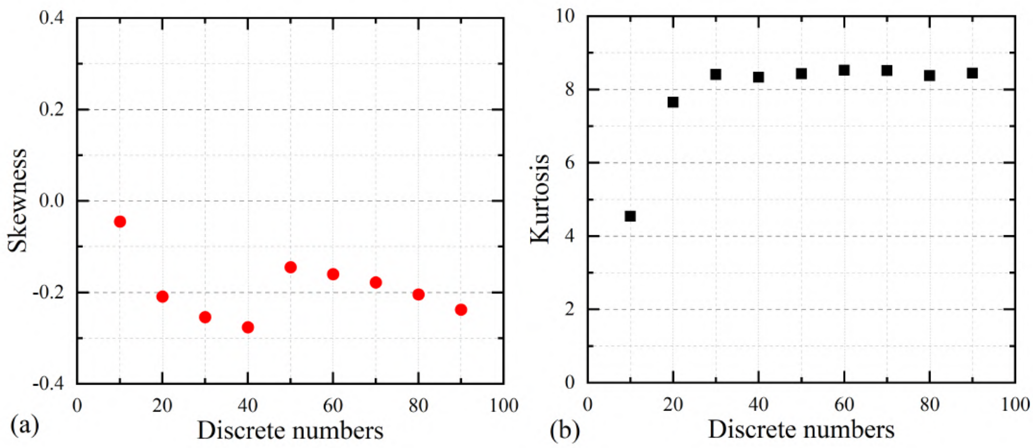

Figure 5.3: Convergence of numerical model for Case 4 with different Fourier points per wavelength: (a) distribution of skewness on ADTs with different Fourier points per wavelength and (b) distribution of kurtosis on ADTs with different Fourier points per wavelength.

8.5 when the number of discrete points exceeds 30. As the skewness of linear focused wave profiles is nearly 0, the values with different discrete Fourier points are small and vary around -0.2. From the convergence of skewness and kurtosis and the wave spectra calculated with 50-60 discrete points, the number of points higher than 30 has been enough to obtain steady numerical results.

5.3.2 Validation of numerical model

To validate the accuracy of our numerical model, we compare the measured and the simulated wave propagation for Cases 3, 9, and 12 (as shown in Figure 5.4) for the setup both with and without the submerged step. The agreement between the experimental and numerical results is excellent for all cases both with and without the submerged step. The numerical model well captures the wave characteristics during nonlinear propagation over bathymetries. For instance, at the focused time, the

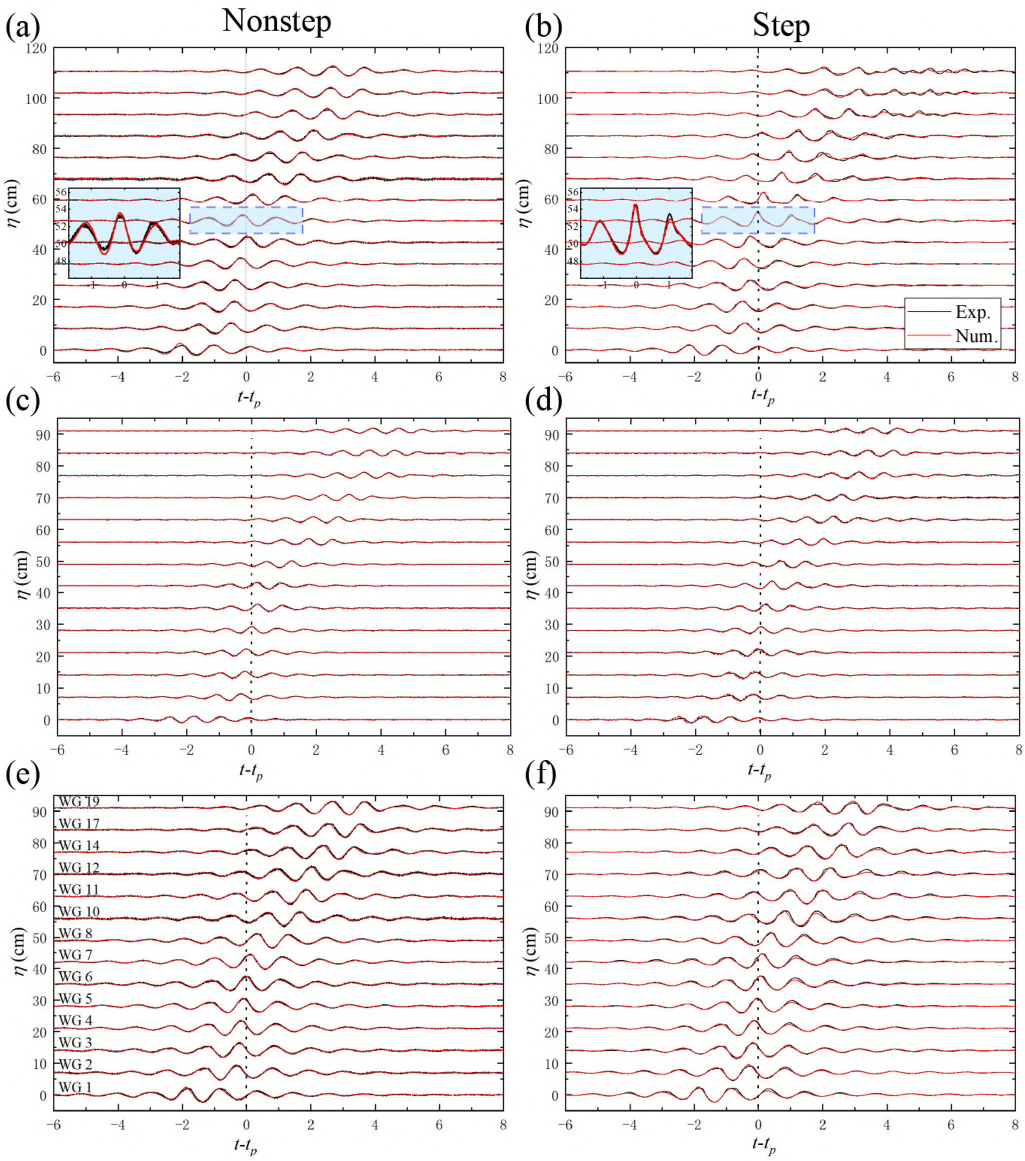

Figure 5.4: Comparison of experimental measurements and numerical results for the surface elevation at the 14 wave gauge positions along the tank: (a-b) Case 3 f_p = 0.9 Hz, $k_p a$ = 0.08; (c-d) Case 9 f_p = 1.2 Hz, $k_p a$ = 0.08 and (e-f) Case 12 f_p = 0.9 Hz, $k_p a$ = 0.08.

crests become sharper over the submerged step in Figures 5.4(a) and (b). Notably, additional minor wave groups follow the main groups, corresponding to reflected waves caused by the submerged step. Overall, the agreement across all cases, regardless of bottom type, provides confidence in our numerical model. As the strong existence of superharmonic in the nonlinear evolution of focused wave groups, further comparisons of spectra and higher harmonics are also made in the following Section 5.5.

5.4 Nonlinear wave profiles in the spatial domain

5.4.1 Crests and focused positions of wave groups

As is reported in the existing literature for a horizontal bottom (Baldock et al., 1996) the focused position and time could be shifted in strongly nonlinear wave groups due to wave-wave interactions. Here we investigate how the existence of the submerged step affects the shifting of the focused position. This section describes the focused position and crests for cases with varying wave steepnesses and peak frequencies. The spatial distribution of crests and troughs is presented to reveal the effects of ADTs on the wave profiles.

In the pre-test stage, the focused position and time were prescribed based on the linear theory. The focused positions for all cases were set at the same location $x = -1.0$ m (WG 6), while a range of amplitudes is established for each relative water depth $k_p h$. Figure 5.5 shows the maximum amplitudes and their corresponding positions in both non-step and step conditions with $h_d = 0.36$ m and $h_d = 0.48$ m, respectively. The incident peak frequency in both conditions is 0.9 Hz. The horizontal axes are the non-dimensional wavenumber and the wave steepness. Normally, the measured focused crests are higher than the theoretical ones, attributed to the nonlinear effects of the wave-wave interactions. Moreover, the increase in the incident amplitudes induces a downstream shift of the focused position. To maintain

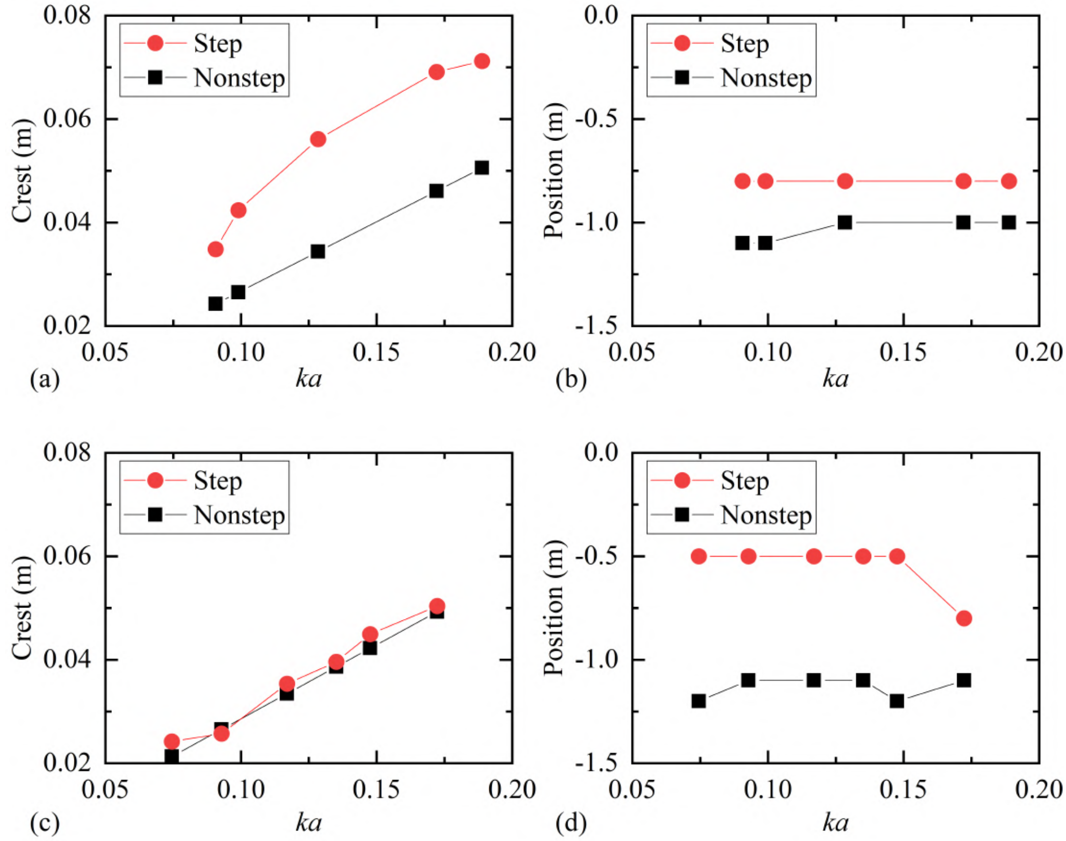

Figure 5.5: (a) Maximum elevations in the case of $h_d = 0.36$ m; (b) position of maximum elevations in the case of $h_d = 0.36$ m; (c) maximum elevations in the case of $h_d = 0.48$ m; (b) position of maximum elevations in the case of $h_d = 0.48$ m.

the focused position unchanged, the actual focused position of each case was iteratively tested in advance. The input linear focused position was set at an upstream location if the actual focused position was observed to deviate from the prescribed position. Consequently, the focused positions for all cases with nonstep conditions are designed approximately at $x = -1.1$ m, as seen in Figure 5.5(b) and (d).

In Figure 5.5(a) and (c), the cases with the submerged step show higher wave crests when compared with the non-step cases. For instance, the peak elevations for $k_pa = 0.08$ increase from 0.024 to 0.035 m, and for $k_pa = 0.14$ the value changes from 0.04609 to 0.0691 m (in Figure 5.5(a)). Meanwhile, there is a minor increment in the case with $h_d = 0.48$ m, where the nonlinearity is much weaker (in Figure 5.5(c)). Conversely, the corresponding position of peak elevation with $h_d = 0.48$ m (at $x = -0.5$ m) is found to be further downstream than that with $h_d = 0.36$ m (at $x = -0.8$ m) in the step conditions. The difference of focus position between nonstep and step conditions in Figure 5.5(b) is about 0.3 m, which is smaller than the difference of about 0.6 m in Figure 5.5(d). Therefore, the presence of ADTs not only enhances the crests but also makes the corresponding position move downstream. The shallower case ($h_d = 0.38$ m) exhibits a greater increase in crest results, while in the deeper case ($h_d = 0.48$ m), the focused positions shift further downstream. This indicates the presence of ADTs makes the nonlinear characteristics more pronounced, including a higher amplitude and a further-focused position.

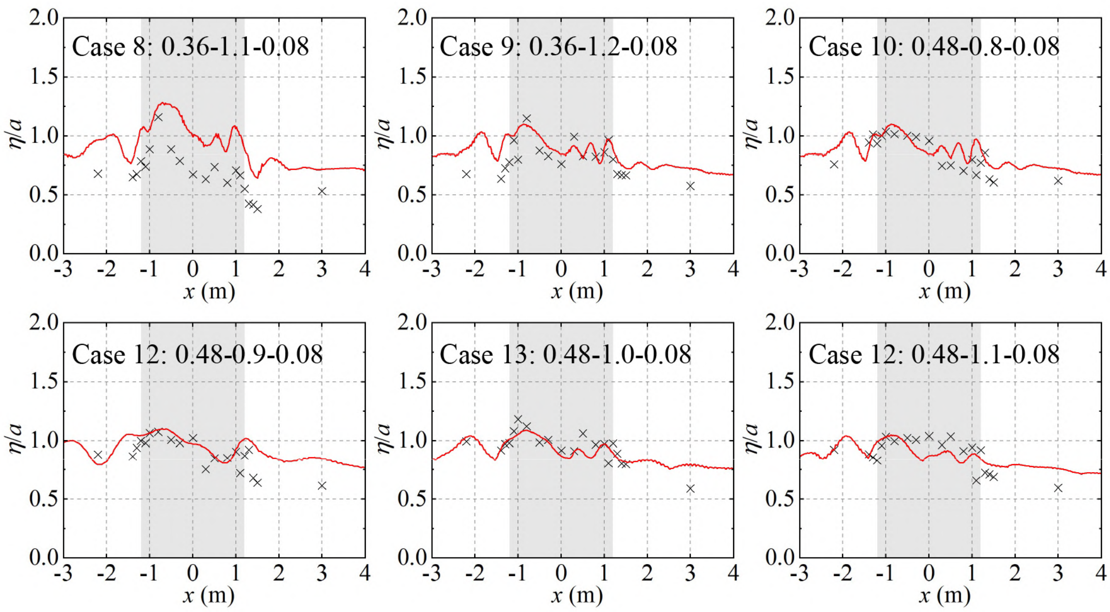

Figure 5.6: Spatial distribution of normalized crests with numerical (red line) and measured data (black crosses). The label denotes the water depth h_d, the peak frequency f_p and incident wave steepness $k_p a$, respectively.

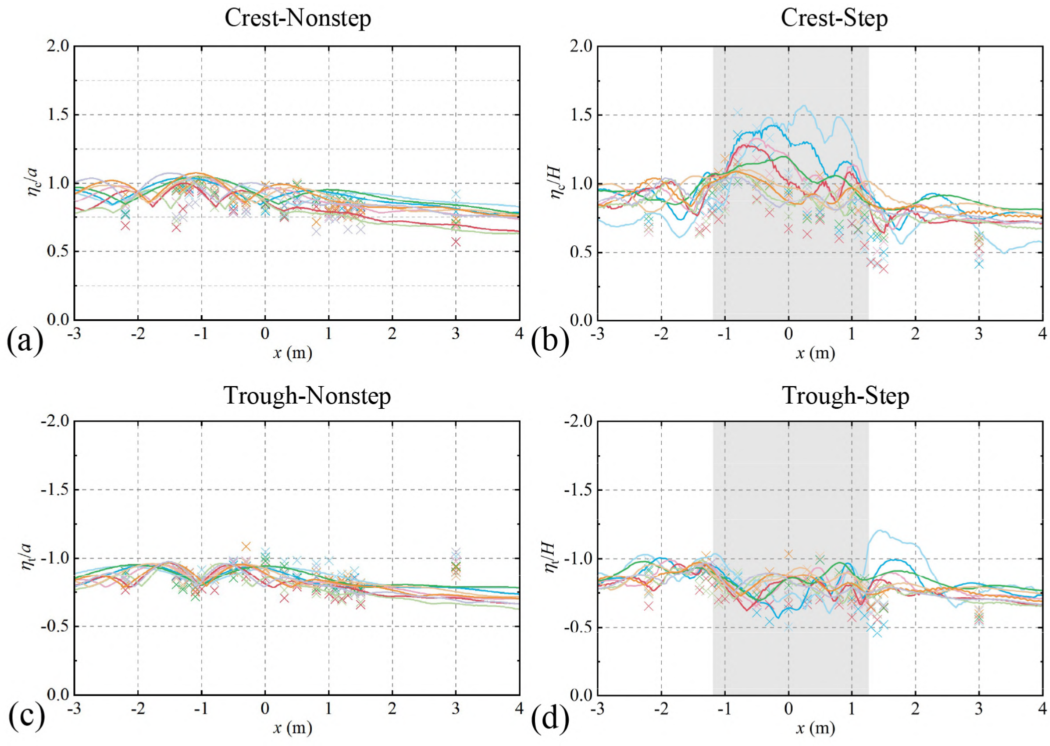

Figure 5.7: Spatial distribution of crests and troughs in both non-step and step conditions (markers: measured data, lines: computed results).

The normalized peak elevations along the tank near the step for different cases are presented in Figure 5.6 where the shaded area is the submerged step. The maximum elevations are normalized with the incident amplitude η/a for both the measured and numerical results. The label ”0.36-1.1-0.10” denotes the information of incident wave conditions, referring to water depth $h_d = 0.36$ m, the peak frequency $f_p = 1.1$ Hz and incident wave steepness $k_p a = 0.10$, respectively. This labeling is also employed in the subsequent contents. In general, good agreements between the measured and numerical results are found for the maximum elevations for all cases. A minor decrease occurs in front of the first ADT, followed by a gradual increase to the maxima at around $x = -1.0$ m. Subsequently, the crests start to decline until they reach the second ADT, during which another increase is observed (at x = 1.2

m). Finally, the crests return to constants behind the submerged step. Comparing the results of the two relative water depths of $k_p h = 0.36$ m and $k_p h = 0.48$ m shows less increment of crests over the step. This suggests the wave group interaction with the submerged step is less significant with a larger $k_p h$. A discrepancy between the numerical and experimental results is found in case 8, where the numerical results are higher than the experimental ones. This is due to strong wave nonlinearity that causes less resolution in numerical results and different generation methods of the second free waves in the numerical and experimental tanks (in Section 3.3.3).

The normalized crests and troughs are also analyzed (in Figure 5.7). The crests in non-step conditions are observed at the focused position, where the wavelengths of crests are different, resulting from the different peak frequencies of each focused wave group. The markers are the measured and the lines are our numerical results. The variation of troughs is nearly the opposite as the crests, with the position of peaks in the troughs also at $x = -1.0$ m. To further compare the variation of crests and troughs, the positive y-axis in Figure 5.7(c-d) is inverted as different to that in Figure 5.7(a-b). The forms of variation between the crests and troughs are found to be opposite in the spatial domain. When the crests increase in the shallower regions ($x = -1.2$ to $x = -0.8$ m), the troughs decrease at the same time. In addition, the absolute value of minimal troughs 0.75 is smaller than that of crests 1.15, indicating the nonlinearity of wave profiles.

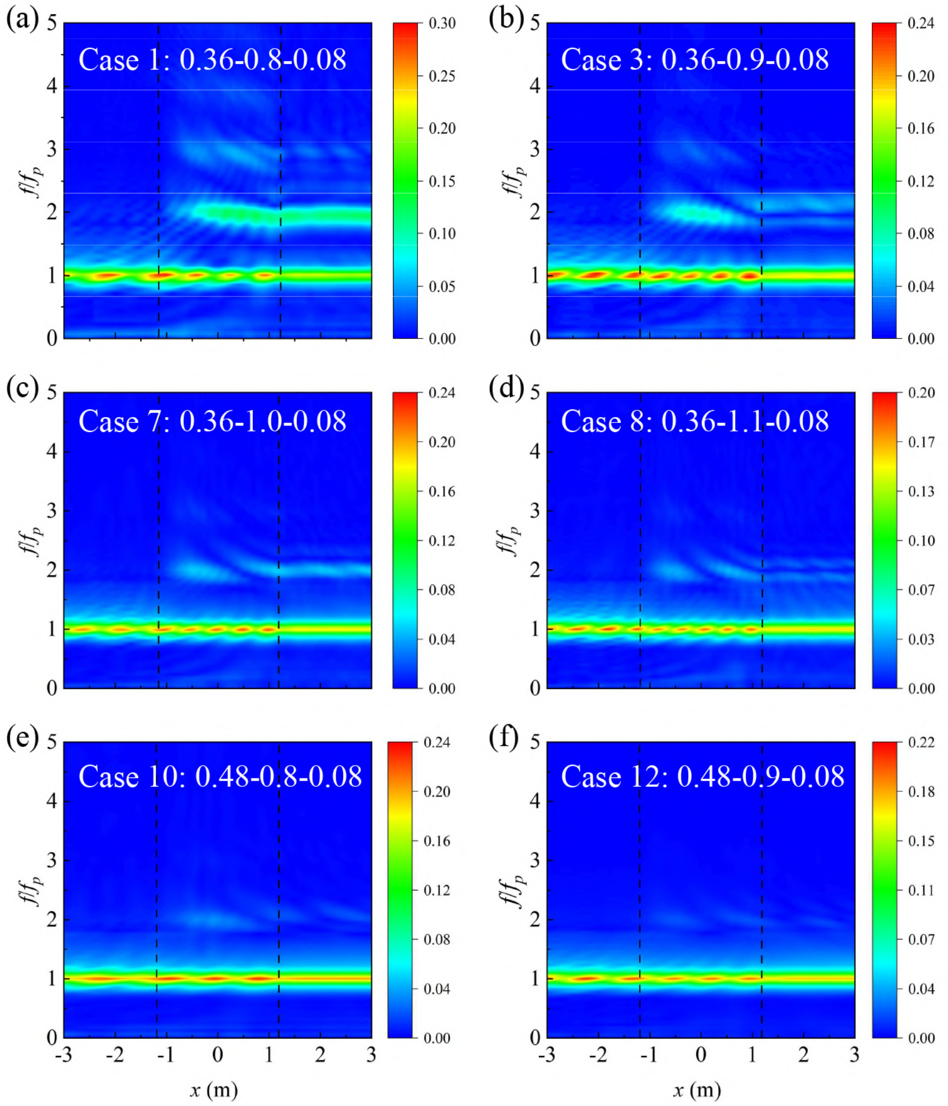

Figure 5.8: Spectral evolution of wave elevations along the submerged step with computed results.

5.4.2 Spectral evolution

The spectral evolution of the waves traveling through the step is displayed in Figure 5.8. The vertical axis is the normalized frequency and the colour represents the amplitude spectra, and the dashed lines are the edges of the submerged step. Figures 5.8(a)-(d) are for the water depth of 0.36 m and Figures 5.8(e)-(f) are for 0.48 m. The amplitudes of fundamental components are found to decrease after the first

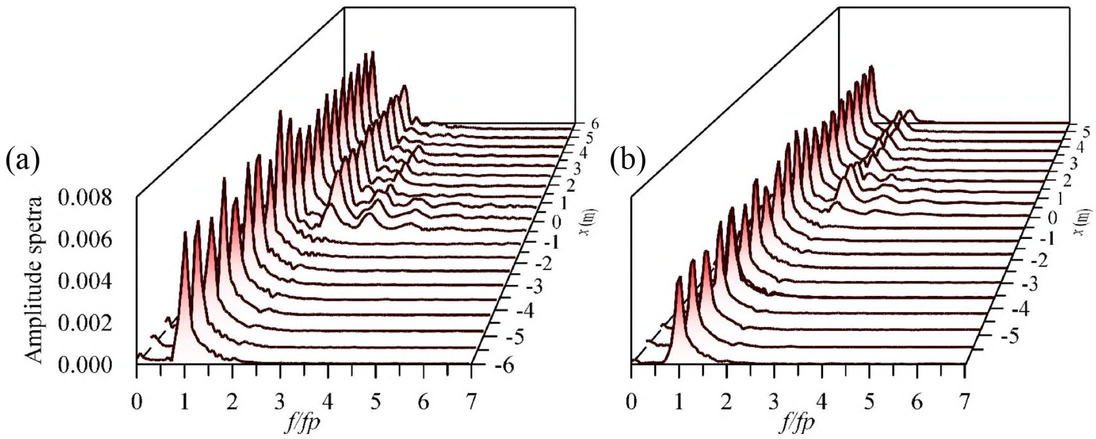

Figure 5.9: Evolution of harmonics along with the submerged step for (a) Case 1 and (b) Case 3.

ADT for all cases. Subsequently, they stabilize at approximately two-thirds of their initial values when arriving behind the submerged step. In shallower regions, second to fourth harmonics are generated behind the focused position, which can be found in Figure 5.8(a). As the relative water depth $k_p h$ increases, the nonlinearity tends to be weaker resulting in fewer superharmonics in shallower regions. For instance, in the case of $h_d = 0.48$ m (in Figure 5.8(e)-(f)), the third and fourth components become negligible. Regardless of the $k_p h$ condition, the position of the second harmonic generation remains consistent (at $x = -1.0$ m). The discrepancy is that the second component lasts longer behind the step if the condition is set with a higher nonlinearity for Case 1 0.36-0.8-0.08. With the computed results, the spectral variation for Cases 1 and 3 are displayed in Figure 5.9. It is found that the fundamental component reaches the peak at $x = -1.0$ m, followed by the generation of the second and third harmonics. Along the tank, each wave component decreases at the second depth transition (x = 1.2 m), and the third harmonics vanish approximately 2.4 m away from the second ADT.

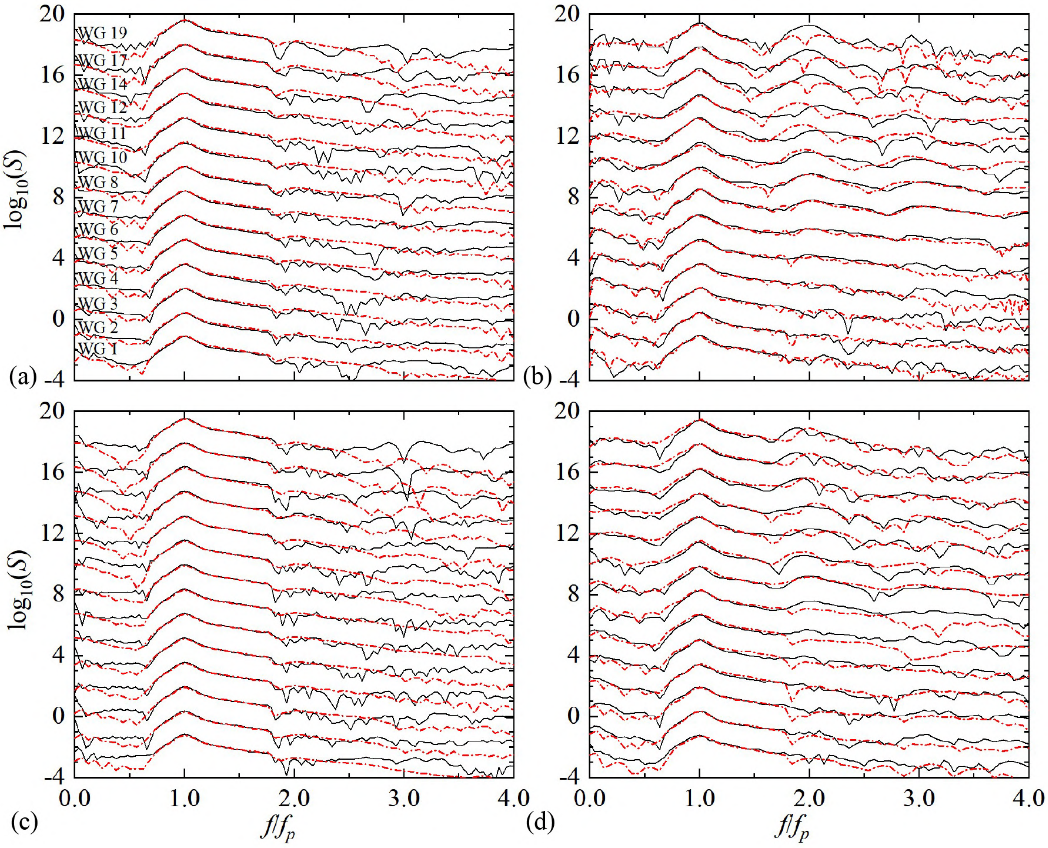

Figure 5.10: Spectral variation in space for (a) Case 3 $f_p = 0.9$ Hz without a step; (b) Case 3 $f_p = 0.9$ Hz with a submerged step; (c) Case 7 $f_p = 1.0$ Hz without a step and (d) Case 7 $f_p = 1.0$ Hz with a submerged step (black solid lines: measured data, red dot-dashed lines: computed results).

5.4.3 Spectra at specific positions

Figure 5.10 displays the specific evolution of the spectrum for Cases 3 and 7 with numerical results (red) and measured data (black). The x-axis represents the normalized frequency. The spectra of surface elevations in log-scale at the 14 wave gauges are calculated using the Fast Fourier Transform (FFT) technique. Both the non-step and step conditions are considered. For the non-step condition in Figures 5.10(a) and (c), the fundamental harmonic component, in the range of $(0.6 - 1.8)f_p$, shows very good agreements between the numerics and the experiments over the spatial domain. The superharmonics are negligible. There is a clear rise at the zero frequency, indicating a setup/setdown of the mean water level. With a submerged step in Figures 5.10(c) and 5.10(d), the superharmonics become significant as seen in the second harmonics when the group is on the step. Discrepancies in the superharmonic components between the numerical and experimental results can be found especially at the second harmonic. For instance, in Figure 5.10(d), a slight drop in the second harmonics occurs near $f/f_p = 2.3$, which shifts towards $f/f_p = 2$. The presence of the second free wave is the main reason for the discrepancy between numerical and experimental results. Section 5.5.2 presents a detailed description of the evolution of second bound and free waves.

In order to compare the higher harmonics in detail between the numerical and experimental results, spectra at the four zones are presented in Figure 5.11: in front of the first ADT ($x = -2.2$ m), the left side of the central step ($x = -1.0$ m), the right side of the central step ($x = 0.5$ m), and behind the second ADT ($x = 1.5$ m). In front of the first ADT ($x \leq -1.2$ m), there are mainly the fundamental components with a good agreement between the measured and numerical results. As the focused wave groups pass through the ADT (in Figure 5.11(b)), a clear increase in second harmonics and third components can be found. Specifically, the amplitude of the second harmonics rises from 0.03 at ($x = -2.2$ m) to 0.06 ($x = -1.0$ m), while the third component grows from 0.01 to 0.02. Along the right side of the central step at $x = 0.5$ m, a discrepancy is found in the superharmonics with numerical results showing higher values. There is a sudden drop at the second harmonic component, and it becomes more obvious behind the second ADT. Except for that, the

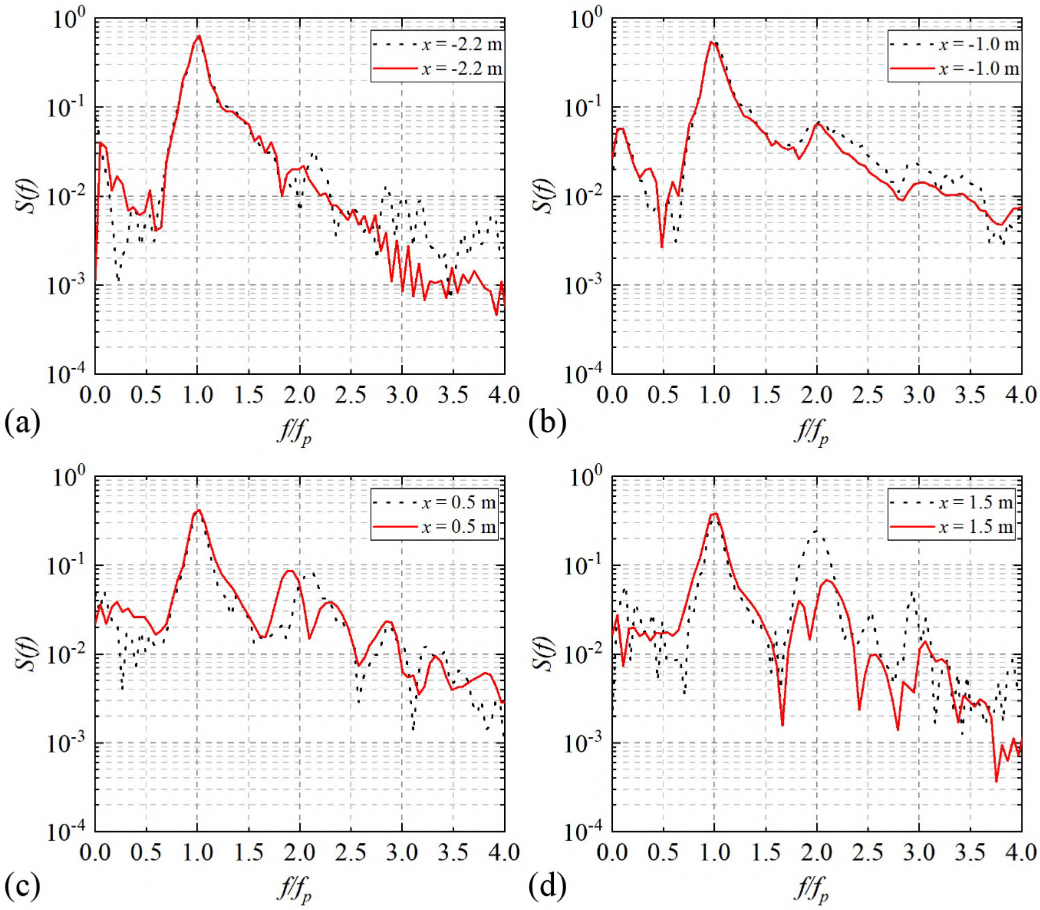

Figure 5.11: Normalized amplitude spectra at 4 different positions for Case 3 $f_p = 0.9$ Hz with measured (black dotted lines) and numerical results (red solid lines).

agreements in other harmonics are good.

5.5 Superharmonic generation of focused wave groups

5.5.1 Comparison of superharmonics in the spatial domain

A phase-manipulation approach (four-phase-based method) has been employed to extract higher harmonics in the nonlinear elevations of focused waves. This approach is particularly useful for analyzing focused wave groups where overlapping of harmonics is expected and the simple FFT is not effective. Detailed descriptions for this method are presented in Section 3.5.3 Figure 5.12 exhibits the first four harmonics extracted in the spatial domain for Case 3, which has an incident frequency range of $f/f_p = 0.3 - 1.8$. Note that the colour ranges are in different scales to present each harmonic clearly. In the first harmonic in Figure 5.12(a), small wavy variations are observed when the group propagates through the submerged step.

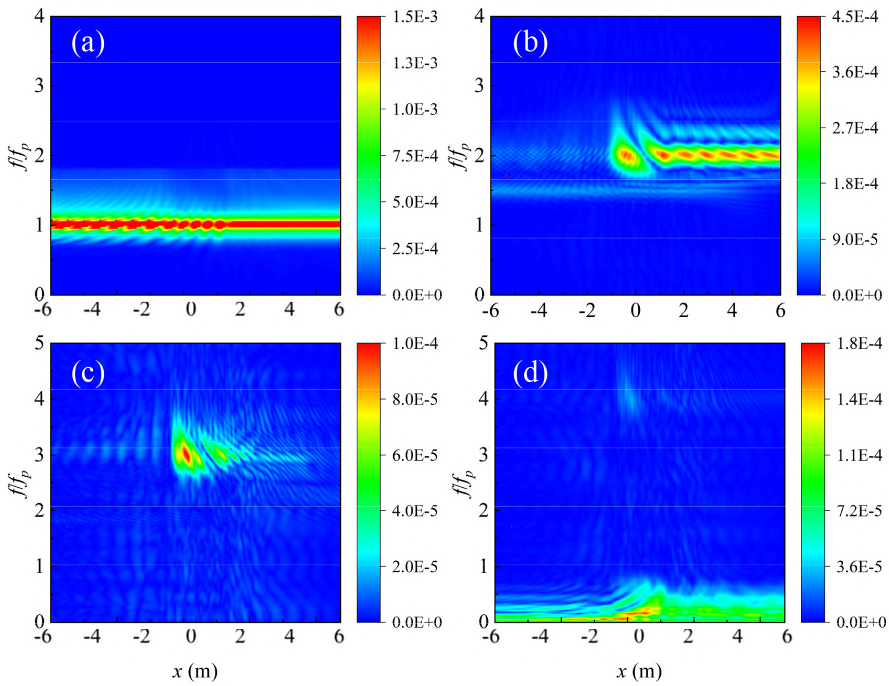

Figure 5.12: Spatial evolution of first four harmonics for Case 3.

The second harmonic is clearly induced at $x = -1.0$ m (Figure 5.12(b)) at the focused position on the step. The frequency range is approximately $(1.8 - 2.6)f_p$ and this range tends to narrow as it passes through the submerged step. Furthermore, components of the third harmonic in Figure 5.12(c) and the second subharmonic in Figure 5.12(d) can be seen, with the fourth harmonic being nearly zero. The second subharmonic signifies an elevation in the mean free surface level, suggesting that the even free surface of the focused wave groups in shallower regions is ascending. The decrease of nondimensional water depth $k_p h_s$ leads to a stronger nonlinearity, usually accompanied by more pronounced peaks and flatter troughs.

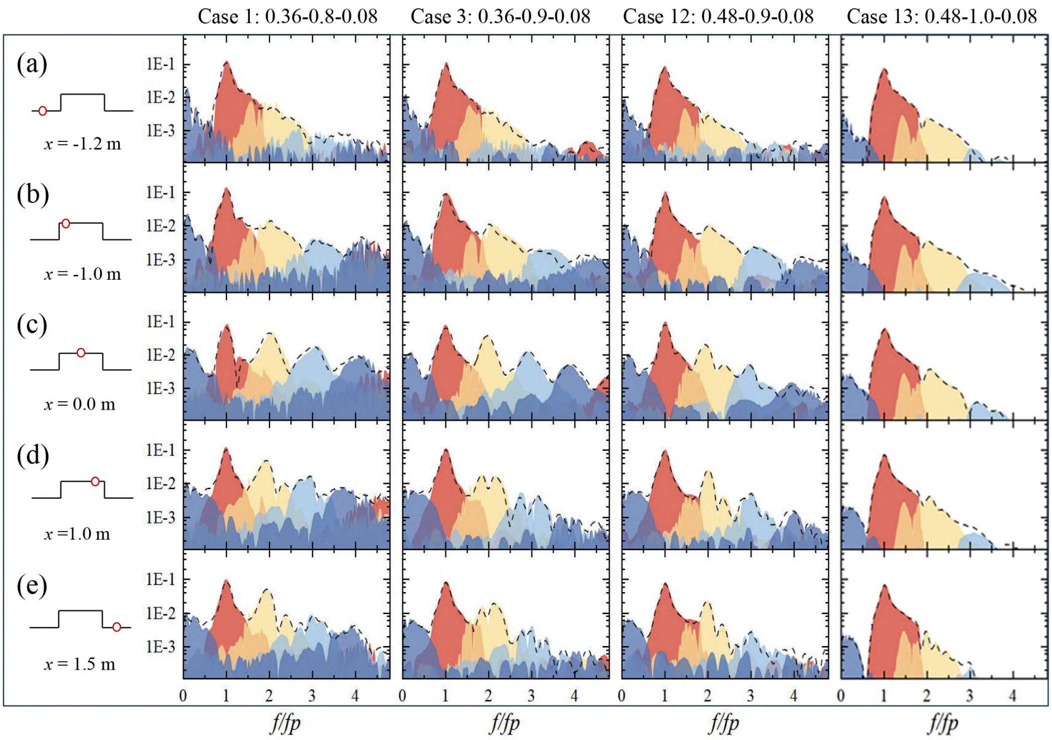

Figure 5.13: Decomposed elevation spectra for four selected cases at five positions: (a) $x = -1.2$ m; (b) $x = -1.0$ m; (c) $x = 0.0$ m; (d) $x = 1.0$ m and (e) $x = 1.5$ m.

The decomposed spectra at five different locations for four selected cases are presented in Figure 5.13, accompanied by numerical results. Each harmonic is described with colour area and the spectra of nonlinear surface elevations are shown with the black dotted lines. The surface elevations have been normalized with the crest a obtained in the constant water depth. In the step condition with $h_d = 0.36$ m, the amplitude of the first to fourth components is higher compared to the case with $h_d = 0.48$ m. The overlaps between each harmonic component make it challenging to present superharmonics directly, hence four different colours are used to demar-

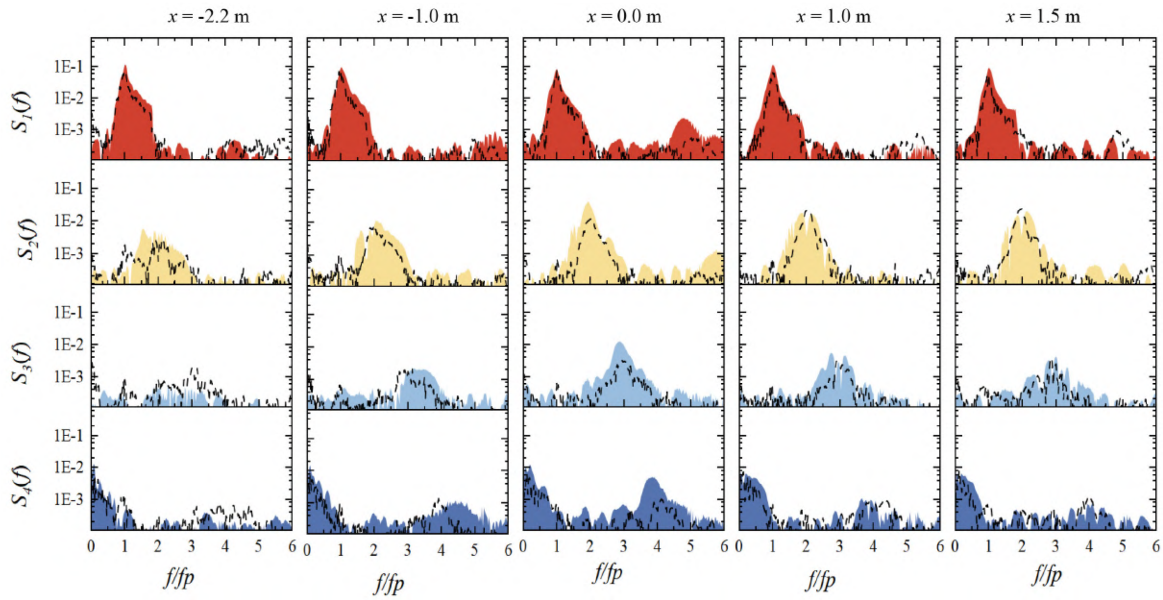

Figure 5.14: Decomposed elevation spectra for Case 3 at specific positions (black dotted lines: measured data, mapped area: computed results).

cate each harmonic. It is found that the peak of each harmonic component gradually decreases with superharmonics. The superharmonics are significantly larger with smaller $k_p h_d$ than in other cases. For example, the peak amplitude spectrum of the fundamental component for Case 3 is approximately 0.15 at $x = -1.0$ m, with the second one being 0.02. The frequency range of each harmonic then narrows at $x = 0.0$ m. Concurrently, the peak spectrum of fundamental harmonics decreases to 0.1, which is marginally higher than that with the second (0.06), the third (0.03) and the fourth (0.01) components.

From the decomposed higher harmonics, it is observed that a sudden drop only occurs in the second harmonics. This suggests that the existence of a drop is not a superposition of different harmonics but results from a component of frequency near the second ones. Taking Case 3 as an example, the spectrum of each extracted harmonic at five spatial positions is displayed in Figure 5.14. The dotted black lines represent the experimental results, while the numerical ones are depicted with colour block shadows. Good agreements between the decomposed experimental and numerical results are found for each harmonic. It is seen that the most notice-

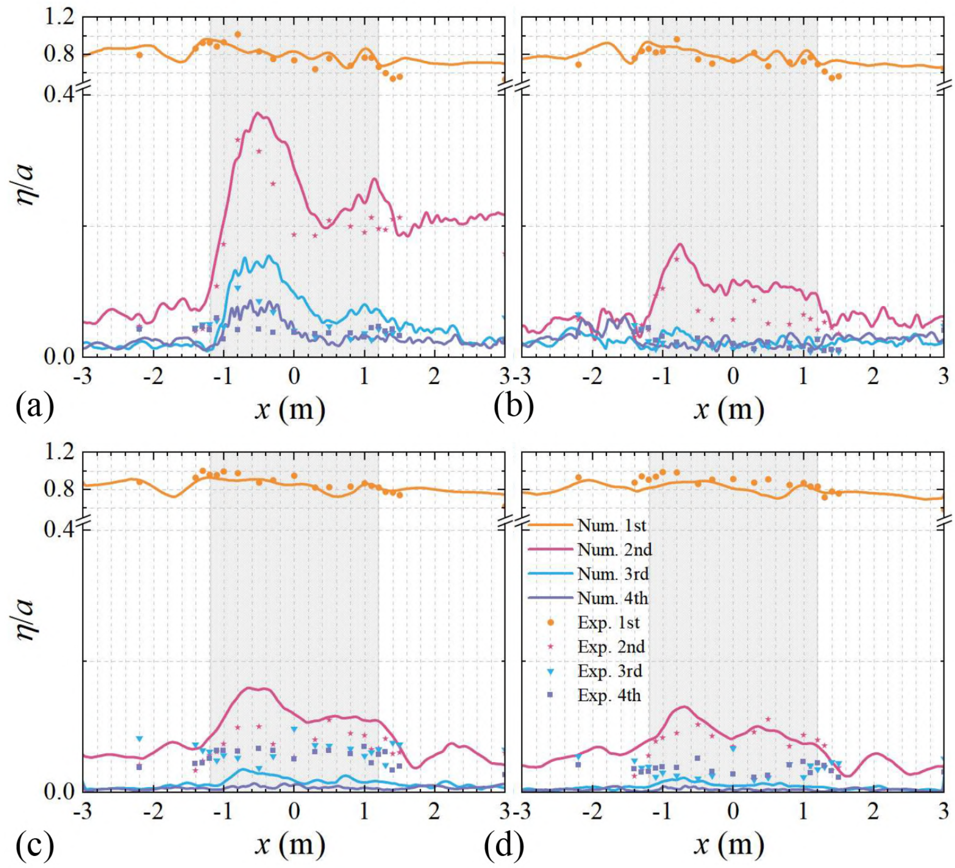

Figure 5.15: Decomposed harmonic amplitudes for four different cases with both measured and numerical results for (a) Case 7; (b) Case 9; (c) Case 12 and (d) Case 13.

able superharmonics are generated at $x = 0.0$ m, at the middle position of the step. Additionally, the subharmonics at low frequencies can also be discerned in the spectrum of S_4, whose peak spectra is larger than that of the fourth harmonic component. The cleanly extracted harmonics provide a clear description of the evolution of each harmonic component.

To capture the positions of the highest superharmonics, the peak elevations of each harmonic along the submerge step are presented in Figure 5.15. This is done by carrying out the four-phase decomposition analysis at every probing position along the tank. Both measured and numerical results for four different cases are displayed in Figure 5.15. The wave crests of fundamental harmonics $f/f_p = 1$ appear at the focused position $x = -1.2$ m and begin to decrease gradually as the group propagates downstream. Then, a sudden rise of the fundamental components can be found at the second ADT, and these second peaks are much smaller than those at the focused position. The superharmonics ($f/f_p = 2, 3, 4$) show different behaviors over the step. In terms of peak positions, the peak crests of superharmonics are at further downstream locations, specifically behind the first ADT ($x = -0.6$ m). We see the superharmonics rise rapidly after passing the first ADT. There is also a minor increase in the second harmonic at the second ADT as shown in Figure 5.15(a). The third and fourth harmonics contribute a much smaller portion in the nonlinear elevations, nevertheless, they follow a similar trend with the second harmonic component.

5.5.2 Wave profiles of superharmonics

Figure 5.16 and 5.17 present the decomposed wave profiles with both measured and numerical results. The crest of each harmonic is normalized with the wave steepness as $\eta_n/(k^{n-1}A^n)$ for all cases. In Figure 5.16, the comparison between the experimental and numerical reveals general good agreement, particularly concerning crest shapes and overall profiles. Three positions were strategically selected along the steps: the front, middle, and back of the steps, which allows us to observe the vari-

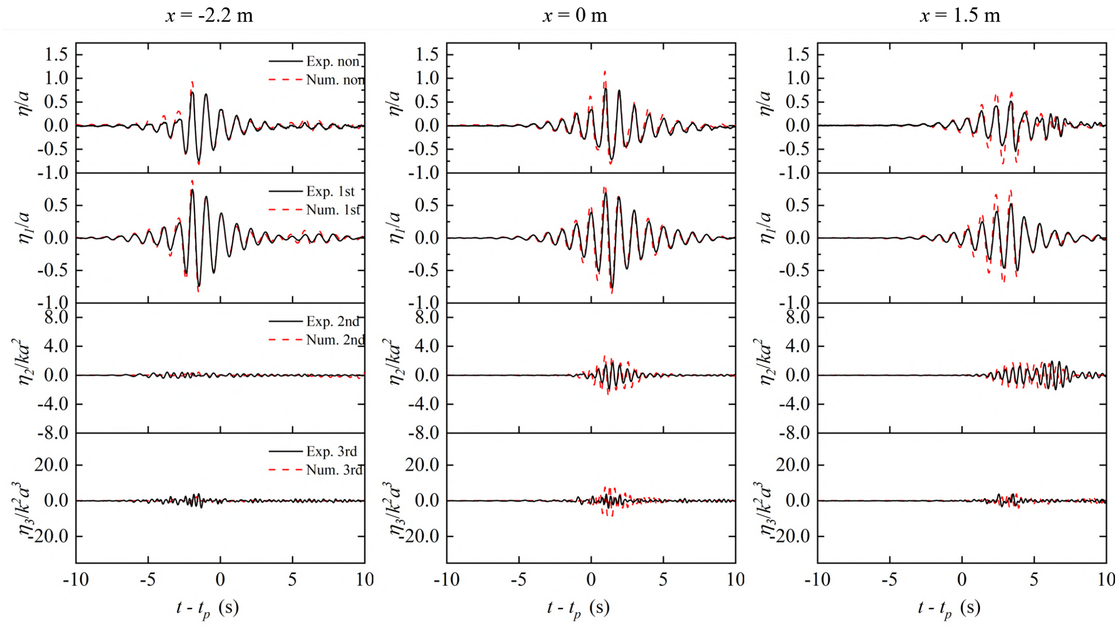

Figure 5.16: Surface elevation of decomposed harmonics at selected positions for Case 7.

ation of wave groups in space. At the position in front of the first ADT $x = -2.2$ m, the fundamental harmonic dominates, while the superharmonics remain small. The surface elevations at the middle of the step exhibit higher crests, meanwhile, the superharmonics become clearer beyond the focused time $t - t_p > 0$. Behind the second ADT $x = 1.5$ m, two wave groups of the second harmonics emerge, where the latter group corresponds to the second free wave (demonstrated in the next section). Figure 5.17 displays the nonlinear evolution of wave profiles. In the step condition, initially, the fundamental harmonics peak around the nearly focused time $t = 30.2$ s. Subsequently, the crests of fundamental components decrease gradually, but that of superharmonics increase after propagating over the first ADT. Two closed crests of second harmonics can be found over the step since $t = 32.2$ s. In addition, the length of the envelope of the second harmonics becomes longer when $t = 34.2$ s since the phase velocities are different between second bound and free waves. We

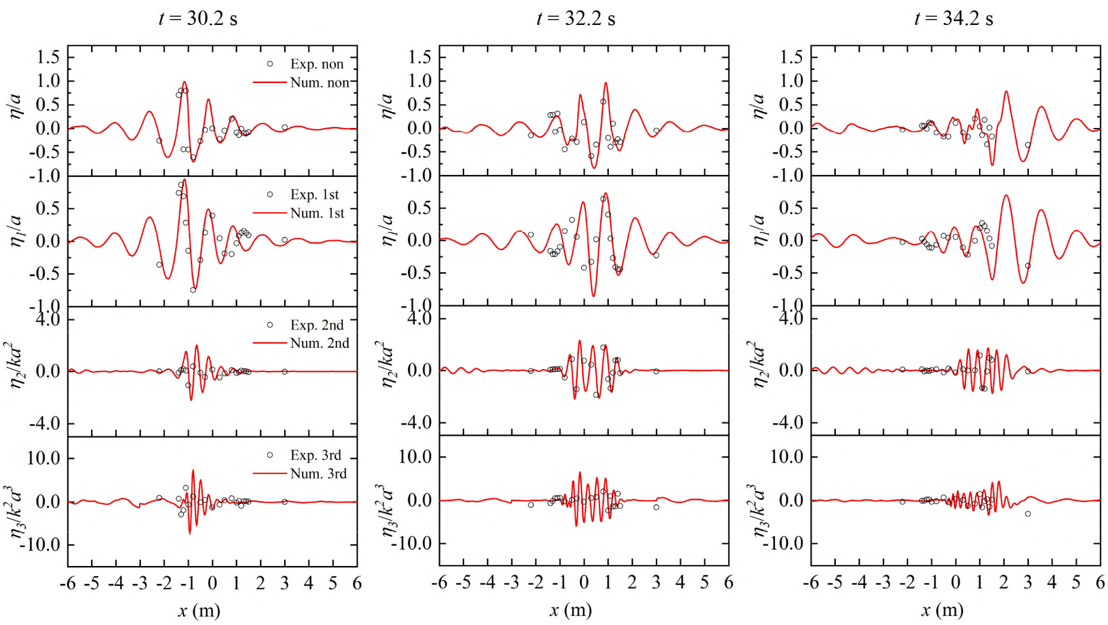

Figure 5.17: Wave profiles of decomposed harmonics at selected time instants for Case 7.

examine in detail subharmonics and superharmonics in Section 5.6.

To investigate the influence of superharmonics on nonlinear surface elevations, Figure 5.18 presents a comparison between the nonlinear numerical results and the superposition of the first three components. The wave profiles of fundamental components exhibit symmetry, and their crests are smaller than those of the nonlinear surface elevations. By incorporating the second and third components, the peaks neighbouring the crest closely resemble those of the nonlinear results. However, a discrepancy emerges between the numerical surface elevation and that obtained from the superposition of the first three harmonics. It indicates the significant role higher harmonics play at the crest, while the following and proceeding crests are predominantly attributed to lower harmonics, such as the second subharmonics.

Furthermore, Figure 5.19 displayed the generation of second harmonics and subharmonics with numerics. The process of second harmonics begins at the first ADT.

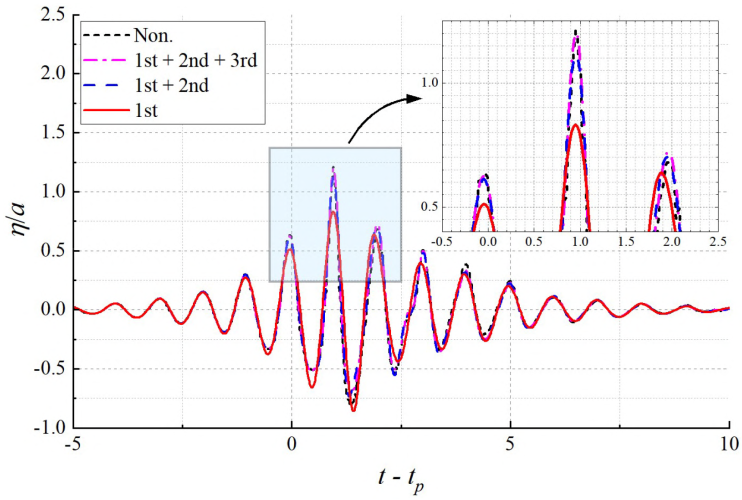

Figure 5.18: Comparison of nonlinear numeric results and superposition of first three components for Case 7.

Subsequently, the second free wave gradually separates behind the second bound waves. Additionally, there exists a component of second harmonics in reflected waves, evolving in the opposite direction. The presence of subharmonics, or a long wave, is reflected in the mean water level. They are found to be generated at the first ADT, characterized by a long wavelength. Moreover, the phase velocity associated with subharmonics is faster than that of superharmonics. Consequently, the second harmonics can be decomposed into the second bound, free, and subharmonics during the nonlinear propagation of focused wave groups. In the next Section 5.6, a further study of the second bound and free wave is presented.

5.5.3 Effects of steepness on third and fourth harmonics

Except for the second harmonics, the effects of wave steepness k_pa on the third and fourth harmonics are investigated. For the cases $f_p = 1.0$ and 1.2 Hz, the spatial distribution of amplitudes of the third and fourth components are displayed in Figure

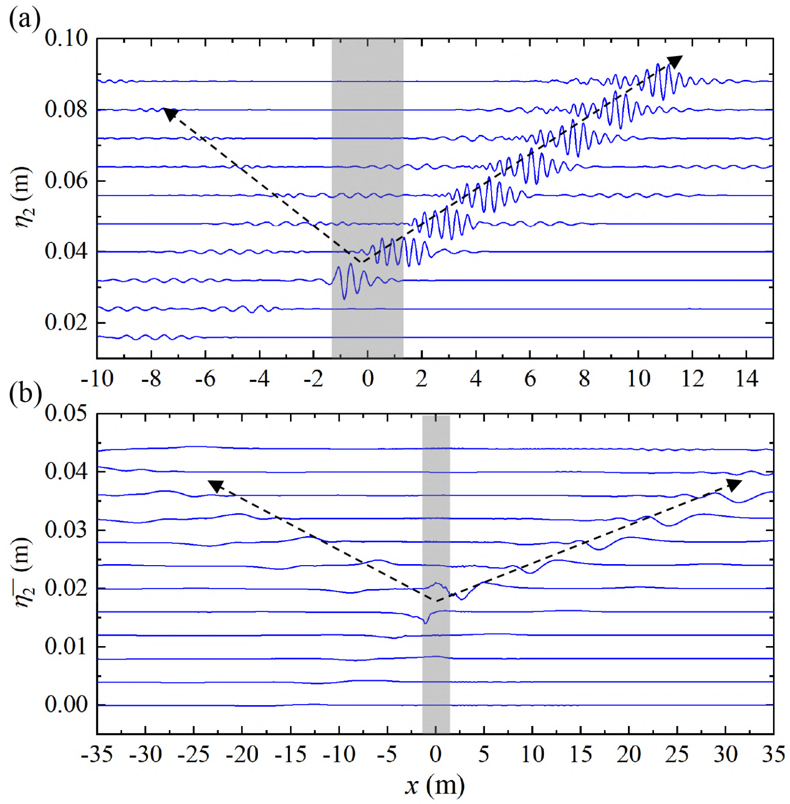

Figure 5.19: Propagation of second subharmonics and superharmonics for Case 7.

5.20. It is found that the higher steepness $k_p a$ induces larger superharmonics in shallower regions, meanwhile, the corresponding positions associated with these superharmonics shift downstream. The growth of peak values is nonlinear, specifically, for the same incremental increase in wave steepness, the peak increase becomes gradually smaller. The third and higher harmonics play important roles in shaping wave crests. While incident steepness enhances superharmonics in shallower regions, the increase in peak values occurs more gradually and appears downstream. Considering the effects of superharmonics is beneficial for accurate modelling and prediction in coastal and offshore engineering applications.

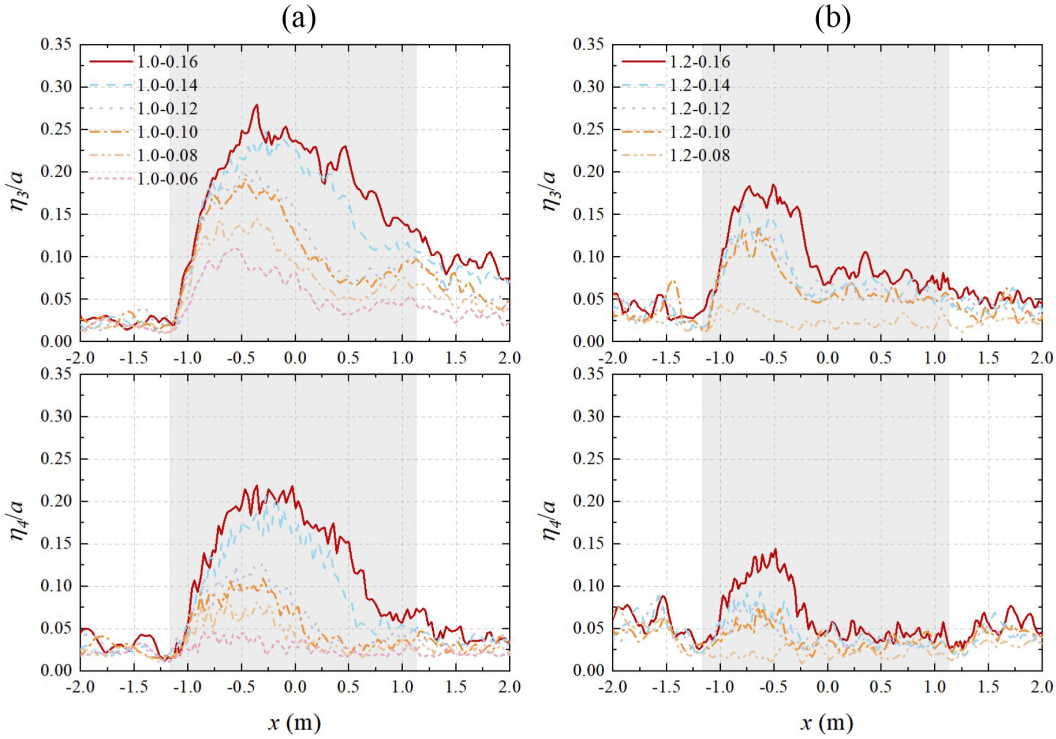

Figure 5.20: Spatial Distribution of third and fourth harmonics at (a) $f_p = 1.0$ Hz, $h_d = 0.36$ m and (b) $f_p = 1.2$ Hz, $h_d = 0.36$ m.

5.6 Analysis of second free and bound waves

5.6.1 Extraction of second free waves

To confirm that the sudden drop in the second harmonics in wave spectra is due to the existence of second free waves, we further extracted the second free waves from the second harmonic. We compare the spectral evolution of elevations without the second free component. According to the study by Gutiérrez (2017), the second free wave is significant at $k_p h_s = 0.4$ when the Ursell number is $U_r \approx 100$. The Ursell number $U_r = \frac{H}{h}(\frac{\lambda}{h})^2$ is a dimensionless parameter indicating the nonlinearity of surface waves. The conditions in our Case 3 $k_d h_s = 0.45$ and $U_r = 84$ nearly align with the conditions in Gutiérrez's work. In order to show clearly the existence of the second free waves, the spatio-temporal representation of the numerical surface elevations for Case 3 is presented in Figure 5.21. The slopes of the black dotted lines represent the phase velocities of the free waves. It distinguishes three different phase velocities, demonstrating the existence of the fundamental, second and third free waves. The measured phase velocities of the three free components are 0.99, 0.68, and 0.57 m/s respectively. Based on the dispersion relation, the theoretical phase velocities of the first three harmonics can be obtained as 0.94, 0.75, and 0.53 m/s respectively. It turns out that they match closely for each free wave. Consequently, the presence of second free waves is confirmed from the perspective of the Ursell number and phase velocities.

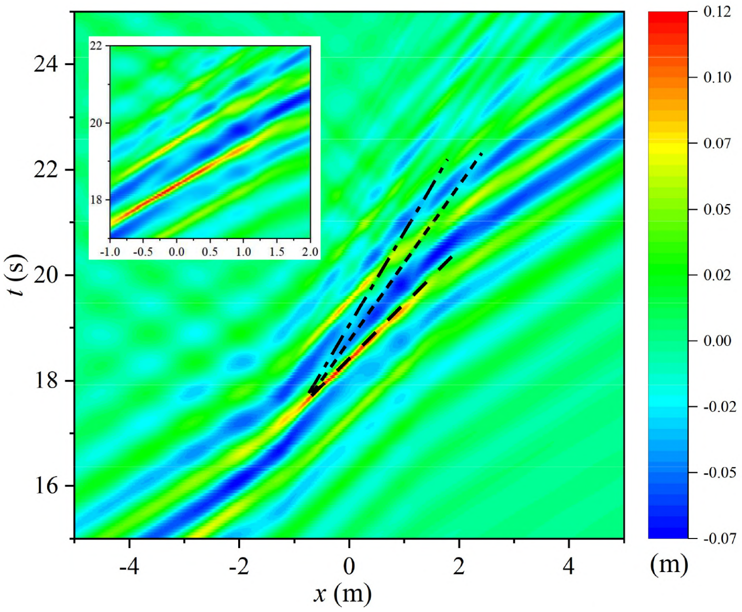

Figure 5.21: Spatio-temporal representation of focused wave groups for Case 3.

Additionally, the numerical surface elevations for Case 3 are analyzed in the spatial domain with FFT to present the spectrum distribution in wavenumbers. The wavenumbers at six time instants are shown in Figure 5.22. In the deeper region,

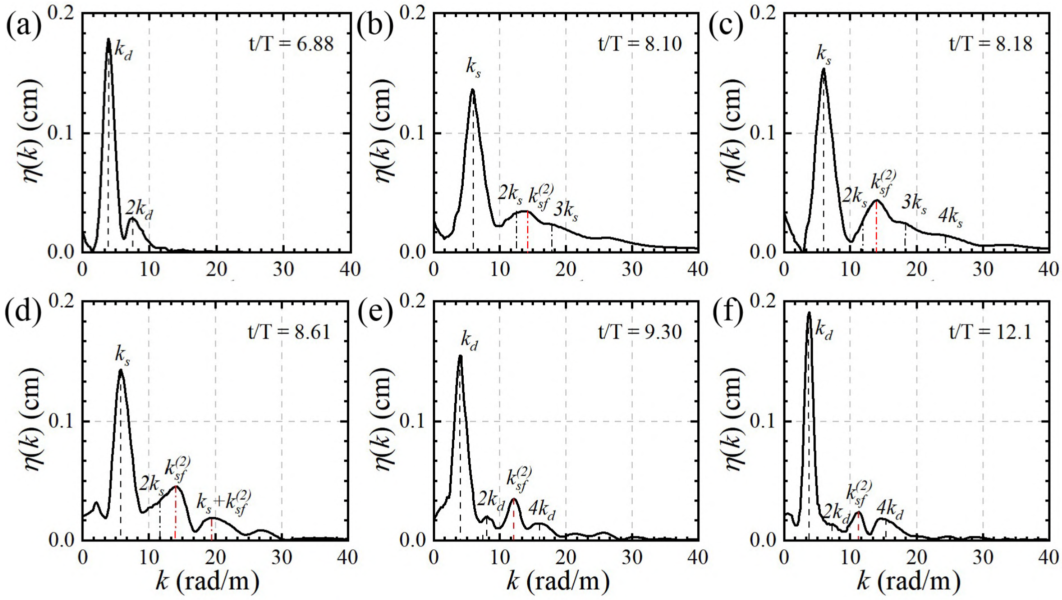

Figure 5.22: The peak amplitude of the superharmonic $\eta(k)$ for Case 3, as a function of wavenumber at six time instants (a) $t/T = 6.88$; (b) $t/T = 8.10$; (c) $t/T = 8.18$; (d) $t/T = 8.61$; (e) $t/T = 9.30$ and (f) $t/T = 12.1$.

at $t/T = 6.88$ in Figure 5.22(a), two peaks are observed where the bound wave at $k_d = 3.9$ rad/m is the primary component when the focused wave groups propagate in front of the step at $t/T = 6.88$. The symbol $2k_d$ denotes the wavenumber corresponding to the second bound wave in the region; $k_{sf}^{(2)}$ is the wavenumber of the second free waves in the shallower regions. Then, when the focused wave groups propagate over the first depth transition (at $t/T = 8.10$), an increase in wavenumber occurs ($k_s = 5.96$ rad/m) due to the change in water depth dominated by the dispersion relation (in the shallower region). The second bound at $2k_s = 11.92$ rad/m and free waves $k_{sf}^{(2)} = 13.90$ rad/m can be found over the step. The accurate wavenumber obtained by the dispersion relation for $k_{sf}^{(2)}$ confirms the existence of the second free wave. Due to the nonlinear wave-wave interaction during the focused wave evolution and wave-bathymetry interplay, there are also third $3k_s$ and fourth $4k_s$

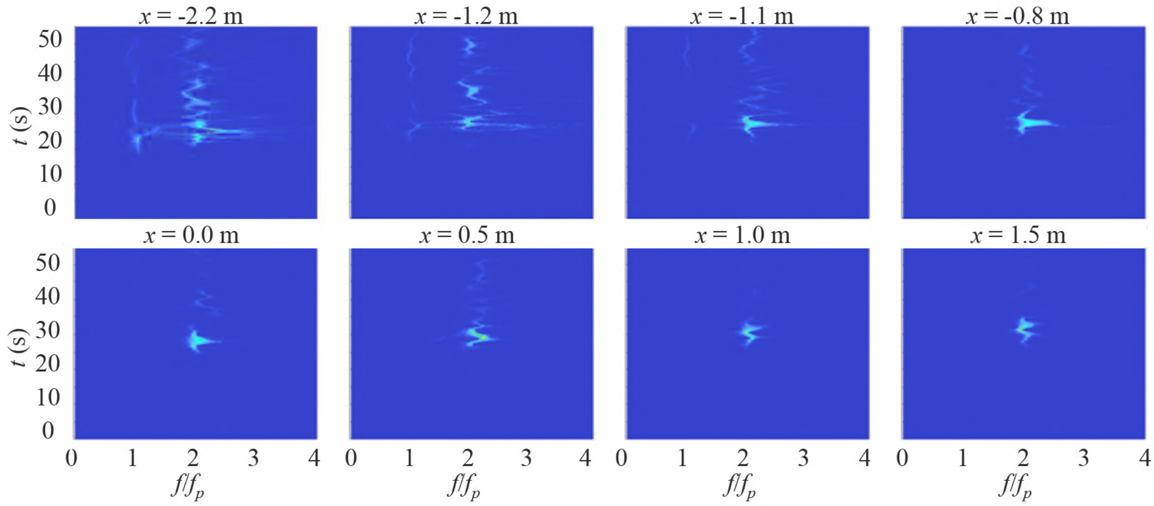

Figure 5.23: Temporal distribution of second harmonics for Case 3 for selected positions.

wave components. At $t/T = 8.61$, when wave groups propagate in the middle of the step, three maxima are visible. The first two maxima are located at wavenumbers k_s and $k_{sf}^{(2)}$ rad/m, corresponding to the fundamental and the second free waves. The third peak at $(k_s + k_{sf}^{(2)})$ rad/m corresponds to the components generated by the first and second free harmonics. It can be found that the value of free wave components tends to increase and overpass that of the bound waves at $t/T = 8.18$. This means that the influence of second free waves tends to be greater in the shallower region after passing the first depth transition. Finally, at the time instant $t/T = 9.30$, the bound waves revert back to the initial values while the wave groups have passed the two depth transitions, which are smaller than that of second free waves. This further confirms the presence of free waves in the shallower regions and their significant influence on increasing second harmonics at the second depth transitions.

Since there is an overlap in the frequency of second bound and free waves, the Continue Wavelet Transform (CWT) is employed to separate them from the temporal domain. The distribution of second harmonics is shown in Figure 5.23, where the x-axis is normalized frequency and the y-axis is the time. At WG 6 ($x = -1.0$ m), clear second components are at the focused time $t_f = 30$. The obvious second harmonic is generated due to their arrival of the focused position. Around WG 11 ($x = 0.3$ m) (passes through the central step), a separation in the second harmonics is found because of the generation of the second free wave. The discrepancy in Figure 5.10 between the numerical and measured data is also observed from WG 11, demonstrating the existence of second free waves after passing the first ADT.

Two local maximum values corresponding to bound and free components are identified at different wavelengths. Similarly, the evolution of frequencies in the temporal domain reveal two local maximum values (in Figure 5.23)–one around $t = 30.2$ s for the bound waves and the other around $t = 31.5$ s for the free waves. When analyzing the spectra individually for the bound and free waves, it is found that there are no sudden drops in the second harmonics at $f/f_p = 2$. As a result, the discrepancy in the propagation of the second free wave between experiments and numerical simulations may stem from differences in the generation method for focused wave groups. In the test wave tank, wave groups are generated by prescribing designated movement of the piston-type wavemaker. However, in the numerical wave tank, linear wave profiles on the free surface are directly prescribed as an initial condition. Furthermore, the distance between the wavemaker and the focused position is different with a much longer distance in the numerical model. Discrepancies in the nonlinear evolution distance lead to phase differences in the second free wave.

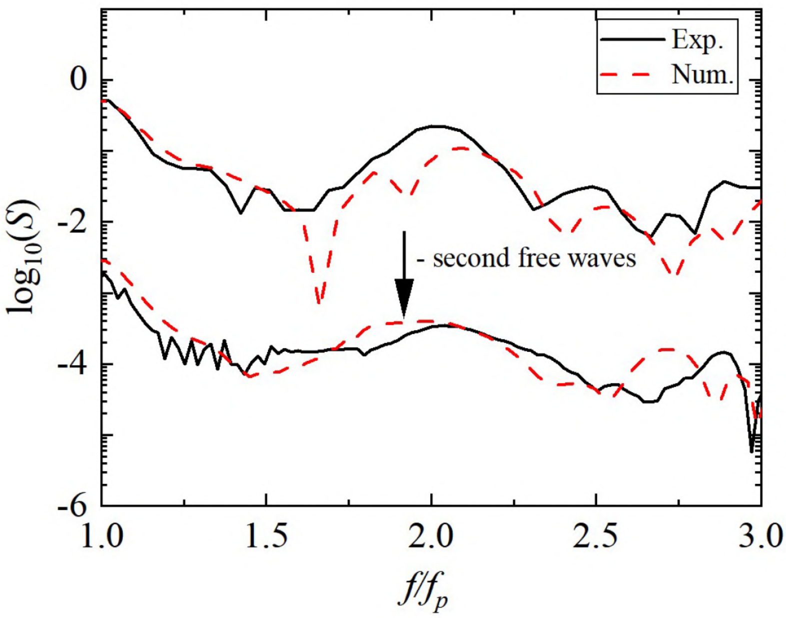

Figure 5.24: The wave spectra for Case 3 (WG 14) with and without the second free waves.

5.6.2 Evolution of second bound and free waves

The second harmonics in wave spectra with and without the second free waves are shown in Figure 5.24 for Case 3 at $x = 1.0$ m (WG 14). After removing the second free wave, the magnitude of the normalized spectra decreases. Meanwhile, a better agreement between the numerical and experimental results can be seen. It further confirms that the superposition of the second bound and free waves induces a sudden drop in the wave spectrum. Figure 5.25 presents the detailed maximum elevation of extracted second bound and free waves in the spatial domain for Cases 7 and 9. It is found that the generation of second bound waves initiates from the first ADT and peaks behind the focused position $x = -0.9$ m. Subsequently, a minor rise in the second bound wave occurs at the second ADT, with a smaller peak at $x = 1.0$ m. The peak amplitudes of the second bound waves decrease behind the step and

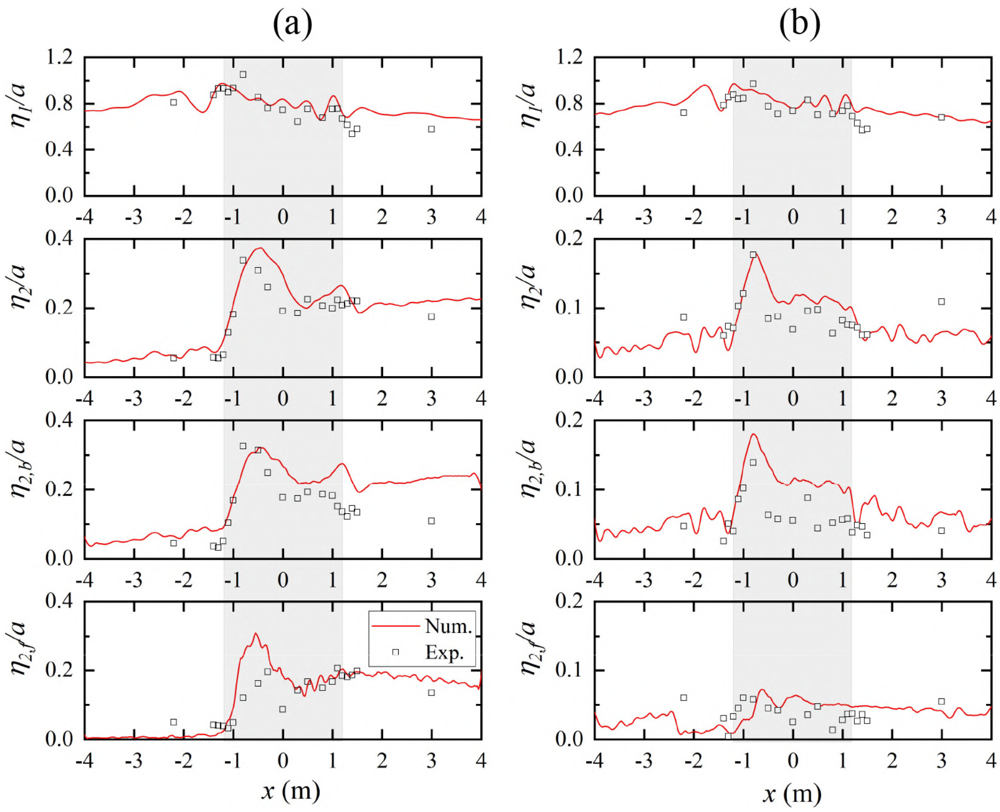

Figure 5.25: Distribution of second bound and free waves for (a) Cases 7 and (b) Case 9.

gradually stabilize. Compared to the bound waves, the position of the crests of the free wave is nearly the same but with a smaller amplitude. Additionally, there is primarily one increase in the shallower region. Unlike the sudden rise of bound waves at the second ADT, the variation of free waves is less clear. Behind the step, the peak crests of free waves surpass those of bound waves. It demonstrates that the cause of the increased second harmonics differs at two ADTs, where the free waves have a major influence at the second transition.

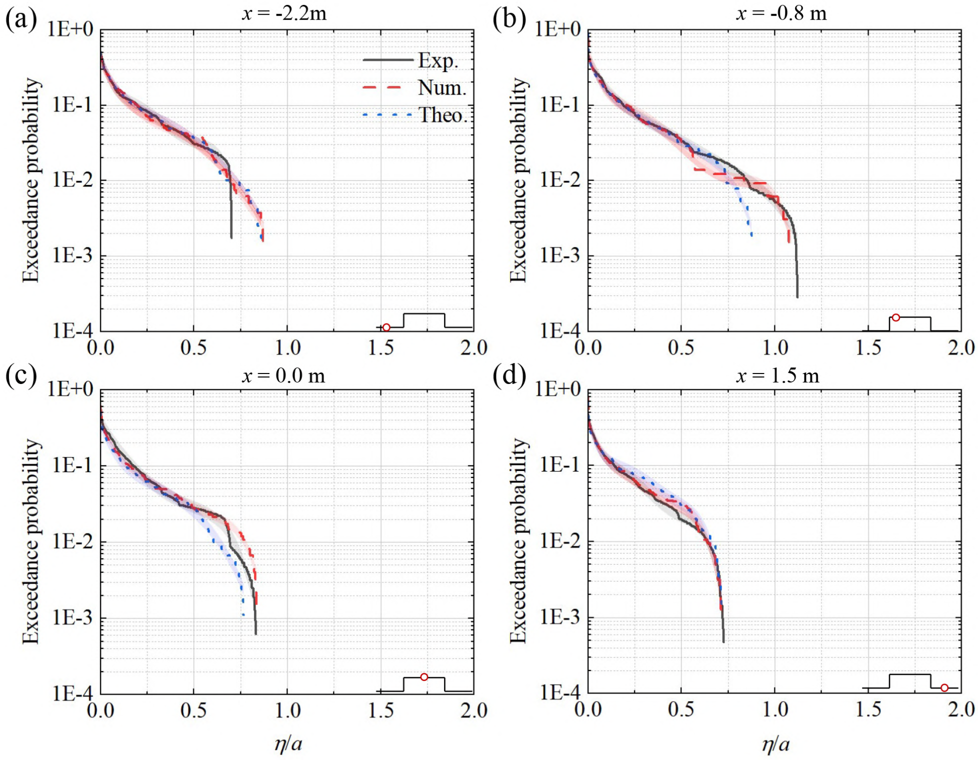

Figure 5.26: Comparison of exceedance probability with linear, numerical and measured results for Case 9.

5.7 Statistical analysis of nonlinear waves

This section studies the focused wave groups propagating over ADTs using some statistical parameters, namely, the exceedance probability as well as the skewness and kurtosis of the surface elevations. The effects of wave steepness and water depth on these parameters are discussed.

5.7.1 Exceedance probability

Exceedance probability of surface elevations can be calculated using statistical methods. To calculate the probability of exceedance of surface elevations, a time series of waves at a gauge is collected and a probability distribution function is fitted to the data. Then, the fitted distribution is utilized to calculate the probability of the elevation exceeding a certain threshold using the formula $P(X > x) = 1 - F(x)$, where $P(X > x)$ is the exceedance probability, x is the threshold elevation, and $F(x)$ is the cumulative distribution function. Here x is the normalized surface elevation η/a. The exceedance probability of surface elevations over the submerged step is shown in Figure 5.26. The x-axis is the ratio of surface elevations η to the focused wave crests a. In front of the first ADT, the linear theoretical, numerical and measured data exhibit similar behavior, with all values remaining less than 1. The maximum crest elevation η/a exceeds 1 ($\eta/a = 1.1$) at a position $x = -0.8$ m for Case 9. The linear theory result is less than 1 because the effect of nonlinearity on the crests during propagation is not taken into account. The shaded region represents the 90% confidence interval, demonstrating good agreement between the measured and numerical results. Importantly, there is a good agreement between the numerical and experimental results. Then, the maximum elevation decreases to 0.8 over the middle of the step. At the backside of the step ($x = 1.5$ m), the peak of elevation drops even further to 0.73. The existence of the step primarily improves surface elevations near the focused position. These results further reveal the enhancement of the submerged step on wave crests. Meanwhile, this could help assess the risk of extreme elevations for applications like flood risk prediction and infrastructure design.

5.7.2 Distribution of skewness and kurtosis

Two parameters, skewness λ_3 and kurtosis λ_4, of the surface elevations for three cases over the submerged step are shown in Figure 5.27. Local increases are observed at the two ADTs, with a more significant increase at the first ADT. Given the same wave steepness $k_p a$, the peaks of skewness tend to diminish for higher normalized water depths $k_p h_d$. The positive skewness values indicate higher crests and flatter troughs, mainly resulting from the decrease of water depth over the step. Moreover, the skewness quickly returns to 0 when the peaks are lower. For instance, the skewness for Case 7 is restored to 0 at $x = 3$ m, whereas for Case 9, it is at $x = 2.5$ m. Meanwhile, changes in kurtosis are more frequent in shallower regions. The peaks of kurtosis are attained at the position $x = -0.8$ m, which is close to the position where the maximum crest elevation of the second harmonic is observed. Furthermore, the variation of kurtosis is more obvious than that of skewness, as evidenced by the corresponding position $x = 4$ m for Case 9.

The spatial distribution of skewness and kurtosis in both constant water depth and step conditions are compared in Figure 5.28. It is found that the skewness remains at $\lambda_3 = 0$ over the entire spatial domain, and the kurtosis $\lambda_4 = 10$ is located at $x = -1.0$ m, which is the prescribed focused position. When a step is submerged at the bottom, increases in both skewness and kurtosis are observed at the top of the steps. Notably, the spatial locations corresponding to the maximum values have shifted downstream. Considering the spatial distribution of harmonics in Figure 5.15, the position of peak kurtosis coincides with the appearance of the superhar-

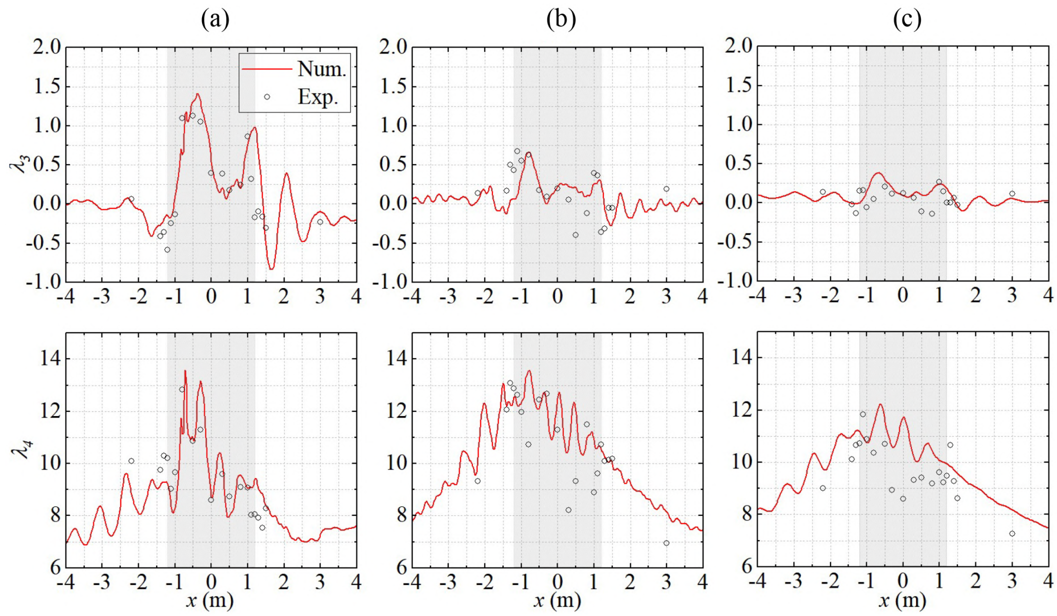

Figure 5.27: Spatial evolution of skewness and kurtosis for (a) Case 7; (b) Case 9 and (c) Case 13.

monic. Therefore, the ADTs induce the generation of superharmonics, enhancing the surface elevation asymmetry. Additionally, the numerical results compare well with the measured ones for all cases.

5.7.3 Nonlinear effect with varying wave parameters

The influence of each wave harmonic on the skewness and kurtosis is examined by analyzing the skewness and kurtosis of the superposition of different harmonics, as shown in Figure 5.29. The fundamental harmonics yield results similar to those in the constant water depth, except for a lower kurtosis peak. Then, the higher harmonics (the second to fourth bound components) are stacked together. Increased peaks of skewness and kurtosis are observed when considering higher harmonics. The distribution pattern remains the same, with only an increment of peaks in the shallower region.

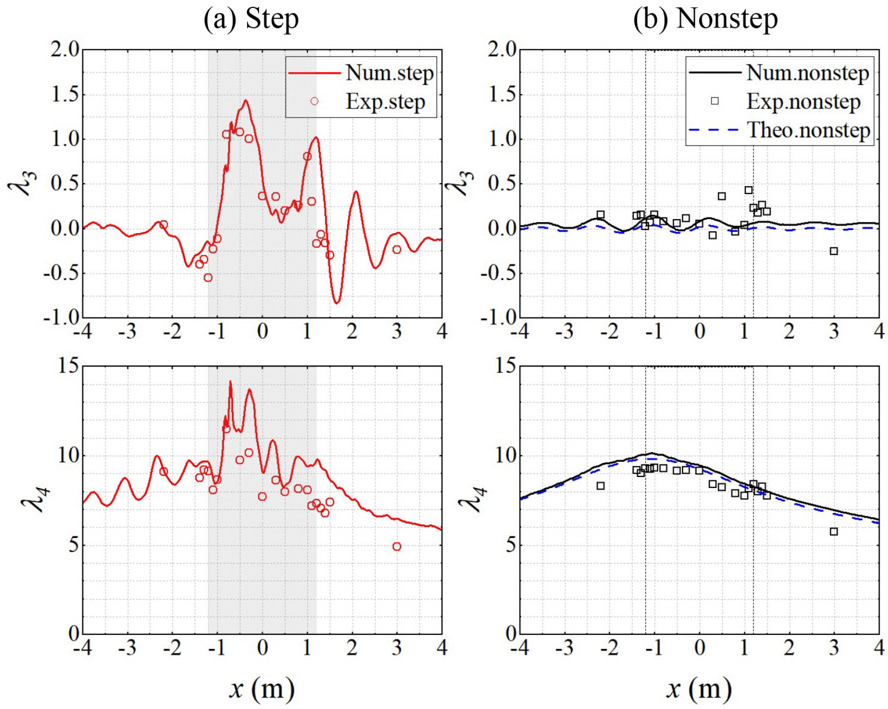

Figure 5.28: Spatial evolution of skewness and kurtosis in step and non-step conditions for Case 7.

However, the discrepancy with the nonlinear results is serious, where the peak crest of nonlinear results is less than that of the superposition of the first four harmonics. The results show that the second subharmonics are added, and the peaks decrease to the same level as the nonlinear results. Contrary to the effect of higher harmonics on the degree of statistics, the second difference component reduces the overall degree of statistics. The strong nonlinearity of wave profiles on the top of steps comprises two parts, the generation of higher harmonics and the upshift of the mean waterline. The inclusion of subharmonics compensates for the asymmetry of the wave surface, resulting in smaller peaks of skewness and kurtosis. Superharmonics and subharmonics have an opposite effect on the skewness and kurtosis in the spatial domain, but the step heightens the overall values of kurtosis.

The effects of wave steepness $k_p a$ and normalized water depth $k_o h_d$ on the statis-

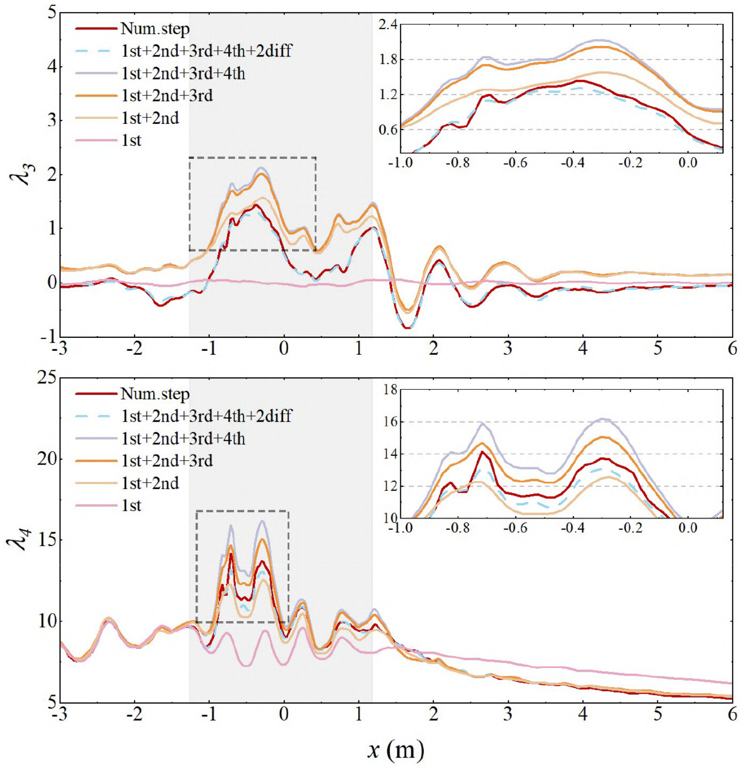

Figure 5.29: Skewness and kurtosis with the superposition of superharmonics in the spatial domain for Case 7.

tics are shown in Figure 5.30 and 5.31. These figures display the peaks of skewness and kurtosis under varying steepness and normalized water depth. Similar to their effects on the superharmonics, a higher k_pa leads to higher peaks of λ_3 and λ_4. Meanwhile, there are downstream shifts of the corresponding positions. Such variations also occur at the second ADT with a minor increment of peaks. When the steepness increases to $k_pa = 0.16$, the position corresponding to the peaks is merely 0.4 m ahead of the middle of the step. Conversely, the maximum value of λ_3 and λ_4 gradually decreases with a higher h_ph_d, as indicated by both the experimental and numerical values (in Figure 5.31). In summary, an increase in steepness k_pa and a decrease in normalized water depth k_ph_d can enhance the statistic in the shallower regions. This induces the higher peaks of skewness and kurtosis, as well as

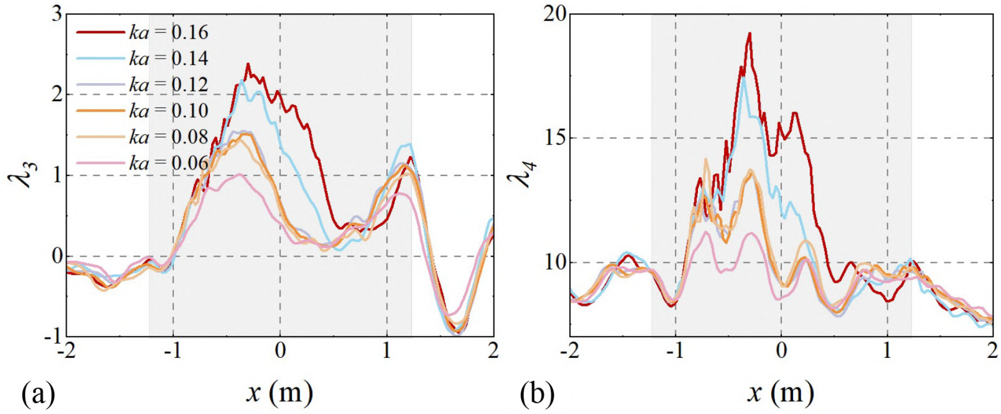

Figure 5.30: Skewness and kurtosis with the variation of wave steepness at $f_p = 0.9$ Hz.

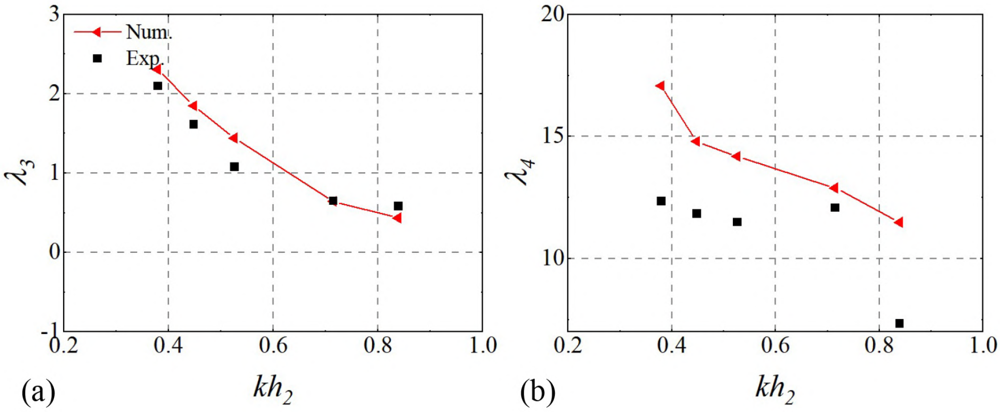

Figure 5.31: Skewness and kurtosis with the variation of normalized wave depth.

the downstream shift of corresponding positions.

5.8 Conclusions

The hydrodynamic performance of focused wave groups over two bathymetries (with and without a submerged step) was studied experimentally and numerically. The characteristics of these focused wave groups were examined from the perspective of the peak crests in space, the superharmonics, and the evolution of skewness and kurtosis, with particular emphasis on the evolution of subharmonics and superharmonics. The measured data agree well with the numerical results. The findings indicate an increase in the peaks of focused waves when propagating over a submerged step. The increasing incident steepness $k_p a$ triggers a nonlinear growth in the crest results and the corresponding positions, implying that the discrepancy between the conditions with and without the steps diminishes as the steepness $k_p a$ increases.

With the decomposition method with a phase-manipulation approach and the Continuous Wavelet Transform (CWT), the superharmonics are effectively extracted in both the temporal and spatial domains. It confirms that the downstream shift of the focused position results from the generation of superharmonics behind the focused position. The frequency range of superharmonics is narrower, with a higher crest after the prescribed focused settings. Moreover, the generation of superharmonics is predominantly reflected in the crests. The results obtained from the superposition of the first two harmonics suffice to resemble the peaks neighboring the crests of nonlinear results. However, the third and fourth components need to be considered to obtain the crests of nonlinear results. A higher $k_p a$ induces greater superharmonics, where the crests of the third and fourth components grow and the corresponding positions shift downstream.

The superposition of higher bound and free waves leads to a sudden drop in the corresponding wave spectrum frequency, despite having the same frequency. This offers a novel method to identify the presence of free waves. In addition, the cause of increased second harmonics is identified, where the second bound and free waves take major responsibility at two depth transitions, respectively. The occurrence of superharmonics triggers the increment of crests and a stronger asymmetry of wave profiles, resulting in higher skewness and kurtosis. On the contrary, the generation of the second subharmonics decreases the values of the two parameters. The depth transition induces a shift downstream of the focused positions of extreme waves, thereby increasing the risk in that area. This understanding is crucial for coastal management and planning, particularly in areas prone to extreme wave events. It highlights the need for comprehensive studies and strategies to mitigate potential risks associated with such wave behaviors.

Chapter 6

Wave resonance over varying bottoms

6.1 Introduction

Extreme waves might cause great damage to coastal structures and also a high threat to human life (Didenkulova et al., 2023; Xiang and Istrati, 2021; Yuan et al., 2021; Zhu and Dong, 2020). Thus, investigating the influence of bathymetry on minimizing extreme waves is of great significance. When the bathymetry and progressing waves meet certain conditions, wave resonance exists with especially high or low reflection coefficients. Specifically, a certain ratio of the water depth in shallower regions to that of deeper regions can induce wave trapping in the shallower regions, resulting in a low reflection coefficient (Neetu et al., 2011). If the bathymetry is periodic, such as ripples, a Bragg resonance of waves exists at the dimensionless parameter $2S/L = 1, 2, 3...$ (S is the wavelength of sinusoidal bottom undulation). In the Bragg resonance, most incoming waves are reflected (Liu et al., 2016). As mentioned before, the focused wave groups have been widely used to represent extreme waves (Fern 'andez et al., 2014; Moideen and Behera, 2021; Ning et al., 2022a; Zeng et al., 2022). However, the reflection of focused wave groups has rarely been studied because the description of the nonlinear wave propagation during complex bathymetries is difficult. The fully nonlinear model using the conformal mapping method shows its advantages in dealing with any type of incident wave and any shape of bottoms (Viotti et al., 2014). Therefore, to consider the nonlinear effects of Bragg resonance, a numerical model is employed to simulate the nonlinear wave resonance with varying bathymetries.

This chapter aims to investigate the wave resonance over varying bottoms using a fully nonlinear numerical model. First, the wave trapping is discussed in Section 6.2.4 with the consideration of trapping frequency. The conformal mapping method employed in the nonlinear model is firstly validated by the measured Bragg reflection and is applied to study the effects of the periodic seabed on the focused wave groups. The convergence and validation of the numerical model are presented in Section 6.3. The effects of parameters of focused waves and different seabed topographies are analyzed in Section 6.4 and Section 6.5. Section 6.6 draws the conclusions and future perspectives.

6.2 Wave trapping with monochromatic waves

6.2.1 Convergence of numerical simulation

To examine the convergence of the numerical model, the wave resistance associated with the release of radiative waves is tested. The wave resistance can be identified with the time derivative of the total horizontal momentum $P_x(t)$ (see Figure 6.1). Consistently, once again, with the measurement of wave resistance presented by Camassa and Wu (1991), the curve $P_x(t)$ starts flat at $t = 0$ s and then monotonically decreases until it stabilizes on a constant value. We compare the horizontal momentum in cases with the trapped frequency and normal frequency. In the trapped frequency 0.94 Hz (obtained in Section 6.2.3), the variation of 32 and 36 points are similar and the comparison of the results with 42 and 52 points are also comparable. The results of the other normal frequency with 1.06 Hz show the same tendency among the six discrete points. Thus, the discrete number 42 is an optional choice that can realize the precise simulation with less computation load and time.

6.2.2 Validation of numerical simulation

The numerical model describes a wave tank with 27 m in length, 0.75 m in width, and 1.5 m in depth, as shown in Figure 6.2. The water depth in the deeper region h_1 is designed and that of the shallower area h_2 is installed 4 m away from the wavemaker. The length of the step is set as 2.4 m and the height of h_2 is kept constant, the height of h_1 is designed as 0.36m. Eight capacitive wave gauges are adopted, and the

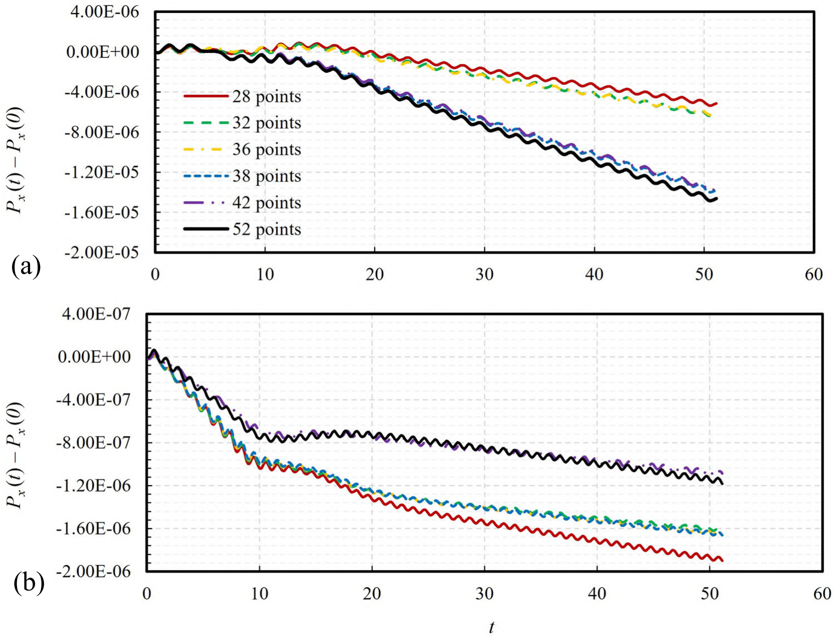

Figure 6.1: Horizontal momentum P_x, for the simulation at (a) f = 0.94 Hz and (b) f = 1.06 Hz.

location of the center on the step is assumed to be zero. Then the distance of WG 1 to WG 8 is -2.2 m, -1.56 m, -1.4 m, -1.2 m, -1.0 m, 0.0 m, +1.1 m and +1.3 m.

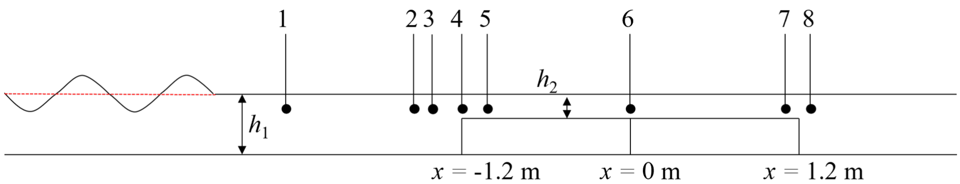

Figure 6.2: Sketch of bottom profile and locations of the wave gauges.

The conformal mapping method has been validated for various conditions (Choi and Camassa, 1999; Viotti et al., 2014). It provides outstanding results for propagation with an adequate computational cost. To verify the results, the evolution of the surface wave is compared with that of the theoretical results (Cokelet, 1977) in Figure 6.3, and the results show good agreement when the steepness ε = 0.13.

The discrepancy becomes clearer with the increase in wave steepness. This is be-

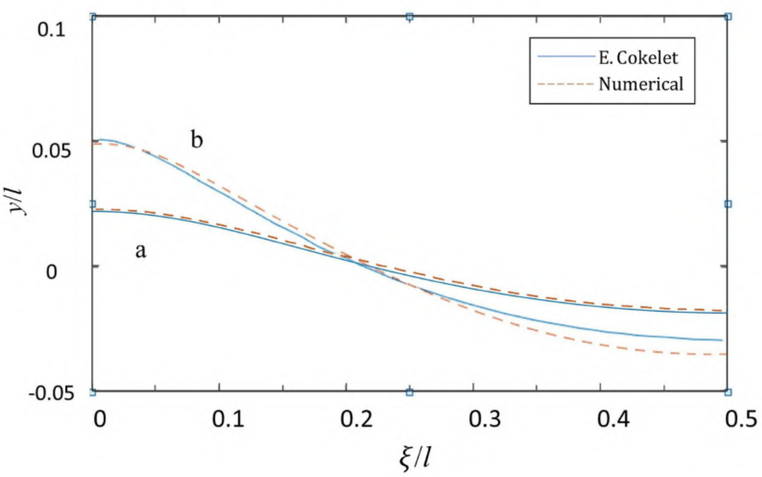

Figure 6.3: Comparison between numerical wave profiles (blue solid lines) and that of theoretical results (red dotted lines) by Cokelet (1977). a. $\varepsilon = 0.13$; b. $\varepsilon = 0.25$.

cause waves with large wave steepness could cause higher nonlinear characteristics. The theory referred to in Cokelet employed a perturbation strategy with expanded coefficients at various orders of accuracy and Pade approximation was used for the expansion series. The accuracy of the theory depends on the truncation of the expanded series. However, our numerical model solves the exact fully nonlinear free surface without approximation. This explains that with higher steepness or nonlinearity, the discrepancy is enlarged. The convergence and validation of numerical models are conducted in the following sections.

6.2.3 Trapping efficiency

The reflection coefficient is a crucial research objective of nonlinear wave propagation over a bottom with varying depths with the shallow long wave theory. A characteristic feature with significant water depth variations is that the reflection coefficient becomes zero when wave trapping occurs. Wave trapping is a phenomenon

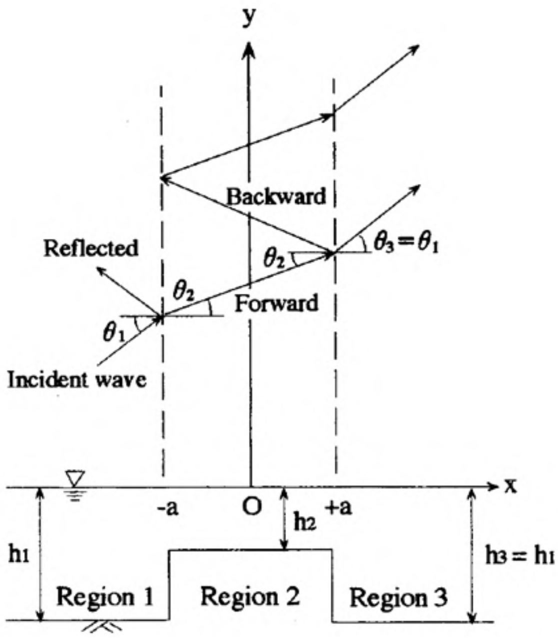

Figure 6.4: Directions of wave vectors at a step (Koshimura et al., 2001).

in which waves are trapped in the shallower region of a step (Neetu et al., 2011). To capture the special wave resonance, calculating the reflection coefficients is a critical initial step.

The reflection coefficients of wave trapping with discontinuous depth variation are solved using the linear long wave theory. The general solution of surface elevations η_1, η_2, η_3 over each flat region (Region 1, 2 and 3) can be written as follows (in Figure 6.4)

$$\eta_1 = e^{i(\beta y - \omega t)} \left\{ e^{i\alpha_1 (x+a)} + A e^{-i\alpha_1 (x+a)} \right\} \quad x < -a, \tag{6.1}$$

$$\eta_2 = e^{i(\beta y - \omega t)} \left\{ B e^{i\alpha_2 x} + C e^{-i\alpha_2 x} \right\} \quad -a < x < a, \tag{6.2}$$

$$\eta_3 = D e^{i(\beta y - \omega t)} e^{-i\alpha_3 (x-a)} \quad x > a, \tag{6.3}$$

where α and β represent the partial wave numbers on the x-axis and y-axis, respectively. The relationship $\alpha_i^2 + \beta_i^2 = k_i^2$ holds for $i = 1, 2, 3$. The subscript of α_1, α_2 and α_3 refers to the regions 1, 2 and 3 over the mapped area. The variable a is half the length of the step. This study has no oblique incident wave, thus, $\beta = 0$ and $\alpha_i = k_i, i = 1, 2, 3$. The variables A, B, C and D represent the complex amplitudes of waves. We assume that the incident wave has a unit amplitude. Then, A represents the amplitude and phase lag of the waves reflected at the left ridge boundary, B corresponds to the waves propagating forward on the ridge, C represents the waves reflected at the right ridge boundary, and D corresponds to the waves propagating forward in region 3.

The coefficients A, B, C and D are determined by ensuring the continuity of the surface elevation η and the derivative of the surface elevation with respect to x, denoted as $h\frac{\partial \eta}{\partial x}$, at the two depth transitions. The continuity of surface elevation and volume flux are written as

$$\eta_1 = \eta_2 \quad \text{at} \quad x = -a, \tag{6.4}$$

$$h_1 \frac{\partial \eta_1}{\partial x} = h_2 \frac{\partial \eta_2}{\partial x} \quad \text{at} \quad x = -a, \tag{6.5}$$

$$\eta_2 = \eta_3, \quad \text{at} \quad x = a, \tag{6.6}$$

$$h_2 \frac{\partial \eta_2}{\partial x} = h_3 \frac{\partial \eta_3}{\partial x}, \quad \text{at} \quad x = a, \tag{6.7}$$

By solving the above simultaneous equations, we obtain the complex amplitudes as

$$A = |\frac{e^{-2ik_2a} - (1 - s_{12})(1 + s_{32}) + (1 + s_{12})(1 - s_{32})e^{-2ik_2a}}{(1 + s_{12})(1 + s_{32})e^{-2ik_2a} - (1 - s_{12})(1 - s_{32})e^{2ik_2a}}|, \tag{6.8}$$

$$B = |\frac{2s_{12}(1+s_{12})e^{-ik_2a}}{(1+s_{12})(1+s_{32})e^{-2ik_2a} - (1-s_{12})(1-s_{32})e^{2ik_2a}}|, \tag{6.9}$$

$$C = |\frac{2s_{32}(1-s_{32})e^{ik_2a}}{(1+s_{12})(1+s_{32})e^{-2ik_2a} - (1-s_{12})(1-s_{32})e^{2ik_2a}}|, \tag{6.10}$$

$$D = |\frac{4s_{12}}{(1+s_{12})(1+s_{32})e^{-2ik_2a} - (1-s_{12})(1-s_{32})e^{2ik_2a}}|, \tag{6.11}$$

where$s_{\mu\nu} = \frac{k_\mu h_\mu}{k_\nu h_\nu}$, $\mu, \nu = 1, 2, 3$, respectively. The reflection coefficient Re, transmission coefficient T and trapping efficiency Γ are written as

$$Re = A, \tag{6.12}$$

$$T = D, \tag{6.13}$$

$$\Gamma = \frac{C}{B} = |\frac{h_2 \tan\theta_1 - h_1 \tan\theta_1}{h_2 \tan\theta_1 + h_1 \tan\theta_1}|, \tag{6.14}$$

6.2.4 Wave trapping with monochromatic waves

To study the coupling effects of wave trapping and wave nonlinearity over depth changes, the size of the immersed step should be carefully designed with respect to the wave trapping efficiency Γ. To validate the application of the numerical model in studying wave resonance, we refer to the research of Chang and Liou (2007) on a continuous trapezoidal bathymetry, which discussed reflection coefficients using the theory of Mei et al. (2005). The reflection coefficients obtained by the present model are compared with those in the literature in Table 6.1. The water depth in the deeper regions h_1 and in the shallower regions h_2 are shown with their ratio, that in the deeper regions downstream is h_3. The results well match those in the literature, confirming the successful reproduction of both reflection and transmitted reflection

Table 6.1: Verification with the theoretical results in the study of Mei et al. (2005).

Case	Case 1 ($h_1 = h_3 = 2.4$ m)			Case 2 ($h_1 = 2.4$ m, $h_3 = 1.6$ m)		
	R	T	$R^2 + T^2$	R	T	$R^2 + T^2$
Results	0.4113	0.9115	1	0.3449	1.0388	1.1980
Mei's theory	0.4114	0.9114	1	0.3450	1.0387	1.1980

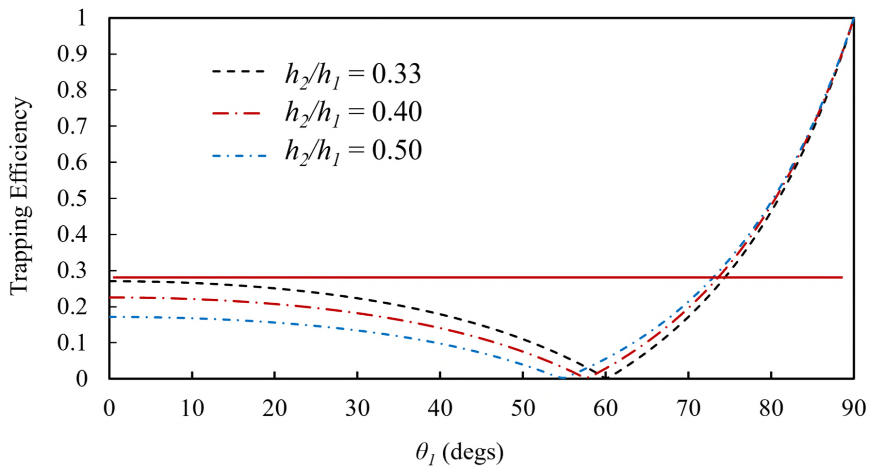

Figure 6.5: Trapping efficiency as a function of θ_1 and h_2/h_1.

calculations. These findings contribute to the preparatory work for subsequent research.

Section 6.2.3 has discussed wave scattering with the linear shallow-water theory. To capture the trapped wave, the sum parameters B and C are considered as a measure of the magnitude of waves on the step. Results are obtained and shown in Figure 6.5. When this sum arrives at a peak, it can be said that wave trapping is excited. As mentioned in Section 6.2.3, trapping efficiency is dependent on incidence angle θ_1 and water depths at shallower and deeper areas. The relationship among trapping efficiency, incidence angle and ratios of h_2/h_1 is shown in Figure 6.5. At each fixed h_2/h_1, the trapping efficiency decreases gradually to 0 with the increase of incidence angle first. It decreases to 0 at an incidence over 55 degrees. Then, the trapping efficiency boosts high with the increasingly larger θ_1. Normally, strong wave trapping is considered to occur when the trapping efficiency is achieved above 0.5. On the other hand, if θ_1 is fixed, when θ_1 is small, the smaller the value of h_2/h_1, the higher the trapping efficiency will be. By contrast, if θ_1 is large, the larger value of h_2/h_1 will cause a smaller trapping efficiency. Thus, the optional group of h_2/h_1 and incidence angle should be accurately designed to capture the wave trapping phenomenon.

From the analysis of trapping efficiency, there are two main approaches to realize the wave trapping phenomenon, large incidence angle or small value of h_2/h_1. In other words, when the length of a step is fixed, either an increase in the incidence angle or a decrease of h_2/h_1 can enhance the wave trapping. For the further verification of the numerical model with experiments, this study chooses a normal incidence where θ_1 is zero with a relatively small value of h_2/h_1. The definition of the reflection coefficient is the ratio of the amplitude of the reflected wave and the incident wave in region 1 (in Figure 6.4). The wave trapping efficiency is the amplitude ratio of waves propagating backward to those forward on the step (region 2). From the definition of the two terms, when trapping efficiency is large, the corresponding reflection coefficient is small since most of the waves are trapped in the upper region of the step.

Moreover, the excitation condition in terms of the wave number α_2 and the step breadth $2a$ can be expressed by

$$2\alpha_2 k_2 = 2n\pi, (n = 1, 2, 3...), \tag{6.15}$$

We can translate the feature of Eq. 6.15 into the wave period of the trapped mode as follows. The wave number in the x-direction (α_2) is related to the wave number in the direction of wave propagation on the step (k_2) by the following expression,

$$k_2 = \frac{2\pi}{L} = \frac{2\pi}{\sqrt{gh_2 T}}, \quad as \quad c^2 = gh, \tag{6.16}$$

where β is the wave number in the y-direction. From Eq. 6.16, the tsunami wave period on the step is obtained as

$$T = \frac{2\pi}{\sqrt{\alpha^2 + \beta^2}} \frac{1}{gh_2} = \frac{2\pi}{\sqrt{gh_2}} \frac{1}{1 + \sqrt{\tan^2 \theta_2}}, \tag{6.17}$$

where

$$\tan^2 \theta_2 = \frac{\beta}{\alpha_2}, \tag{6.18}$$

with the substitution of

$$\frac{\sqrt{gh_1}}{\sin \theta_1} = \frac{\sqrt{gh_2}}{\sin \theta_2}, \tag{6.19}$$

which is the so-called Snell's law, and Eq. 6.15 into Eq. 6.16 yields Eq. 6.17. This can be interpreted as the wave period of the trapped-mode wave. The wave period of the trapped-mode wave depends upon the water depths h_1 and h_2, step breadth $2a$, incident angle θ_1 and the number of modes n.

$$T_{tp} = \frac{2a}{n\sqrt{gh_2}} \frac{1}{\sqrt{1 + \tan^2 \left\{ \sin^{-1}(\sqrt{h_2/h_1} sin\theta_1) \right\}}}, \tag{6.20}$$

The reflection coefficients of the simulated results on the first four trapped modes and the other two frequencies are simulated which agree well with the theoretical results (in Figure 6.6). We observe that the reflection coefficients can be very small at the corresponding trapping frequencies, which means that most of the long waves travel over the step. Except for the special cases, other wave frequencies

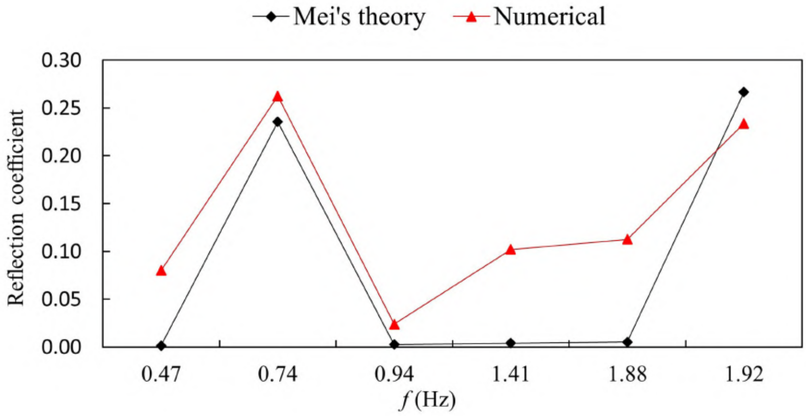

Figure 6.6: Comparison of theoretical reflection coefficients and simulated reflection coefficients on the $f = 0.47$ Hz, 0.74 Hz, 0.94 Hz, 1.41 Hz, 1.88 Hz and 1.92 Hz with wave height H = 0.002.

show normal reflection effects. To compare the reflection coefficients of different wave steepness, the wave height remains the same on the 6 wave frequencies so a range of wave steepness can be considered ε = 0.01, 0.02, 0.04, 0.08, 0.14, 0.15. In Figure 6.6, the first three simulation results show good agreement with the theoretical ones as the wave propagation with small wave steepness can be described by the shallow long water theory. However, with the increase in wave height, there are larger discrepancies between the simulation and theoretical results. Since the wavelength becomes shorter, the same wave height leads to larger wave steepness and more complicated wave propagation. When ε is larger than about 0.05, it is difficult to apply the theory to the nonlinear wave propagation. Nonetheless, the numerical simulation allows for further cases in this condition.

Figure 6.7 displays the surface elevation under the four specific wave frequencies. (x, η) is a Cartesian coordinate system where η is the upward vertical coordinate showing the wave amplitude and the right upward vertical coordinate indicating

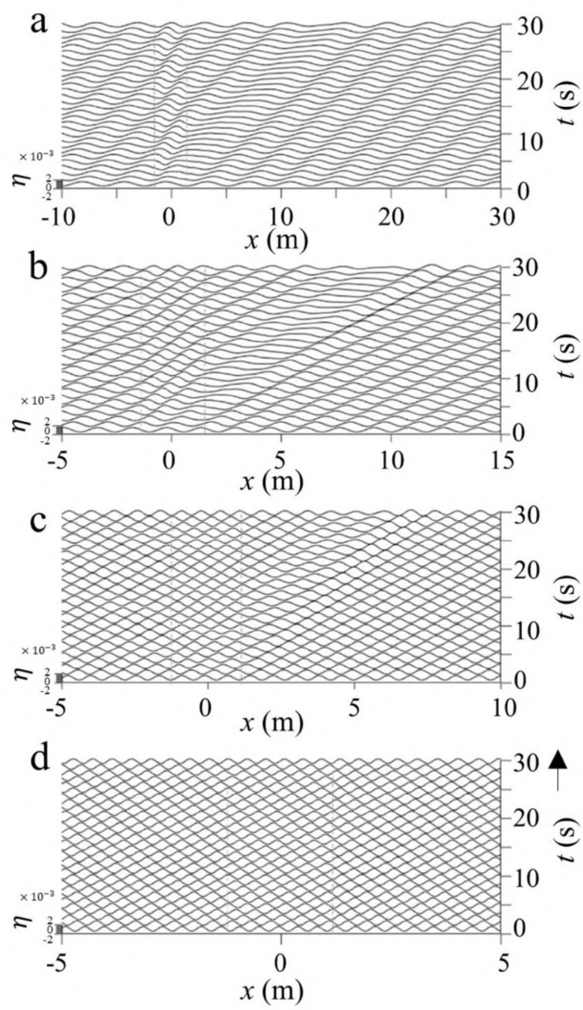

Figure 6.7: Free surface elevation on the first four trapped conditions: (a) $f = 0.47$ Hz; (b) $f = 0.94$ Hz; (c) $f = 1.41$ Hz and (d) $f = 1.88$ Hz.

the time domain. The time domain is 30 seconds, which can cover the maximum wave period. The agreement of the propagation trend is good, but the trapped effects evanesce with the rise of trapped mode. As the wave propagates toward the right side, the same phase shifts happen; the wavelength grows after transmitting the submerged step. In addition, the wavelength decreases on the upper domain on the step since it needs to reach a new equilibrium where h_2 suddenly becomes small. Notably, part of the wave is tapped where existing reflective waves travel backwards and forward after about 13 seconds in the first two modes. The other two plots have no obvious wave trapping. This could be explained by the small wave trapping efficiency since it cannot be very high without obliquely except for the extremely large value of h_2/h_1. In terms of the third and fourth trapped modes, the effects of refraction become weaker due to the rise of trapped wave numbers.

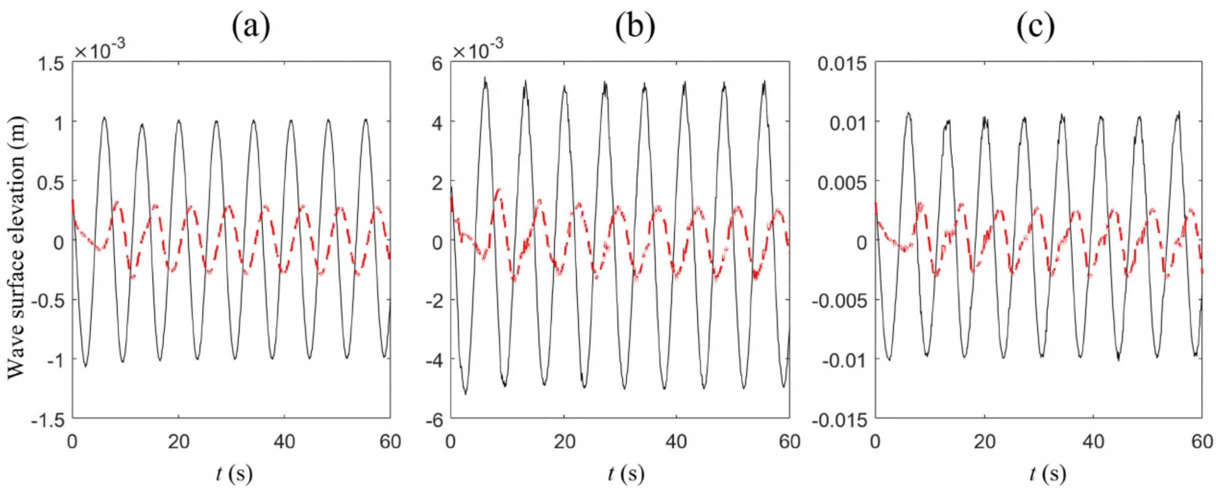

Figure 6.8: Incident (black solid line) and reflected wave (red dash line) of $f = 0.74$ Hz: (a) $H = 0.002$ m, $\varepsilon = 0.02$; (b) $H = 0.01$ m, $\varepsilon = 0.1$ and (c) $H = 0.02$ m, $\varepsilon = 0.2$.

To investigate the influence of the wave steepness, three groups of steepness are simulated on the wave with a frequency of 0.74 Hz (in Figure 6.8). The incident and reflected wave can be separated by Wang et al.'s method (2003). With two wave gauges located before the step, the harmonic amplitude is computed to find the reflection situation by carrying out the conventional DFFT on the time series of free-surface elevations. We can see that with the increase in steepness, the nonlinearity of reflected waves becomes more obvious. In addition, there is no clear change in Re though the nonlinearity becomes stronger.

Eight capacitive wave gauges are adopted, and the location of the center on the

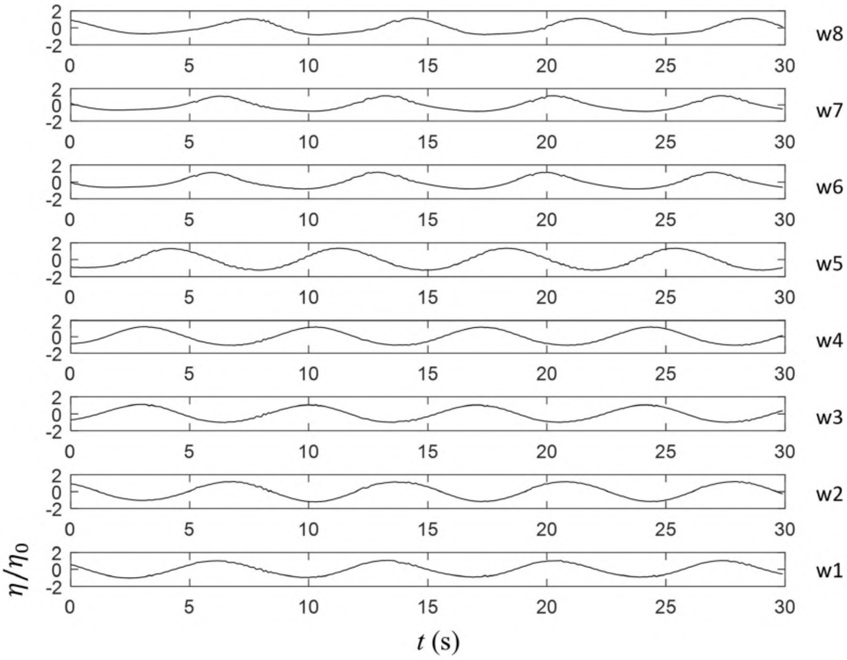

Figure 6.9: Wave surface profiles at each wave gauge with the $f = 0.74$ Hz, $H = 0.02$ m, $\varepsilon = 0.2$.

step is assumed to be zero. Then the distance of wave gauge 1 to wave gauge 8 is -3.0 m, -1.6 m, -1.4 m, -1.2 m, -1.0 m, +1.1 m and +1.3 m. The time distribution of surface elevation at the 8 wave gauges is plotted to show the change of wave profiles (in Figure 6.9). It is clear that the wave crest becomes sharper at the latter wave gauges with a flatter wave trough. Figure 6.10 described the wave spectra of wave surface elevation recorded at WG 2 and 3. Since the wave surface profile can be described as $\eta = A\cos(\sigma t) + B\sin(\sigma t)$. The coefficients A and B can be obtained by Fourier transformation. The spike of the graph refers to the corresponding frequency existing in the wave profiles. It can be noticed that with the increase of wave amplitude, the wave amplitude separated is larger and more spikes are shown in the results, resulting in the harmonic wave being generated. Moreover, the corresponding frequencies in the result not only include 0.14 but also 0.28 and 0.42 (part

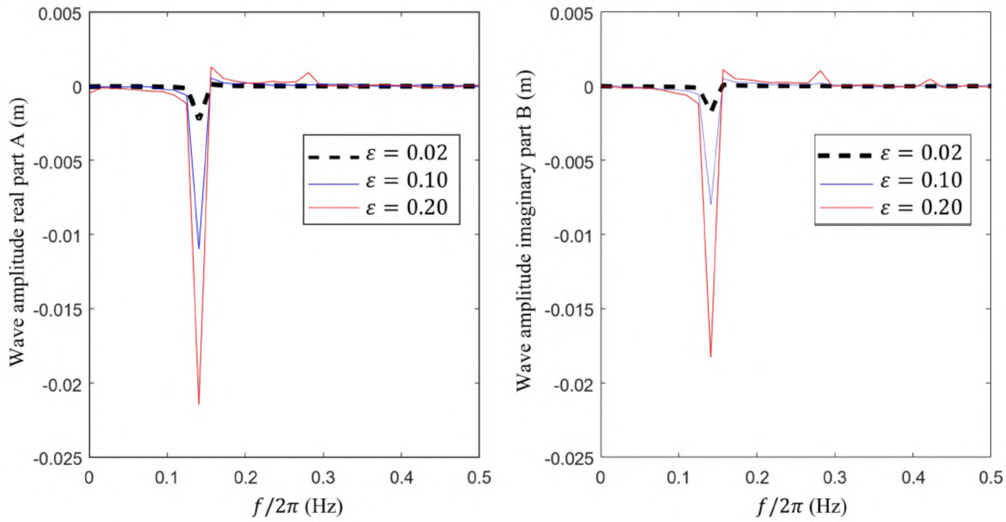

Figure 6.10: FFT coefficients of time series wave surface elevation of WG 2 and 3.

B in Figure 6.10) which indicates that the second and third harmonic waves are generated due to the wave-structure interaction. However, the other two cases only show the incident frequency, which indicates the linear theory can well describe the propagation.

The evolution of the skewness and kurtosis of the free surface elevation on the four trapped conditions and two frequencies with high reflection coefficients are shown in Figure 6.11 and Figure 6.12. As mentioned before, the effect of trapping is small on the third and fourth trapped modes, and the result of the skewness and kurtosis can also be small. In Figure 6.11, the skewness shows similar increasing and decreasing trends on the second depth transition of the step. Before the center of the step, the skewness is almost 0 or oscillating around 0. For the higher trapped mode, the change of skewness becomes quicker as the wavenumber increases. The skewness indicates the asymmetry of the probability distribution of the considered variable. A positive skewness indicates waves with sharper crests and flatter troughs

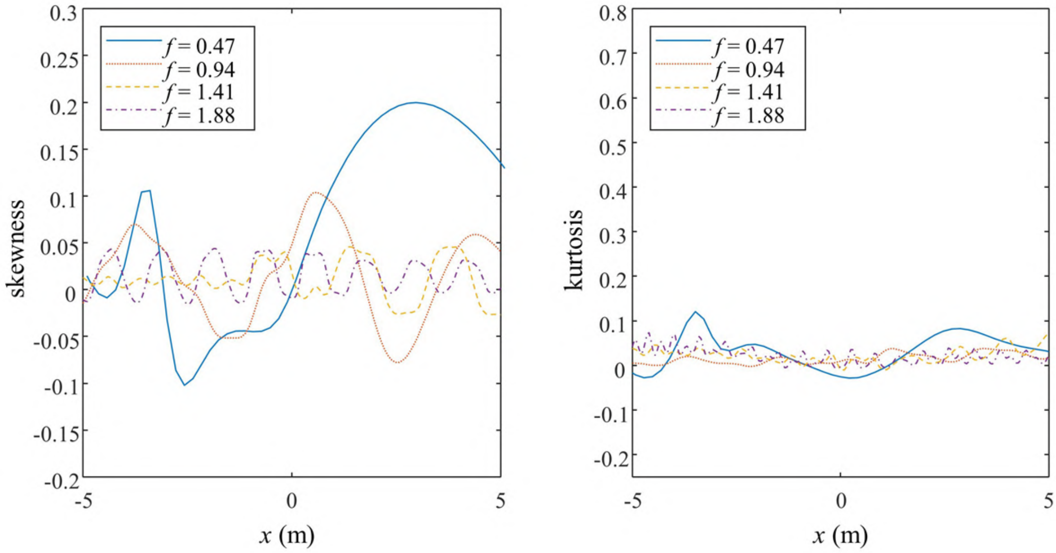

Figure 6.11: Spatial evolution of wave skewness and kurtosis on the four trapped modes.

and vice versa for negative values. Thus, there is a relatively symmetric surface wave profile in the deeper region and the wave develops as an asymmetric profile with higher skewness in the shallow region and finally decreases again after propagating over the step.

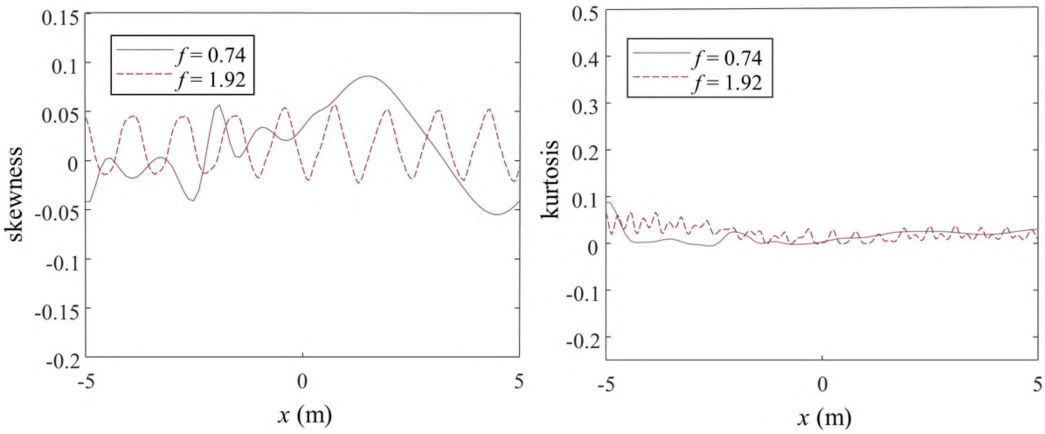

Figure 6.12: Spatial evolution of wave skewness and kurtosis at the two frequencies with high reflection coefficients.

In terms of kurtosis, a comparable trend among the four trapped modes shows a gradual increase after the second depth transition. The standard kurtosis is 3 for a Gaussian distribution. There the standard kurtosis equals 0 by decreasing 3. The maximum kurtosis of the second and third trapped modes arrives at the same position, both located nearly 4 m after the second water depth change. The kurtosis of the first trapped mode starts earlier in the middle of the step. For the second trapped mode, the growth of kurtosis can cause a higher probability of the occurrence of extreme waves. Figure 6.12 shows the skewness and kurtosis of the wave profiles with normal reflection coefficients. The change of skewness for the frequency of 0.82 Hz agrees well with that of the other frequencies, where there is an increment in the shallow area and a drop in the deep area. For the skewness with a frequency of 1.52 Hz, the change of skewness is not clear, which is similar to the condition of the fourth trapped mode. This may result from the relatively small wavelength. Both high frequencies lead to the short wavelength, and the water area becomes the deep-water region. In consequence, the nonlinearity of waves with high frequency can be ignored and the calculation of reflection coefficients is only stable for part of the incident wave frequency which makes sure the region is a shallow or intermediate one. The maximum kurtosis is similar to that of the trapped modes when the wave frequency is 0.8 Hz. Even if no wave trapping happens, the high reflection effects may also cause an abnormal wave.

6.3 Numerical model of focused waves propagation over periodic bathymetries

6.3.1 Convergence of numerical model

To achieve an exact solution of wave profiles over periodic bottoms, the convergence of the numerical model has been tested. A range of wave groups with different discrete Fourier points per wavelength were simulated with the numerical model. The comparison of focused wave profiles is shown in Figure 6.13 with discrete points varying from 15 to 60 per wavelength for two cases (Baldock et al., 1996; Davies and Heathershaw, 1984). The case parameters are referred to as Case B in Baldock et al. (1996) with the constant water depth $h_0 = 0.7$ m and the crest of focused wave groups as $a = 0.022$ m. It can be found that focused wave profiles become almost identical when the number of discrete Fourier points is larger than 30 per wavelength. The discrete Fourier points 50 per wavelength are sufficient to capture the accurate nonlinear focused wave propagation over a constant depth or varying depths. In the simulations in this study, 50 Fourier points are employed. Owing to the nature of the conformal mapping method, the efficiency of the simulation is generally very high. Further details can be found in Wu et al. (2023).

6.3.2 Validation of numerical model

To examine the capability of the present fully nonlinear numerical model in studying Bragg resonance, the reflection coefficients of a group of monochromatic waves

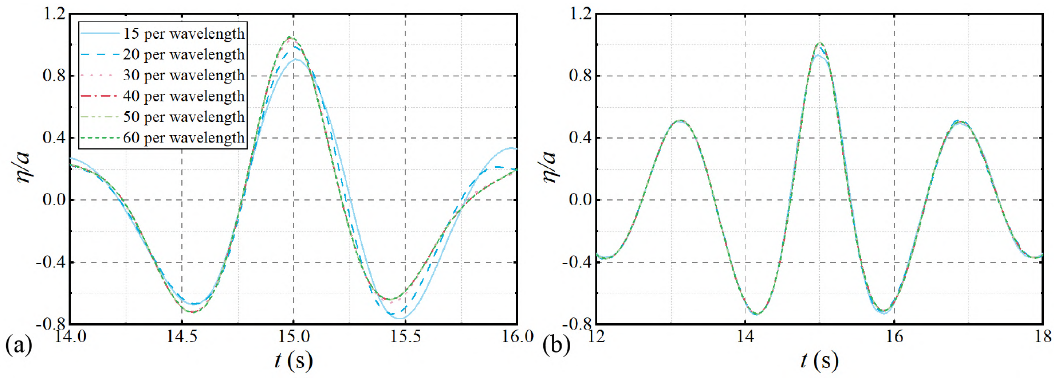

Figure 6.13: Surface elevations of focused wave group at focusing with (a) the constant depth and (b) the 4 ripples.

Table 6.2: Bar parameters

Case	D (m)	S (m)	M	h_0 (m)
D1	0.05	1.00	2	0.156
D2	-	-	4	0.156
D3	-	-	10	0.313

are compared with previous studies (Davies and Heathershaw, 1984; Gao et al., 2021; Hsu et al., 2007). Ripples were commonly used in the literature to study Bragg resonance. Davies and Heathershaw (1984) conducted a series of experiments using regular waves over ripples, mainly using the seabed with four or 10 ripples to excite the Bragg resonance. The reflection coefficients of regular waves are shown in Figure 6.14. The parameters of the periodic seabed are shown in Table 6.2. D and M denote the amplitude and number of ripples, respectively. S is the spacing, the distance between two adjacent ripples. Note that the water depth h_0 is different in Cases D1 ($h_0 = 0.156$ m), D2 ($h_0 = 0.156$ m) and D3 ($h_0 = 0.313$ m). These case parameters will be adopted in the numerical model's validation and used in the following discussion of resonant coefficients. Here two water depths are employed to observe the difference in hydrodynamic characteristics.

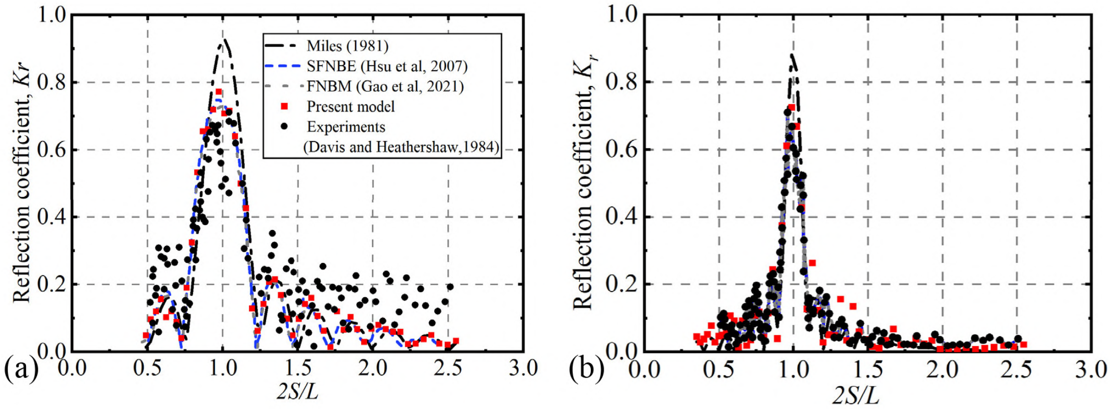

Figure 6.14: Reflection of regular waves over the ripples (a) $M = 4, h_0 = 0.156$ m (Case D2) and (b) $M = 10, h_0 = 0.313$ m (Case D3).

Miles (1981) proposed the theoretical expression of reflection coefficients with monochromatic wave propagation over ripples in the framework of the linear potential flow theory. Then Hsu et al. (2007) optimized a fully nonlinear model with the second-order Boussinesq equations (SFNBE) and verified the model with the measured data by Davies and Heathershaw (1984). Lately, Gao et al. (2021) established a fully nonlinear Boussinesq model (FNBM) where the numerical results are also compared with the present model. In Figure 6.14, numerical results obtained by the present fully nonlinear model are well validated by the experimental and numerical results for the two types of ripples D2 and D3. It is seen both the Bragg resonance and bandwidth of peak wave reflection are well captured using the present fully nonlinear model. The agreement between the present model and the FNBM and SFNBE results is excellent.

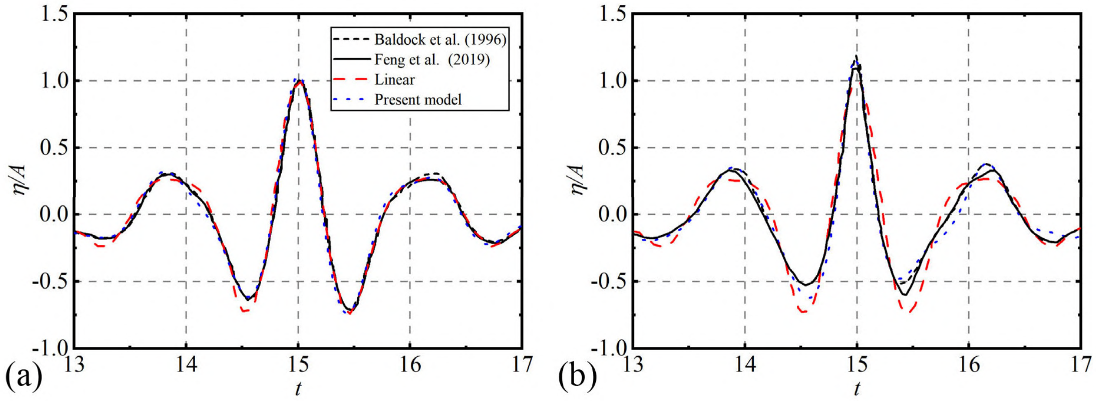

Figure 6.15: Wave profiles of the focused wave group at the focused position for (a) a = 0.022 m and (b) a = 0.055 m.

6.3.3 Validation for focused wave groups

To verify the simulation of the focused wave group using the present model, the focused wave profiles are compared with the measured data in the work of Baldock et al. (1996) and the numerical results in the study of Feng (2019), as shown in Figure 6.15. In Baldock et al.'s study, the wave period T of wave groups was generated with $0.6 \leq T \leq 1.4$ with 29 monochromatic wave components, where the wave periods were evenly divided. The water depth $h_0 = 0.7$ m and two incident crests of focused wave groups at $a = 0.022$ and 0.055 m are employed. The linear results (NewWave theory) are found not sufficient to describe the nonlinear wave profiles since the wave-wave interaction is complicated during the evolution. It can be found that the numerical results reproduce the sharp and high crest and agree well with the measured and other numerical results. Consequently, focused wave groups as extreme waves can be well simulated in the numerical model.

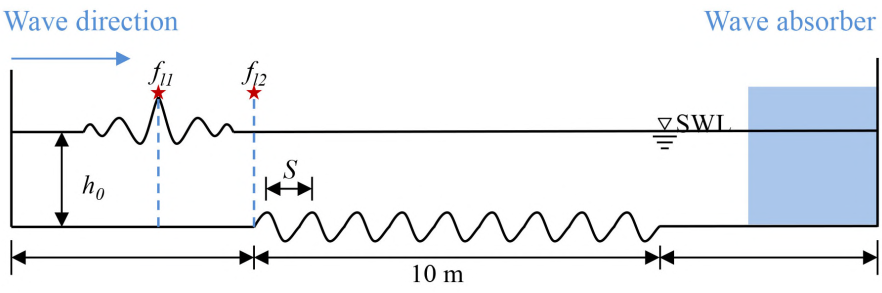

Figure 6.16: Sketch of the numerical tank and location of two focused positions $x_{f_{l1}}$ and $x_{f_{l2}}$.

6.4 Bragg reflection with a focused wave group over ripples

In this section, the influence of different focused wave groups on the Bragg reflection is discussed. Varying parameters of focused wave groups are considered, including amplitude and focused position. The numerical tank is designed to be long enough for the nonlinear evolution of the wave group propagation, as shown in Figure 6.16. Existing studies have widely investigated the Bragg reflection with varying monochromatic waves; however, the Bragg reflection of extreme waves has been rarely studied. Here, the focused wave groups, as representative of extreme waves are considered with their propagation over ripples.

6.4.1 Nonlinear effects

As mentioned in Section 3.3.3.2, the crests of focused wave groups vary with time during the propagation. Thus, how to define the reflection coefficients of focused wave groups shall be addressed first. The existing studies about the reflection of focused wave groups mainly study the crests in the spatial domain, and none of

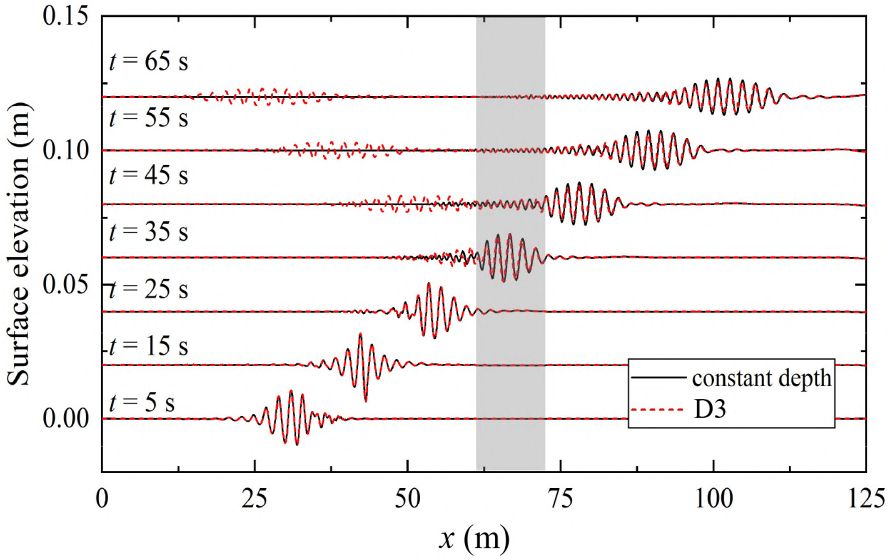

Figure 6.17: Propagation of focused wave group over 10 ripples (Case D3) with $a = 0.015$ m.

them discuss the calculation of reflection coefficients. Referring to the reflection coefficients of irregular waves and the response amplitude operator (RAO), the total reflection coefficient Kr can be defined as

$$Kr = \sqrt{\frac{\sum_i S(f_i)df \cdot R_i^2}{\sum_i S(f_i)df}}, \tag{6.21}$$

$$R_i = \frac{S_r(f_i)}{S_f(f_i)}, \tag{6.22}$$

where f_i is the frequency of each wave component in a wave group. The reflection coefficients R_i and the spectral density function $S(f_i)$ correspond to the ith frequency component. The subscripts 'r' and 'f' denote reflected waves and the incident focused waves, respectively. The reflected wave is the difference between the surface elevation at varying water depth and constant depth at the same location, and the location is 2.5 times the wavelength before the depth change. The surface elevations at the focused position on the constant water depth are used for the incident

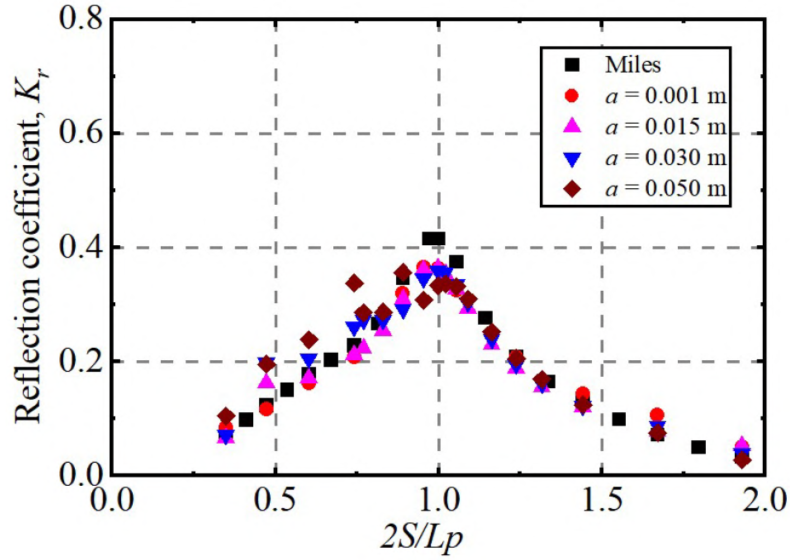

Figure 6.18: Reflection coefficients of focused wave groups ($(0.5-3)f_p$) with varying incident amplitudes over 10 ripples (Case D3).

waves.

The evolution of the focused wave group at the Bragg frequency over the constant depth and the seabed with 10 ripples for Case D3 is shown in Figure 6.17. The time interval is 10 seconds and $a = 0.015$ m, where the wave group is set to focus at the time instant $t_p = 16$ s and the location $x_{f_{l1}} = 44$ m (16 m before the ripples). A decrease in the crest was found when the focused wave group propagates over the depth changes ($t = 35$ s), especially for the neighboring crests. In addition, the reflected waves can be observed upstream. The attenuation of focused wave groups is obvious since the amplitudes of the wave group behind ripples are smaller. Reflection coefficients for Case D3 are displayed in Figure 6.18 where the water depth is $h_0 = 0.313$ m. The reflection coefficients at different incidence steepness are compared with those calculated theoretically by Miles (1981). The peak Bragg reflection occurs around $2S/L_P = 1.0$, which can be found in the cases with different incident amplitudes $a = 0.001$ - 0.030 m and the theoretical results. With an increase of a, a minor upshift of the corresponding $2S/L_P$ is found. Specifically, the case with $a = 0.050$ m has the smallest peak and the highest $2S/L_P$.

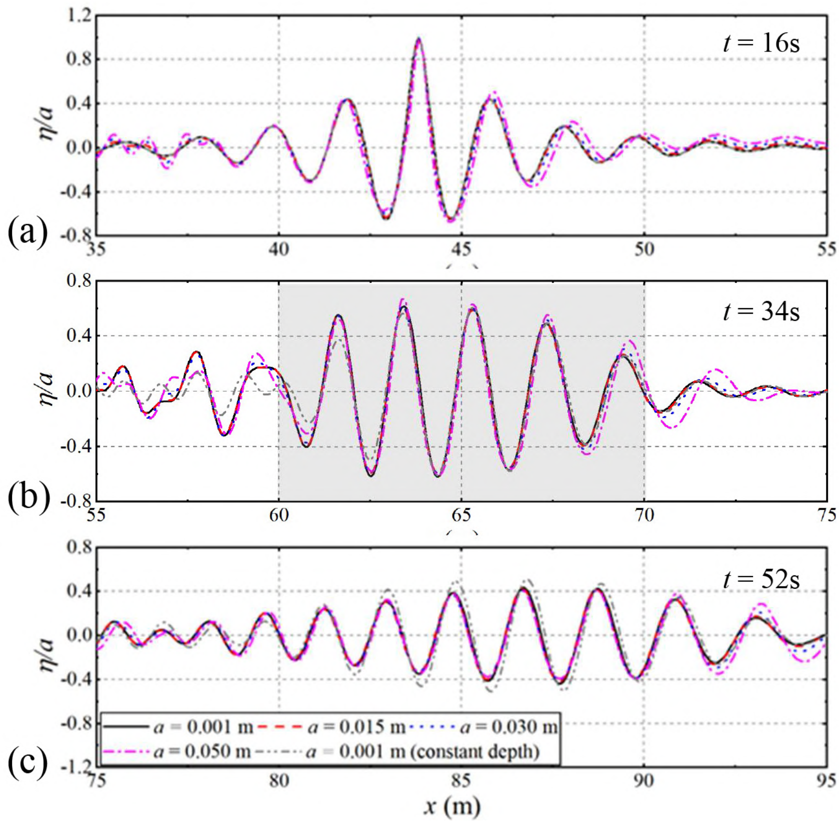

Figure 6.19: Focused wave group in the spatial domain over 10 ripples (Case D3) at (a) $t = 16$ s; (b) $t = 34$ s and (c) $t = 52$ s.

The nonlinear focused wave profiles with different amplitudes at three time instants for Case D3 are shown in Figure 6.19. The x-axis is the distance to the wave maker, y-axis is the nondimensional surface wave elevations. The resonant frequency ($f_p = 0.767$ Hz) is chosen to show the wave resonant profile. The three time instants include the focused time, the occurrence of maximum elevations over ripples and the time after the focused wave past the ripple. It can be observed that the peak elevations are achieved at the focused time $t_f = 16$ s and the focused position $x_{f_{l1}} = 44$ m. A clear asymmetry in the wave profile is found when the amplitude increases to $a = 0.050$ m. The maximum normalized elevation over the ripples is about 0.67 at $t = 34$ s, which is smaller than that at the focused time. We also compare the normalized peaks with those in the constant water depth with $a = 0.001$ m. It is found that the peaks over 10 ripples are higher than those in the constant depth. This indicates the existence of ripples can enhance the crests of focused wave groups over ripples. When the focused wave group propagates past the ripples ($t = 52$ s), the maximum value is only 0.42, whereas the normalized crest of the focused wave group is 0.51 without the ripples. This means the ripples are effective in attenuating wave groups. With varying amplitudes, only small differences in crests are found on the tails of focused wave profiles at $t = 34$ s. Higher incident amplitudes cause strong asymmetric crests over the ripples, but the incident and transmitted wave profiles are nearly the same.

To further study the influence of incident wave amplitudes, the energy spectra of incident and transmitted waves are shown in Figure 6.20. To compare the spectra of waves with different amplitudes, the surface elevations were normalized with the incident amplitude. Discrepancies are found in the tails of the incident spectra (f/f_p > 1.6). Higher amplitudes induce stronger nonlinearity, and the effect is mainly seen in the enhancement of subharmonics and superharmonics. In addition, the increase of wave group amplitude drives a higher spectral tail of both the incident and the transmitted waves. A great reduction of wave components at the fundamental frequency is observed. The existence of ripples decreases the wave energy of both the fundamental waves and the second harmonic wave.

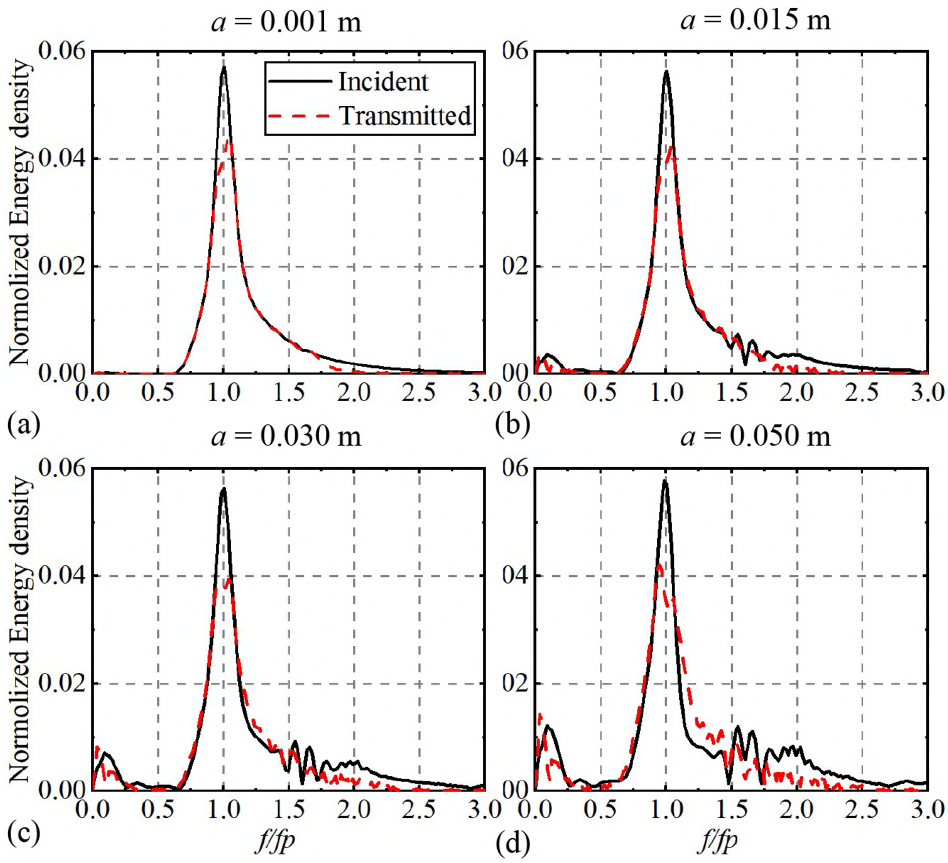

Figure 6.20: Normalized energy spectra of the incident and transmitted waves over 10 ripples (Case D3) with (a) $a = 0.001$ m; (b) $a = 0.015$ m; (c) $a = 0.030$ m and (d) $a = 0.050$ m.

6.4.2 Effects of focused positions

So far, the focused position is set at $x_{f_{l1}} = 44$ m, 16 meters before the ripples. To study the effect of focused position on Bragg resonance, the reflection coefficients of focused wave groups at two different focused positions are compared ($x_{f_{l1}} = 44$ m, $x_{f_{l2}} = 60$ m as shown in Figure 6.16). In addition, two different seabeds with 4 ripples and 10 ripples are employed (Cases D2 and D3). Figure 6.21 shows that the resonant peaks are higher with the focused position $x_{f_{l2}}$, which is at the beginning of ripples. Meanwhile, the bandwidth of Bragg reflection becomes narrower than that

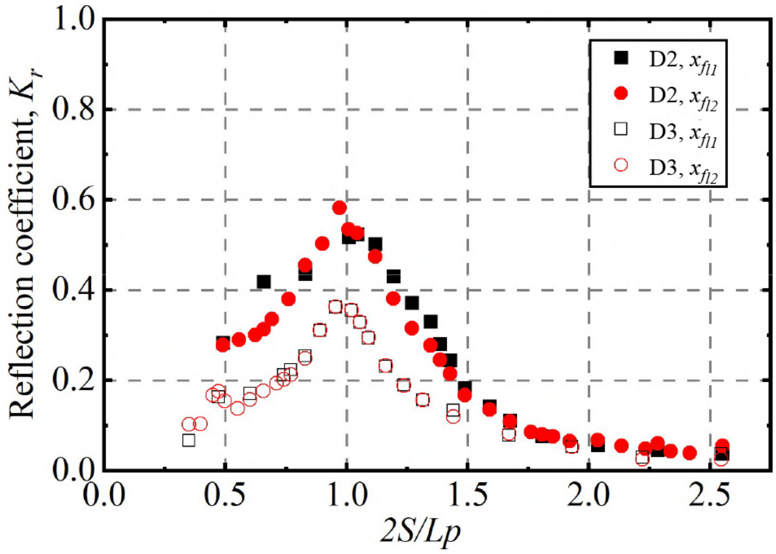

Figure 6.21: Reflection coefficients over 4 ripples (Case D2) and 10 ripples (Case D3) with two different focused positions $x_{f_{l1}} = 44$ m, $x_{f_{l1}} = 60$ m with $a = 0.015$ m and frequency range $(0.5 - 3.0)f_p$.

with $x_{f_{l1}}$. For Case D3, the discrepancy of reflection coefficients with two focused positions is small. To sum up, the resonant peaks with $x_{f_{l2}}$ are higher than those with $x_{f_{l1}}$. It indicates that the focused position near the abrupt depth change induces a higher wave reflection and, hence, a more effective wave absorption.

6.5 Bragg resonance with three bottom configurations

In order to study the effect of the bottoms on the resonant reflection, three types of seabed configurations are employed. In this section, the configurations of the seabed, including ripples, rectified cosinoidal bars and steps, are considered (in Figure 6.22). Compared with ripples, the rectified cosinoidal bars are half the ripple in the horizontal direction. The rounded corners of the rectified cosinoidal bars become sharp at the seabed with steps. The effects of the number M, spacing S, height

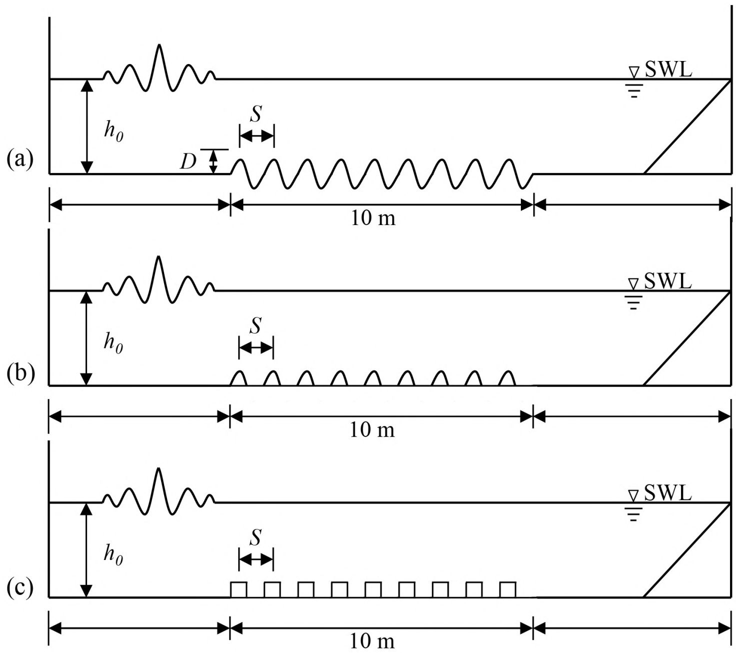

Figure 6.22: Three types of seabed configurations: the ripples, rectified cosinoidal bars and submerged steps with $D = 0.05$ m, $S = 1.0$ m and $M = 10$ (Case D3): (a) ripples; (b) rectified cosinoidal bars and (c) steps.

of seabed D and width (W_1, W_2) on the Bragg resonance are studied numerically.

6.5.1 Wave reflection by three types of seabed configurations

Previous studies have focused more on Bragg resonance with seabed configurations of ripples, subject to regular waves (Gao et al., 2021; Ning et al., 2022a; Suh et al., 1997). Here, we also simulate the rectified cosinoidal bars and steps with the incident waves as focused wave groups. The crests of focused wave groups is set as $a = 0.015$ m to realize a more clear reflection coefficient (in Figure 6.18). Figure 6.23 and 6.24 display the reflection coefficients with three types of configurations for Cases D2 and D3, respectively. The Bragg resonance is captured for all cases. The frequency bandwidth of Bragg reflection with ripples is found to be the broadest one. Meanwhile, the reflection coefficients with steps are slightly higher than those

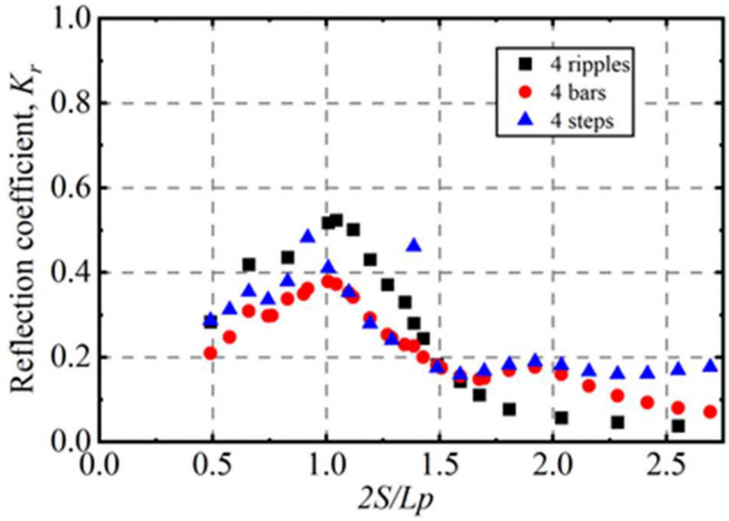

Figure 6.23: Reflection coefficients over three types of seabed configurations with the incident amplitude $a = 0.015$ m and frequency range $(0.5 - 3.0)f_p$, $M = 4$ (Case D2).

with rectified cosinoidal bars for all cases. It should be noticed that the reflection coefficients with ripples are the highest at the relative wavelength $2S/L_P = 1.0$, however, the coefficients are the lowest when the $2S/L_P$ is larger than 1.5. This phenomenon is obvious in shallower water depths with $h_0 = 0.156$ m (Cases D2). Consequently, to excite a higher resonant peak, the type of seabed configurations should be chosen based on the relative wavelength. If $2S/L_P < 1.5$, the ripples result in the highest resonant peaks and a broader bandwidth. On the contrary, the seabed with periodic steps induces the highest reflection coefficients.

6.5.2 Shift of second-order Bragg resonance frequency

For each type of the configurations, the effects of the number of bars are studied for $M = 2, 4, 10$ at the water depth $h_0 = 0.156$ m. Figure 6.25 displays the reflection coefficients with ripples and rectified cosinoidal bars, respectively. It is found that

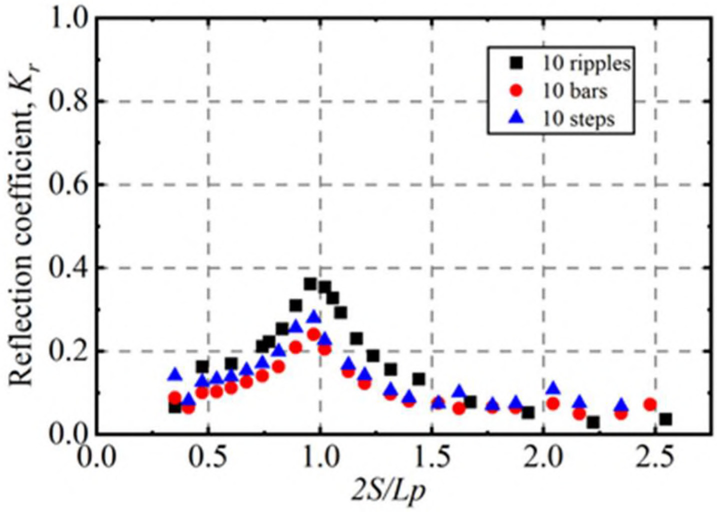

Figure 6.24: Reflection coefficients over three types of seabed configurations with the incident amplitude $a = 0.015$ m and frequency range $(0.5 - 3.0)f_p$, $M = 10$ (Case D3).

the resonant peaks become higher with the increase in the number of bars. For instance, the resonant peak (0.39) with 4 rectified cosinoidal bars is 1.5 times higher than that (0.22) with 2 rectified cosinoidal bars. The corresponding bandwidth of Bragg resonance becomes broader.

A second-order Bragg resonance is observed in the cases with rectified cosinoidal bars (in Figure 6.25(b)). Except for the fundamental Bragg resonance ($2S/L_P = 1.0$), a local increase of reflection coefficients can be found for the cases with rectified cosinoidal bars at $2S/L_P = 2.0$. In this condition, the wavelength L is half of the peak wavelength L_P. Under the strong interaction between focused wave groups and finite periodic rectified cosinoidal bars, it is rational that the relation between the wavelength of the superharmonics and that of the rectified cosinoidal bars at $2S/L_P = 2.0$ excites the second-order Bragg resonance. The peaks of the second-order Bragg resonance are found to be half of that of the fundamental Bragg resonance. Meanwhile, a minor upshift of the corresponding relative wavelength

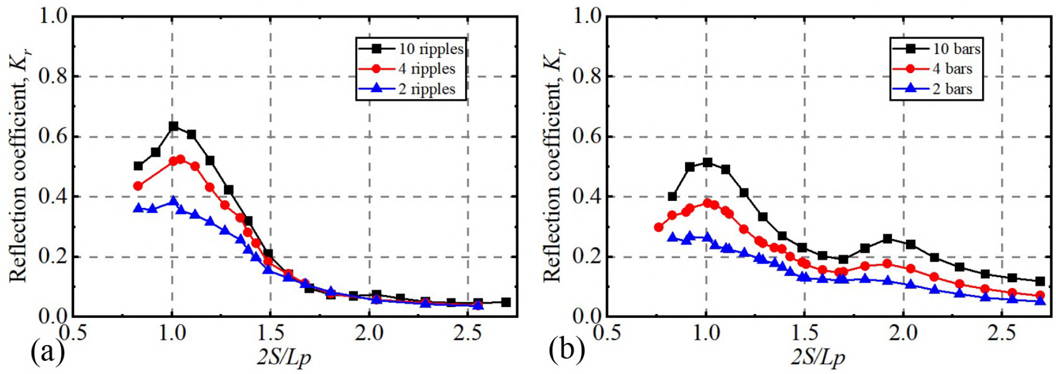

Figure 6.25: Reflection coefficients over seabed with the incident amplitude $a = 0.015$ m, $h_0 = 0.156$ m and frequency range $(0.5 - 3.0)f_p$: (a) ripples and (b) rectified cosinoidal bars.

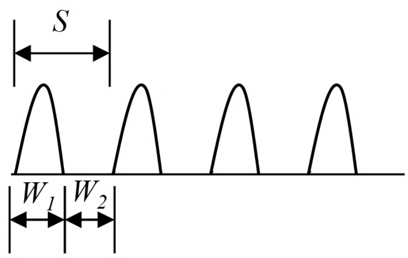

Figure 6.26: Sketch of the width (W_1, W_2) with W_1 being the length of bars and W_2 being the length of flat area.

of the second-order Bragg resonance can be found with the rise in the number of rectified cosinoidal bars.

6.5.3 Influence of the spacing of bars

In previous sections of the Bragg resonance over ripples, the spacing S is set as 1.0 m and the specific width is $W_1 = 0.5$ m, $W_2 = 0.5$ m, as shown in Figure 6.26. This section investigates the reflection coefficients with changes in the spacing and width of rectified cosinoidal bars and steps. Figure 6.27 refers to the cases with $M = 4$ (Case D2) and Figure 6.28 shows the cases with $M = 10$ (Case D3). Three types of combinations of spacing and width of bars are chosen, including the groups with $(W_1 = 0.5, W_2 = 0.5)$, $(W_1 = 0.6, W_2 = 0.4)$ and $(W_1 = 0.5, W_2 = 0.4)$. In terms of Case D2, the peaks in the group with $(W_1 = 0.6, W_2 = 0.4)$ are the highest $K_r = 0.38$ for rectified cosinoidal bars. For the periodic steps, the resonant peak with $(W_1 = 0.6, W_2 = 0.4)$ reaches almost 0.5, which shows a clear increase compared with 0.43 in the case with $(W_1 = 0.5, W_2 = 0.5)$. A relative wavelength upshifting exists for the three combinations of spacing and width of rectified cosinoidal bars. It can be found that the excitation condition of the fundamental Bragg resonance $2S/L_P$ is around 1.0 for cases with $(W_1 = 0.5, W_2 = 0.5)$ and $(W_1 = 0.6, W_2 = 0.4)$, but it becomes 1.1 with $(W_1 = 0.5, W_2 = 0.4)$. For the excitation condition of the second-order Bragg reaction with $(W_1 = 0.6, W_2 = 0.4)$, the condition for rectified cosinoidal bars is $2S/L_P = 1.9$ and $2S/L_P = 1.8$ for steps. A downshift of the dimensionless parameter $2S/L_P$ is found in both types of periodic bars. In addition, the values of $2S/L_P$ for both rectified cosinoidal bars and steps have upshifted to 2.2 with $(W_1 = 0.5, W_2 = 0.4)$.

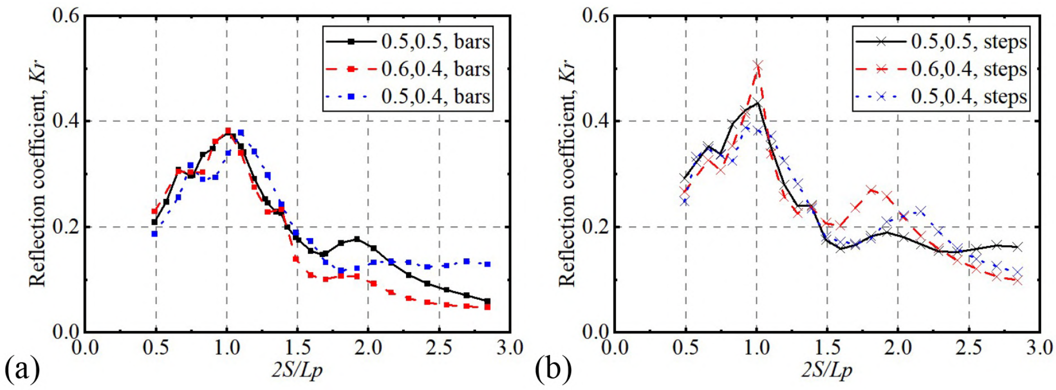

Figure 6.27: Reflection coefficients with different groups of spacing and width with the incident amplitude $a = 0.015$ m and frequency range $(0.5 - 3.0)f_p$: (a) $M = 4$, $h_0 = 0.156$ m, rectified cosinoidal bars and (b) $M = 4$, $h_0 = 0.156$ m, steps.

In terms of deeper h_0 (Case D3) in Figure 6.28, the deviation among the second-

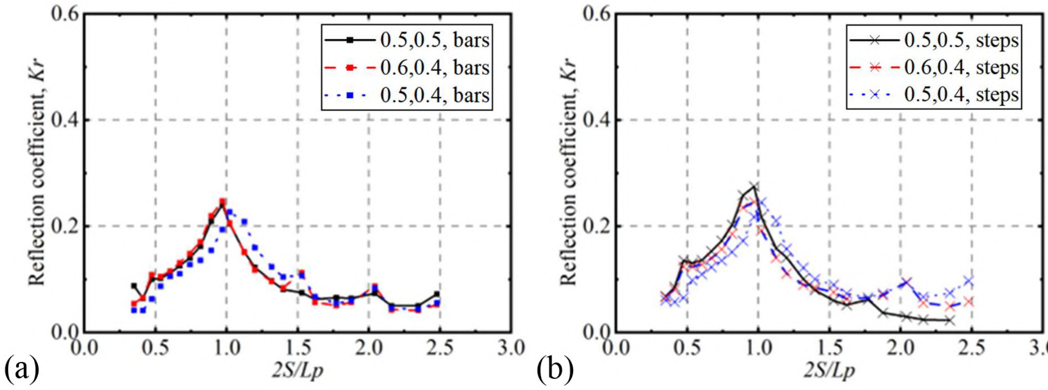

Figure 6.28: Reflection coefficients with different groups of spacing and width with the incident amplitude $a = 0.015$ m and frequency range $(0.5-3.0)f_p$: (a) $M = 10$, $h_0 = 0.313$ m, rectified cosinoidal bars and (b) $M = 10$, $h_0 = 0.313$ m, steps.

order Bragg resonance is negligible. The discrepancies among the three groups are small for 10 rectified cosinoidal bars and steps, respectively. The peak for steps with $(W_1 = 0.5, W_2 = 0.5)$ is the maximum as 0.28. Meanwhile, the second-order Bragg reflection coefficient peaks for the latter two groups are the same. Thus, in a shallower water depth, the variation of width and spacing is demonstrated to significantly influence excitation conditions, especially for the second-order Bragg resonance. The increased water depth h_0 can reduce the difference induced by the variation of spacing and widths.

6.5.4 Influence of the height of seabed

Except for the number and spacing, the height of seabed D is also an important factor influencing the Bragg resonant peaks (Chang and Liou, 2007). Figure 6.29 displays the reflection coefficients with different heights $D = 0.03$ m, $D = 0.05$ m and $D = 0.07$ m for the seabed of ripples, rectified cosinoidal bars and steps with the numbers $M = 4$ (Case D2) and Figure 6.30 shows the results with $M = 10$ (Case

D3). It is found that the cases with $D = 0.07$ m always excite the highest resonant peaks. For Case D3 with ripples, the peaks of the fundamental Bragg resonance increase by about 0.1 with every increment of 0.02 m in height. In addition, the peaks at $2S/L_P = 2.0$ are high in the cases with $D = 0.07$ m. In the cases with rectified cosinoidal bars and steps, the peaks at $2S/L_P = 2.0$ even exceed that of the fundamental Bragg reflection by increasing the height of the seabed. One potential explanation is that the depth changes induce the superharmonics, which are enhanced at the depth transitions (Li et al., 2021c). It also causes higher reflected waves, and hence the superharmonics of the reflected waves also become higher and excite a second-order Bragg resonance. The value of the second-order Bragg reflection may exceed that of the fundamental Bragg reflection. To sum up, the increase in height D effectively increases the Bragg resonant peaks. The shift of the dimensionless parameter $2S/L_P$ is small here.

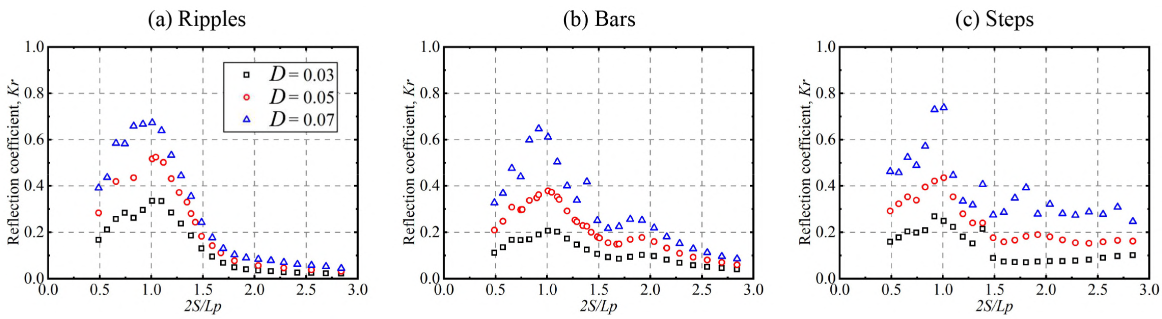

Figure 6.29: Reflection coefficients with different heights for rectified cosinoidal bars and steps with the incident amplitude $a = 0.015$ m and frequency range $(0.5 - 3.0)f_p$, $M = 4$ (Case D2): (a) ripples; (b) bars and (c) steps.

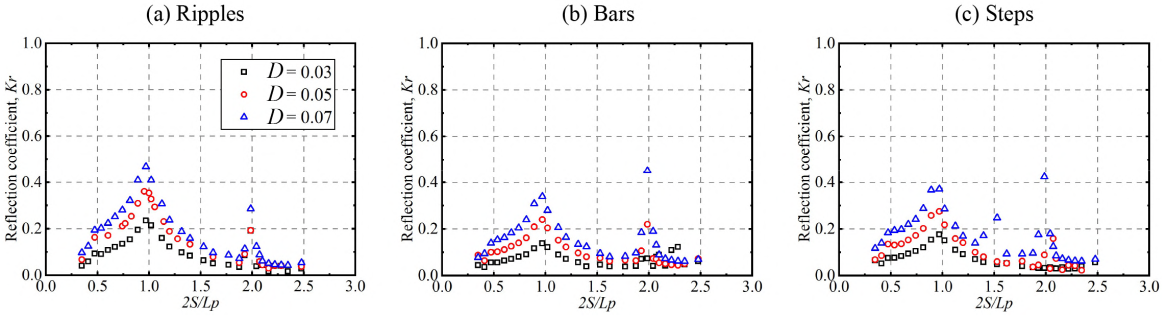

Figure 6.30: Reflection coefficients with different heights for rectified cosinoidal bars and steps with the incident amplitude $a = 0.015$ m and frequency range $(0.5 - 3.0)f_p$, $M = 10$ (Case D3): (a) ripples; (b) bars and (c) steps.

6.6 Conclusions

This chapter employs a fully nonlinear numerical model using the conformal mapping method to investigate wave resonance. The first part discussed the potential wave trapping with the abrupt depth transition. The propagation of trapped waves traveling along a submerged step is investigated numerically. Regular incident waves with the first four trapped frequencies and two normal frequencies are adopted. The surface elevations in spatial and time domains show the first two trapped modes and obvious wave refraction propagating behind the step. Besides, the reflective wave can be strongly influenced by the wave steepness and lead to the generation of superharmonics. The reflection coefficient is used as the reference for the trapped wave amplitude where the simulated results have good agreement with the theoretical ones. Variation of skewness at the trapped frequencies is stronger than that at the normal frequencies. Thus, skewness is more likely to be the reference objective in studying the trapped waves rather than the kurtosis.

The second part considers the nonlinear propagation of focused wave groups over the periodic seabed. The numerical model is well validated by the existing experimental, theoretical and numerical results. Increased amplitudes or wave steepness suppress the peak value of Bragg reflection and upshift the corresponding relative wavelength $2S/L_P$. Moreover, when the focused position is closer to the bars, the peak reflection coefficients are higher, which implies that periodic breakwater locations near the coastline can be optimized to reduce the threat caused by extreme waves more effectively.

Compared with the effects of the incident focused wave groups, the variation of the seabed has a greater influence on the reflection. An increased number of bars is found to achieve a stronger wave reflection, including the fundamental and second-order Bragg resonance. The seabed with ripples contributes to the highest reflection coefficients when $2S/L_P < 1.5$. However, the seabed with steps of the same size results in the highest reflection coefficients if $2S/L_P \geq 1.5$. Adjusting the spacing and width of bars can slightly increase the peak Bragg reflection; however, it causes a downshift of the corresponding relative wavelength of the second-order Bragg resonance, especially when there are only a finite number of bars like $M = 4$. If the number of bars is large, such as 10 rectified cosinoidal bars or steps, there is a little deviation between the reflection induced by different spacing and width. A decrease in the overall spacing weakens the Bragg reflections and upshifts the corresponding relative wavelength. Moreover, the addition of the height of the seabed conspicuously enhances the reflection coefficients. A second-order Bragg reflection might also be induced, and the value may exceed that of the fundamental Bragg reflection. Given the focused wave group is a type of strong nonlinear wave, the generation of the superharmonics in the propagation and the reflection coefficients of superharmonics are important to be considered in further investigation.

Chapter 7

Conclusions and future work

7.1 Conclusions and limitations

The primary objective of this research is to investigate the harmonic generation in the nonlinear wave propagation during varying bathymetries. A fully nonlinear numerical model within the exact Euler equations is developed with the conformal mapping method. The wave elevation and potential on the free surface are updated by the pseudo-spectral method. The nonlinear model simulates the nonlinear interaction between focused wave groups and bathymetry with high efficiency and then facilitates the investigation of the hydrodynamic process. Laboratory experiments are carried out to validate numerical results. Both monochromatic and focused wave group propagation over depth transitions have been taken into consideration in the research, where the subharmonics and superharmonics are decomposed and assessed. For each harmonic component, the investigation of their variation of crests and evolution of kurtosis can provide a more insightful understanding of the extreme wave evolution. Two types of wave resonance, wave trapping and Bragg resonance, are discussed over a submerged step and periodic bottoms, respectively. The excitation conditions of peak reflection during different bathymetries are discussed. Quantifying the role of nonlinearity in this wave scattering or focusing process is decisive for estimating the effects of the associated wave loads on coastal structures and coastlines. The major conclusions of this thesis are summarized as follows:

1). A fully nonlinear numerical model is developed for investigating the nonlinear propagation of focused wave groups and their interactions with complex bathymetries. This nonlinear model provides a more detailed replication of the hydrodynamic process compared to previous numerical models. Furthermore, it requires less computational load and time to solve the potential flow model, which shows high efficiency in solving the nonlinear wave evolution over uneven bottoms. To validate the established model, laboratory experiments were conducted to provide reference data.

2). The nonlinear dynamics of monochromatic waves over a submerged step representing the abrupt depth transitions are investigated both experimentally and numerically. The higher-harmonic wave components are extracted and their corresponding wave profiles in the spatio-temporal domains are displayed. The existence of a submerged step enhances the superharmonic amplitudes at the depth transitions and the shallower regions. In addition, the crests of superharmonics become higher with the increasing wave steepness. Wave scattering with the superharmonics will no longer obey the assumption of the linear theory because the sum of reflection and transmission coefficients is larger than 1. The occurrence of superharmonics triggers higher crests and a stronger asymmetry of wave profiles, resulting in higher peaks of skewness and kurtosis. Hence, it confirms the increased probability of extreme wave occurrence on ADTs.

3). An exploration of the nonlinear focused wave propagation over depth transitions is performed based on the experimental and numerical results. The nonlinear wave-wave interactions result in a downstream shift of focused positions, meanwhile, the shift becomes less when the steepness becomes high. Moreover, except for the wave-wave nonlinearity, the water depth change induces the generation of subharmonics and superharmonics, including the second bound and free waves, which are demonstrated to play a major role in the increased wave nonlinearity at the first and second transitions, respectively. The superposition of bound and free waves causes a sudden drop in the spectra of second harmonics, and conversely, the occurrence of the drop can reflect the presence of free waves. It provides a potential detection for the coexistence of second bound and free waves. The evolution of the skewness and kurtosis demonstrates that the superharmonics influence the high asymmetry of the surface elevation on the upstream junction. The whole influence of higher harmonics enhances the kurtosis in the shallower regions and makes the focused positions of extreme waves shift downstream, thereby increasing the risk in that area.

4). Wave resonance with specific terrain is studied using the fully nonlinear numerical model, which is first validated by theories and experimental data in this field. The trapped waves are assessed at the trapping frequencies obtained from the linear theory, where a clear trapped condition on the first two trapped modes. Compared with kurtosis, the alteration of skewness is informative in studying wave trapping. Effects of the parameters of focused waves and different cross-sections on the resonance peak are examined. The variation in incident focused wave groups has a minor effect on the Bragg reflection compared to that of the bottoms. Three types of periodic bottoms are tested and the corresponding conditions of optimal Bragg resonance are obtained. It could make a contribution to the design of breakwaters for coastal protection. Moreover, a second-order Bragg resonance is discovered on highly nonlinear bathymetries, such as more numbers, specific spacing or larger heights of bottoms. It proposes potential new extreme wave resonance phenomena in coastal engineering and the necessity of improvement of warning in the future.

There are still some limitations of this work. The main limitation is that it is a two-dimensional based model. Three-dimensional effects cannot be considered. Viscous effects due to wave impact or flow separation are not modeled. The fully nonlinear numerical model can simulate the nonlinear wave propagation over different bottoms, but it is unable to simulate the cases with local breaking. In addition, the length of the laboratory tank may be insufficient to capture the entire hydrodynamic performance of wave nonlinearity.

7.2 Future work

The work that needs to be continued in this research is introduced in this section. It mainly focuses on the probability of occurrence of extreme waves in deep-to-intermediate water areas and the effects of the continual water depth changes on the nonlinear wave propagation. Several suggestions for future research are provided:

1). ***Establishment of three-dimensional fully nonlinear numerical model using conformal coordinates***

The three-dimensional potential theory for the surface water waves in varying bathymetries should be considered in future work. The conformal coordinates in complicated domains need to be developed to obtain more accurate results. Meanwhile, it is essential to conduct further validation of the fully nonlinear numerical model, despite the similarity in simulation methods. The forking angles and generalized compatibility condition at nodes may impact the results when studying nonlinear water waves on graphs.

2). ***Statistical analysis of extreme waves generated by abrupt depth transitions***

Future work should focus on conducting a comprehensive statistical analysis of extreme waves generated by abrupt depth changes. This would involve collecting extensive data on wave patterns in areas with sudden depth changes and using advanced statistical methods to analyze this data. The goal would be to determine the exact probability of extreme wave occurrence in these areas, which could significantly improve marine safety and ocean development projects.

3). ***Investigation of the effects of artificial breakwater on coastal protection***

Although the impact of periodic steps on extreme wave occurrence has been investigated, there is a lack of research on the influence of alternative breakwater types, such as periodic trenches and floating steps, in mitigating extreme waves.

Future work should concentrate on understanding the breakwater's role in attenuating extreme wave events. This would involve conducting both laboratory and field experiments, as well as developing new mathematical models to forecast the reduced probability of extreme wave occurrences with varying types of breakwaters.

4). ***Nonlinear Bragg resonance of focused wave groups over periodic bottoms***

It is known that a certain ratio of the wavelength of surface waves and that of the bottoms induce the resonance, meanwhile, the higher-order Bragg resonance in the nonlinear freak waves propagation offshore is also possible. The excitation conditions of higher-order Bragg resonance changes due to the enhanced wave nonlinearity, which means the excitation frequency shift needs to be further investigated. The high nonlinearity could induce the complex wave scattering, hence possible multiple Bragg resonance. This thesis work has verified the second-order Bragg resonance of focused wave groups, but further investigation on the resonance peaks of extreme waves is necessary.

References

Abbasnia, A., Ghiasi, M., and Abbasnia, A. H. (2017). "Irregular wave transmission on bottom bumps using fully nonlinear NURBS numerical wave tank". *Engineering Analysis with Boundary Elements* 82, pp. 130–140.

Abroug, I., Abcha, N., Dutykh, D., Jarno, A., and Marin, F. (2020). "Experimental and numerical study of the propagation of focused wave groups in the nearshore zone". *Physics Letters A* 384.6, p. 126144.

Airy, G. B. (1845). *Tides and waves*. B. Fellowes.

Andersen, T. L., Eldrup, M. R., and Frigaard, P. (2017). "Estimation of incident and reflected components in highly nonlinear regular waves". *Coastal Engineering* 119, pp. 51–64.

Ardhuin, F. and Herbers, T. (2002). "Bragg scattering of random surface gravity waves by irregular seabed topography". *Journal of Fluid Mechanics* 451, pp. 1–33.

Baldock, T., Swan, C., and Taylor, P. (1996). "A laboratory study of nonlinear surface waves on water". *Philosophical Transactions of the Royal Society of London. Series A: Mathematical, Physical and Engineering Sciences* 354.1707, pp. 649–676.

Banks, M. and Abdussamie, N. (2017). “The response of a semisubmersible model under focused wave groups: Experimental investigation”. *Journal of Ocean Engineering and Science* 2.3, pp. 161–171.

Belibassakis, K. and Athanassoulis, G. (2011). “A coupled-mode system with application to nonlinear water waves propagating in finite water depth and in variable bathymetry regions”. *Coastal Engineering* 58.4, pp. 337–350.

Belzons, M., Rey, V., and Guazzelli, E. (1991). “Subharmonic Bragg resonance for surface water waves”. *Europhysics Letters* 16.2, p. 189.

Bihs, H., Chella, M. A., Kamath, A., and Arntsen, Ø. A. (2017). “Numerical investigation of focused waves and their interaction with a vertical cylinder using REEF3D”. *Journal of Offshore Mechanics and Arctic Engineering* 139.4, p. 041101.

Bingham, H. B., Madsen, P. A., and Fuhrman, D. R. (2009). “Velocity potential formulations of highly accurate Boussinesq-type models”. *Coastal Engineering* 56.4, pp. 467–478.

Bolles, C. T., Speer, K., and Moore, M. (2019). “Anomalous wave statistics induced by abrupt depth change”. *Physical review fluids* 4.1, p. 011801.

Borthwick, A. G., Hunt, A. C., Feng, T., Taylor, P. H., and Stansby, P. K. (2006). “Flow kinematics of focused wave groups on a plane beach in the UK Coastal Research Facility”. *Coastal Engineering* 53.12, pp. 1033–1044.

Boudjelal, S., Fourar, A., and Massouh, F. (2022). “Experimental and numerical simulation of free surface flow over an obstacle on a sloped channel”. *Modeling Earth Systems and Environment*, pp. 1–9.

Brossard, J., Perret, G., Blonce, L., and Diedhiou, A. (2009). “Higher harmonics induced by a submerged horizontal plate and a submerged rectangular step in a wave flume”. *Coastal engineering* 56.1, pp. 11–22.

Camassa, R. and Wu, T. Y.-t. (1991). “Stability of forced steady solitary waves”. *Philosophical Transactions of the Royal Society of London. Series A: Physical and Engineering Sciences* 337.1648, pp. 429–466.

Chang, H.-K. and Liou, J.-C. (2007). “Long wave reflection from submerged trapezoidal breakwaters”. *Ocean Engineering* 34.1, pp. 185–191.

Chen, L., Zang, J., Hillis, A. J., Morgan, G. C., and Plummer, A. R. (2014). “Numerical investigation of wave–structure interaction using OpenFOAM”. *Ocean Engineering* 88, pp. 91–109.

Chen, Q., Zang, J., Ning, D., Blenkinsopp, C., and Gao, J. (2019). “A 3D parallel particle-in-cell solver for extreme wave interaction with floating bodies”. *Ocean Engineering* 179, pp. 1–12.

Cheng, Y., Ji, C., Zhai, G., and Oleg, G. (2017). “Fully nonlinear numerical investigation on hydroelastic responses of floating elastic plate over variable depth sea-bottom”. *Marine Structures* 55, pp. 37–61.

Cheng, Y., Li, G., Ji, C., Fan, T., and Zhai, G. (2020). “Fully nonlinear investigations on performance of an OWSC (oscillating wave surge converter) in 3D (three-dimensional) open water”. *Energy* 210, p. 118526.

Choi, W. and Camassa, R. (1999). “Exact evolution equations for surface waves”. *Journal of Engineering Mechanics* 125.7, pp. 756–760.

Choi, Y., Bouscasse, B., Seng, S., Ducrozet, G., Gentaz, L., and Ferrant, P. (2018). "Generation of regular and irregular waves in Navier-Stokes CFD solvers by matching with the nonlinear potential wave solution at the boundaries". *International Conference on Offshore Mechanics and Arctic Engineering*. Vol. 51210. American Society of Mechanical Engineers, V002T08A020.

Chow, A. D., Stansby, P. K., Rogers, B. D., Lind, S. J., and Fang, Q. (2022). "Focused wave interaction with a partially-immersed rectangular box using 2-D incompressible SPH on a GPU comparing with experiment and linear theory". *European Journal of Mechanics-B/Fluids* 95, pp. 252–275.

Christou, M., Swan, C., and Gudmestad, O. (2008). "The interaction of surface water waves with submerged breakwaters". *Coastal Engineering* 55.12, pp. 945–958.

Cokelet, E. (1977). "Steep gravity waves in water of arbitrary uniform depth". *Philosophical Transactions of the Royal Society of London. Series A, Mathematical and Physical Sciences* 286.1335, pp. 183–230.

Cruz, E. C., Isobe, M., and Watanabe, A. (1993). "Nonlinear wave transformation over a submerged permeable breakwater". *Coastal Engineering 1992*, pp. 1101–1114.

Davies, A. and Heathershaw, A. (1984). "Surface-wave propagation over sinusoidally varying topography". *Journal of Fluid Mechanics* 144, pp. 419–443.

Didenkulova, E., Didenkulova, I., and Medvedev, I. (2022). "Freak wave events in 2005–2021: statistics and analysis of favourable wave and wind conditions". *Natural Hazards and Earth System Sciences Discussions* 2022, pp. 1–17.

Didenkulova, E., Didenkulova, I., and Medvedev, I. (2023). “Freak wave events in 2005–2021: statistics and analysis of favourable wave and wind conditions”. *Natural Hazards and Earth System Sciences* 23.4, pp. 1653–1663.

Djordjevié, V. D. and Redekopp, L. G. (1978). “On the development of packets of surface gravity waves moving over an uneven bottom”. *Zeitschrift für angewandte Mathematik und Physik ZAMP* 29, pp. 950–962.

Draycott, S., Li, Y., Stansby, P., Adcock, T., and Bremer, T. van den (2022). “Harmonic-induced wave breaking due to abrupt depth transitions: An experimental and numerical study”. *Coastal Engineering* 171, p. 104041.

Ducrozet, G. and Gouin, M. (2017). “Influence of varying bathymetry in rogue wave occurrence within unidirectional and directional sea-states”. *Journal of Ocean Engineering and Marine Energy* 3, pp. 309–324.

Dyachenko, A. I., Kuznetsov, E. A., Spector, M., and Zakharov, V. E. (1996). “Analytical description of the free surface dynamics of an ideal fluid (canonical formalism and conformal mapping)”. *Physics Letters A* 221.1-2, pp. 73–79.

Eroğlu, N. and Taştan, K. (2020). “Local Energy Losses for Wave-Type Flows at Abrupt Bottom Changes”. *Journal of Irrigation and Drainage Engineering* 146.9, p. 04020029.

Feng, X. (2019). “Analysis of higher harmonics in a focused water wave group by a nonlinear potential flow model”. *Ocean Engineering* 193, p. 106581.

Fern ’andez, H., Sriram, V., Schimmels, S., and Oumeraci, H. (2014). “Extreme wave generation using self correcting method—Revisited”. *Coastal Engineering* 93, pp. 15–31.

Galan, A., Simarro, G., Orfila, A., Simarro, J., and Liu, P.-F. (2012). “Fully nonlinear model for water wave propagation from deep to shallow waters”. *Journal of Waterway, Port, Coastal, and Ocean Engineering* 138.5, pp. 362–371.

Gao, J.-l., Lyu, J., Zhang, J., and Zang, J. (2023). “Influences of floater motion on gap resonance triggered by focused wave groups”. *China Ocean Engineering* 37.4, pp. 685–697.

Gao, J., Ma, X., Dong, G., Chen, H., Liu, Q., and Zang, J. (2021). “Investigation on the effects of Bragg reflection on harbor oscillations”. *Coastal Engineering* 170, p. 103977.

Geng, T., Liu, H., and Dias, F. (2021). “Solitary-wave loads on a three-dimensional submerged horizontal plate: Numerical computations and comparison with experiments”. *Physics of Fluids* 33.3.

Giniyatullin, A., Kurkin, A., Semin, S., and Stepanyants, Y. A. (2014). “Transformation of narrowband wavetrains of surface gravity waves passing over a bottom step”. *Mathematical Modelling of Natural Phenomena* 9.5, pp. 73–82.

Goda, Y. and Suzuki, T. (1976). “Estimation of incident and reflected waves in random wave experiments”. *Coastal Engineering Proceedings* 1.15, p. 47.

Gouin, M., Ducrozet, G., and Ferrant, P. (2016). “Development and validation of a non-linear spectral model for water waves over variable depth”. *European Journal of Mechanics-B/Fluids* 57, pp. 115–128.

Gramstad, O., Zeng, H., Trulsen, K., and Pedersen, G. (2013). “Freak waves in weakly nonlinear unidirectional wave trains over a sloping bottom in shallow water”. *Physics of Fluids* 25.12.

Gu, G. Z. and Wang, H. (1993). “Numerical modeling for wave energy dissipation within porous submerged breakwaters of irregular cross section”. *Coastal Engineering 1992*, pp. 1189–1202.

Guo, F. C., Liu, H. W., and Pan, J. J. (2021). “Phase downshift or upshift of Bragg resonance for water wave reflection by an array of cycloidal bars or trenches”. *Wave Motion* 106, p. 102794.

Gutiérrez, E. M. (2017). “Experimental study of water waves: nonlinear effects and absorption”. PhD thesis. Université Pierre & Marie Curie-Paris 6.

Hsu, T. W., Hsiao, S. C., Ou, S. H., Wang, S. K., Yang, B. D., and Chou, S. E. (2007). “An application of Boussinesq equations to Bragg reflection of irregular waves”. *Ocean engineering* 34.5-6, pp. 870–883.

Hsu, T. W., Tsai, L. H., and Huang, Y. T. (2003). “Bragg scattering of water waves by multiply composite artificial bars”. *Coastal Engineering Journal* 45.02, pp. 235–253.

Hu, J., Zhou, B., Vogel, C., Liu, P., Willden, R., Sun, K., Zang, J., Geng, J., Jin, P., Cui, L., et al. (2020). “Optimal design and performance analysis of a hybrid system combing a floating wind platform and wave energy converters”. *Applied energy* 269, p. 114998.

Janssen, P. A. (2003). “Nonlinear four-wave interactions and freak waves”. *Journal of Physical Oceanography* 33.4, pp. 863–884.

Jeon, C. H. and Cho, Y. S. (2006). “Bragg reflection of sinusoidal waves due to trapezoidal submerged breakwaters”. *Ocean Engineering* 33.14-15, pp. 2067–2082.

Ji, Q., Dong, S., Luo, X., and Soares, C. G. (2017). “Wave transformation over submerged breakwaters by the constrained interpolation profile method”. *Ocean Engineering* 136, pp. 294–303.

Judge, F. M., Hunt-Raby, A. C., Orszaghova, J., Taylor, P. H., and Borthwick, A. G. (2019). “Multi-directional focused wave group interactions with a plane beach”. *Coastal Engineering* 152, p. 103531.

Kharif, C. and Pelinovsky, E. (2003). “Physical mechanisms of the rogue wave phenomenon”. *European Journal of Mechanics-B/Fluids* 22.6, pp. 603–634.

Kharif, C. and Pelinovsky, E. (2006). *Freak waves phenomenon: physical mechanisms and modelling*. Springer Vienna, pp. 107–172.

Kirby, J. T. and Anton, J. P. (1990). “Bragg reflection of waves by artificial bars”. *Coastal Engineering 1990*, pp. 757–768.

Ko, H. S. and Lynett, P. J. (2019). “A study of long wave run-ups on a bi-linear beach slope induced by solitary and transient-focused wave group”. *Coastal Engineering Journal* 61.2, pp. 135–151.

Kobayashi, N. and Wurjanto, A. (1989). “Wave transmission over submerged breakwaters”. *Journal of waterway, port, coastal, and ocean engineering* 115.5, pp. 662–680.

Koshimura, S. I., Imamura, F., and Shuto, N. (2001). “Characteristics of tsunamis propagating over oceanic ridges: Numerical simulation of the 1996 Irian Jaya earthquake tsunami”. *Natural Hazards* 24, pp. 213–229.

Kowalik, Z., Horrillo, J., Knight, W., and Logan, T. (2008). “Kuril Islands tsunami of November 2006: 1. Impact at Crescent City by distant scattering”. *Journal of Geophysical Research: Oceans* 113.C1.

Kurkin, A., Semin, S., and Stepanyants, Y. A. (2015). “Transformation of surface waves over a bottom step”. *Izvestiya, Atmospheric and Oceanic Physics* 51.2, pp. 214–223.

Kway, J. H., Loh, Y. S., and Chan, E. S. (1998). “Laboratory study of deep-water breaking waves”. *Ocean Engineering* 25.8, pp. 657–676.

Lakshmanan, M. (2007). “Integrable nonlinear wave equations and possible connections to tsunami dynamics”. *Tsunami and nonlinear waves*. Springer, pp. 31–49.

Latifah, A. L., Handri, D., Shabrina, A., Hariyanto, H., and Groesen, E. van (2021). “Statistics of Simulated Storm Waves over Bathymetry”. *Journal of Marine Science and Engineering* 9.7, p. 784.

Lawrence, C., Gramstad, O., and Trulsen, K. (2021). “Variational Boussinesq model for kinematics calculation of surface gravity waves over bathymetry”. *Wave Motion* 100, p. 102665.

Lee, C., Kim, G., and Suh, K. D. (2003). “Extended mild-slope equation for random waves”. *Coastal Engineering* 48.4, pp. 277–287.

Lee, J.-F., Tu, L.-F., and Liu, C.-C. (2014). “Nonlinear wave evolution above rectangular submerged structures”. *Journal of Marine Science and Technology* 22.5, p. 1.

Li, J., Wang, Z., and Liu, S. (2014). “Experimental study of interactions between multi-directional focused wave and vertical circular cylinder, part II: Wave force”. *Coastal engineering* 83, pp. 233–242.

Li, Y. and Chabchoub, A. (2023). “On the formation of coastal rogue waves in water of variable depth”. *Cambridge Prisms: Coastal Futures* 1, e33.

Li, Y., Draycott, S., Adcock, T. A., and Bremer, T. S. van den (2021a). “Surface wavepackets subject to an abrupt depth change. Part 2. Experimental analysis”. *Journal of Fluid Mechanics* 915, A72.

Li, Y., Draycott, S., Zheng, Y., Lin, Z., Adcock, T. A., and Bremer, T. S. van den (2021b). “Why rogue waves occur atop abrupt depth transitions”. *Journal of Fluid Mechanics* 919, R5.

Li, Y., Zheng, Y., Lin, Z., Adcock, T. A., and Bremer, T. S. van den (2021c). “Surface wavepackets subject to an abrupt depth change. Part 1. Second-order theory”. *Journal of Fluid Mechanics* 915, A71.

Likhachev, V., Shevaleevskii, O., and Vinogradov, G. (2015). “Quantum dynamics of charge transfer on the one-dimensional lattice: Wave packet spreading and recurrence”. *Chinese Physics B* 25.1, p. 018708.

Lin, C. Y. and Huang, C. J. (2004). “Decomposition of incident and reflected higher harmonic waves using four wave gauges”. *Coastal Engineering* 51.5, pp. 395–406.

Lippmann, T. and Holman, R. (1990). “The spatial and temporal variability of sand bar morphology”. *Journal of Geophysical Research: Oceans* 95.C7, pp. 11575–11590.

Liu, H. F., Bi, C. W., and Zhao, Y. P. (2020). “Experimental and numerical study of the hydrodynamic characteristics of a semisubmersible aquaculture facility in waves”. *Ocean Engineering* 214, p. 107714.

Liu, H. W. (2023). “An approximate law of Class I Bragg resonance of linear shallow-water waves excited by five types of artificial bars”. *Ocean Engineering* 267, p. 113245.

Liu, H. W., Liu, Y., and Lin, P. z. (2019a). “Bloch band gap of shallow-water waves over infinite arrays of parabolic bars and rectified cosinoidal bars and Bragg resonance over finite arrays of bars”. *Ocean Engineering* 188, p. 106235.

Liu, H. W., Shi, Y. P., and Cao, D. Q. (2015). “Optimization of parabolic bars for maximum Bragg resonant reflection of long waves”. *Journal of Hydrodynamics* 27.3, pp. 373–382.

Liu, H., Fu, D., and Sun, X. (2013). “Analytic solution to the modified mild-slope equation for reflection by a rectangular breakwater with scour trenches”. *Journal of Engineering Mechanics* 139.1, pp. 39–58.

Liu, W., Liu, Y., and Zhao, X. (2019b). “Numerical study of Bragg reflection of regular water waves over fringing reefs based on a Boussinesq model”. *Ocean Engineering* 190, p. 106415.

Liu, Y., Li, H. J., and Zhu, L. (2016). “Bragg reflection of water waves by multiple submerged semi-circular breakwaters”. *Applied Ocean Research* 56, pp. 67–78.

Long, J. W. and Özkan-Haller, H. T. (2005). “Offshore controls on nearshore rip currents”. *Journal of geophysical research: oceans* 110.C12.

Loukili, M., Dutykh, D., Pincemin, S., Kotrasova, K., and Abcha, N. (2022). "Theoretical investigation applied to scattering water waves by rectangular submerged obstacles/and submarine trenches". *Geosciences* 12.10, p. 379.

Luo, L., Liu, S., Li, J., and Jia, W. (2019). "Numerical simulation of oblique and multidirectional wave propagation and breaking on steep slope based on FEM model of Boussinesq equations". *Applied Mathematical Modelling* 71, pp. 632–655.

Lynett, P. J., Melby, J. A., and Kim, D. H. (2010). "An application of Boussinesq modeling to hurricane wave overtopping and inundation". *Ocean Engineering* 37.1, pp. 135–153.

MacMahan, J. H., Thornton, E. B., and Reniers, A. J. (2006). "Rip current review". *Coastal engineering* 53.2-3, pp. 191–208.

Madsen, P. A., Fuhrman, D. R., and Schäffer, H. A. (2008). "On the solitary wave paradigm for tsunamis". *Journal of Geophysical Research: Oceans* 113.C12.

Madsen, P. A., Fuhrman, D. R., and Wang, B. (2006). "A Boussinesq-type method for fully nonlinear waves interacting with a rapidly varying bathymetry". *Coastal engineering* 53.5-6, pp. 487–504.

Majda, A. J., Moore, M., and Qi, D. (2019). "Statistical dynamical model to predict extreme events and anomalous features in shallow water waves with abrupt depth change". *Proceedings of the National Academy of Sciences* 116.10, pp. 3982–3987.

Mandelbrot, B. B. and Wallis, J. R. (1969). “Robustness of the rescaled range R/S in the measurement of noncyclic long run statistical dependence”. *Water resources research* 5.5, pp. 967–988.

Massel, S. (1983). “Harmonic generation by waves propagating over a submerged step”. *Coastal Engineering* 7.4, pp. 357–380.

Mei, C. C. and Unluata, U. (1972). “Harmonic generation in shallow water waves.” *Waves on Beaches and Resulting Sediment Transport*, pp. 181–202.

Mei, C. C., Stiassnie, M. A., and Yue, D. K. P. (2005). *Theory and Applications of Ocean Surface Waves: Part 1: Linear Aspects*. World Scientific.

Miles, J. W. (1981). “Oblique surface-wave diffraction by a cylindrical obstacle”. *Dynamics of Atmospheres and Oceans* 6.2, pp. 121–123.

Moideen, R. and Behera, M. R. (2021). “Numerical investigation of extreme wave impact on coastal bridge deck using focused waves”. *Ocean Engineering* 234, p. 109227.

Mondal, R. and Takagi, K. (2019). “Wave scattering by a fixed submerged platform over a step bottom”. *Proceedings of the Institution of Mechanical Engineers, Part M: Journal of Engineering for the Maritime Environment* 233.1, pp. 93–107.

Moore, N. J., Bolles, C. T., Majda, A. J., and Qi, D. (2020). “Anomalous waves triggered by abrupt depth changes: Laboratory experiments and truncated KdV statistical mechanics”. *Journal of Nonlinear Science* 30, pp. 3235–3263.

Morim, J., Wahl, T., Vitousek, S., Santamaria-Aguilar, S., Young, I., and Hemer, M. (2023). “Understanding uncertainties in contemporary and future extreme wave events for broad-scale impact and adaptation planning”. *Science Advances* 9.2, eade3170.

Neetu, S., Suresh, I., Shankar, R., Nagarajan, B., Sharma, R., Shenoi, S., Unnikrishnan, A., and Sundar, D. (2011). “Trapped waves of the 27 November 1945 Makran tsunami: observations and numerical modeling”. *Natural Hazards* 59, pp. 1609–1618.

Ning, D., Liang, C., Chen, L., and Zhang, C. (2022a). “Numerical investigation on the propagation and evolution of focused waves over a sloping bed”. *Ocean Engineering* 250, p. 111035.

Ning, D., Zhang, S., Chen, L., Liu, H., and Teng, B. (2022b). “Nonlinear Bragg scattering of surface waves over a two-dimensional periodic structure”. *Journal of Fluid Mechanics* 946, A25.

Orszaghova, J., Taylor, P. H., Borthwick, A. G., and Raby, A. C. (2014). “Importance of second-order wave generation for focused wave group run-up and overtopping”. *Coastal Engineering* 94, pp. 63–79.

Ou, S. H., Liau, J. M., Hsu, T. W., and Tzang, S. Y. (2002). “Simulating typhoon waves by SWAN wave model in coastal waters of Taiwan”. *Ocean Engineering* 29.8, pp. 947–971.

Pelinovsky, E., Shurgalina, E., and Rodin, A. (2015). “Criteria for the transition from a breaking bore to an undular bore”. *Izvestiya, Atmospheric and Oceanic Physics* 51, pp. 530–533.

Peng, J., Tao, A., Fan, J., Zheng, J., and Liu, Y. (2022). “On the downshift of wave frequency for Bragg resonance”. *China Ocean Engineering* 36.1, pp. 76–85.

Peng, J., Tao, A., Liu, Y., Zheng, J., Zhang, J., and Wang, R. (2019). “A laboratory study of class III Bragg resonance of gravity surface waves by periodic beds”. *Physics of Fluids* 31.6.

Rainey, R. and Longuet-Higgins, M. S. (2006). “A close one-term approximation to the highest Stokes wave on deep water”. *Ocean engineering* 33.14-15, pp. 2012–2024.

Ransley, E., Yan, S., Brown, S., Hann, M., Graham, D., Windt, C., Schmitt, P., Davidson, J., Ringwood, J., Musiedlak, P.-H., et al. (2020). “A blind comparative study of focused wave interactions with floating structures (CCP-WSI Blind Test Series 3)”. *International Journal of Offshore and Polar Engineering* 30.01, pp. 1–10.

Ransley, E. J., Brown, S. A., Hann, M., Greaves, D. M., Windt, C., Ringwood, J., Davidson, J., Schmitt, P., Yan, S., Wang, J. X., et al. (2021). “Focused wave interactions with floating structures: A blind comparative study”. *Proceedings of the Institution of Civil Engineers-Engineering and Computational Mechanics* 174.1, pp. 46–61.

Rapp, R. J. and Melville, W. K. (1990). “Laboratory measurements of deep-water breaking waves”. *Philosophical Transactions of the Royal Society of London. Series A, Mathematical and Physical Sciences* 331.1622, pp. 735–800.

Rey, V., Belzons, M., and Guazzelli, E. (1992). “Propagation of surface gravity waves over a rectangular submerged bar”. *Journal of Fluid Mechanics* 235, pp. 453–479.

Rodrigo, B., Torres-Freyermuth, A., and López-González, J. (2021). “Physical and numerical modeling of focused wave interactions with a low mound breakwater.”

Salonen, N. and Rautenbach, C. (2021). “Toward nearshore, bathymetry induced wave amplification in False Bay, South Africa”. *AIP Advances* 11.7.

Satsuma, J. and Yajima, N. (1974). “B. Initial value problems of one-dimensional self-modulation of nonlinear waves in dispersive media”. *Progress of Theoretical Physics Supplement* 55, pp. 284–306.

Schmitt, P., Doherty, K., Clabby, D., and Whittaker, T. (2012). “The opportunities and limitations of using CFD in the development of wave energy converters”. *Marine & Offshore Renewable Energy*, pp. 89–97.

Shabat, A. and Zakharov, V. (1972). “Exact theory of two-dimensional self-focusing and one-dimensional self-modulation of waves in nonlinear media”. *Sov. Phys. JETP* 34.1, p. 62.

Sriram, V., Schlurmann, T., and Schimmels, S. (2015). “Focused wave evolution using linear and second order wavemaker theory”. *Applied Ocean Research* 53, pp. 279–296.

Stamos, D. G., Hajj, M. R., and Telionis, D. P. (2003). “Performance of hemi-cylindrical and rectangular submerged breakwaters”. *Ocean Engineering* 30.6, pp. 813–828.

Suh, K. D., Lee, C., and Park, W. S. (1997). “Time-dependent equations for wave propagation on rapidly varying topography”. *Coastal Engineering* 32.2-3, pp. 91–117.

Sun, Y. and Zhang, X. (2017). “A second order analytical solution of focused wave group interacting with a vertical wall”. *International Journal of Naval Architecture and Ocean Engineering* 9.2, pp. 160–176.

Synolakis, C. E. (1987). “The runup of solitary waves”. *Journal of Fluid Mechanics* 185, pp. 523–545.

Tang, T., Moss, C., Draycott, S., Bingham, H. B., Van Den Bremer, T. S., Li, Y., and Adcock, T. A. (2023). “The influence of directional spreading on rogue waves triggered by abrupt depth transitions”. *Journal of Fluid Mechanics* 972, R2.

Taylor, M. J., Pendleton Jr, W., Clark, S., Takahashi, H., Gobbi, D., and Goldberg, R. (1997). “Image measurements of short-period gravity waves at equatorial latitudes”. *Journal of Geophysical Research: Atmospheres* 102.D22, pp. 26283–26299.

Teutsch, I., Weisse, R., Moeller, J., and Krueger, O. (2020). “A statistical analysis of rogue waves in the southern North Sea”. *Natural hazards and earth system sciences* 20.10, pp. 2665–2680.

Trulsen, K. (2018). “Rogue waves in the ocean, the role of modulational instability, and abrupt changes of environmental conditions that can provoke non equilibrium wave dynamics”. *The Ocean in Motion*. Springer, pp. 239–247.

Trulsen, K., Raustøl, A., Jorde, S., and Rye, L. B. (2020). “Extreme wave statistics of long-crested irregular waves over a shoal”. *Journal of Fluid Mechanics* 882, R2.

Trulsen, K., Zeng, H., and Gramstad, O. (2012). “Laboratory evidence of freak waves provoked by non-uniform bathymetry”. *Physics of Fluids* 24.9, p. 097101.

Tsai, L. H., Kuo, Y. S., Lan, Y. J., Hsu, T. W., and Chen, W. J. (2011). “Investigation of multiply composite artificial bars for Bragg scattering of water waves”. *Coastal Engineering Journal* 53.04, pp. 521–548.

Ursell, F. (1951). “Trapping modes in the theory of surface waves”. *Mathematical Proceedings of the Cambridge Philosophical Society*. Vol. 47. 2. Cambridge University Press, pp. 347–358.

Viotti, C. and Dias, F. (2014). “Extreme waves induced by strong depth transitions: Fully nonlinear results”. *Physics of Fluids* 26.5, p. 051705.

Viotti, C., Dutykh, D., and Dias, F. (2014). “The conformal-mapping method for surface gravity waves in the presence of variable bathymetry and mean current”. *Procedia IUTAM* 11, pp. 110–118.

Wang, G., Liang, Q., Shi, F., and Zheng, J. (2021). “Analytical and numerical investigation of trapped ocean waves along a submerged ridge”. *Journal of Fluid Mechanics* 915, A54.

Wang, L., Li, J. X., Liu, S. X., and Fan, Y. P. (2020a). “Experimental and numerical studies on the focused waves generated by double wave groups”. *Frontiers in Energy Research* 8, p. 133.

Wang, W., Kamath, A., Martin, T., Pákozdi, C., and Bihs, H. (2020b). “A comparison of different wave modelling techniques in an open-source hydrodynamic framework”. *Journal of Marine Science and Engineering* 8.7, p. 526.

Wang, Y., Peng, J., Sun, H., and Li, G. (2003). “Separation of composite waves by an analytical method”. *Ocean Engineering* 21.1, pp. 42–46.

Westphalen, J., Greaves, D., Williams, C., Hunt-Raby, A., and Zang, J. (2012). “Focused waves and wave–structure interaction in a numerical wave tank”. *Ocean engineering* 45, pp. 9–21.

Wu, Q., Feng, X., Dong, Y., and Dias, F. (2023). “On the behavior of higher harmonics in the evolution of nonlinear water waves in the presence of abrupt depth transitions”. *Physics of Fluids* 35.12.

Xiang, T. and Istrati, D. (2021). “Assessment of extreme wave impact on coastal decks with different geometries via the arbitrary Lagrangian-Eulerian method”. *Journal of Marine Science and Engineering* 9.12, p. 1342.

Xie, J. J. and Liu, H. W. (2023). “Analytical study of Bragg resonances by a finite periodic array of congruent trapezoidal bars or trenches on a sloping seabed”. *Applied Mathematical Modelling* 119, pp. 717–735.

Xu, J., Chen, L., Ning, D., and Zhao, M. (2023). “Resonance of water waves propagating over a uniform and a graded line array of rectified submerged cosinoidal bars”. *Applied Ocean Research* 134, p. 103531.

Yang, Y., Zheng, Y., Ge, H., and Wang, C. (2023). “Nonlinear interactions between solitary waves and structures in a steady current”. *Ocean Engineering* 274, p. 113920.

Yuan, P., Zhu, D., and Dong, Y. (2021). “Spatial failure mechanism of coastal bridges under extreme waves using high-efficient pseudo-fluid-structure interaction solution scheme”. *Ocean Engineering* 240, p. 109894.

Yuen, H. C. and Lake, B. M. (1980). “Instabilities of waves on deep water”. *Annual Review of Fluid Mechanics* 12.1, pp. 303–334.

Zeng, F., Zhang, N., Huang, G., Gu, Q., and Pan, W. (2022). “A novel method in generating freak wave and modulating wave profile”. *Marine Structures* 82, p. 103148.

Zeng, H., Qin, B., and Zhang, J. (2017). “Optimal collocation of Bragg breakwaters with rectangular bars on sloping seabed for Bragg resonant reflection by long waves”. *Ocean Engineering* 130, pp. 156–165.

Zhang, H., Tao, A., Tu, J., Su, J., and Xie, S. (2021a). “The focusing waves induced by Bragg resonance with V-shaped undulating bottom”. *Journal of Marine Science and Engineering* 9.7, p. 708.

Zhang, J. and Benoit, M. (2021). “Wave–bottom interaction and extreme wave statistics due to shoaling and de-shoaling of irregular long-crested wave trains over steep seabed changes”. *Journal of Fluid Mechanics* 912, A28.

Zhang, J., Benoit, M., Kimmoun, O., Chabchoub, A., and Hsu, H.-C. (2019). “Statistics of extreme waves in coastal waters: large scale experiments and advanced numerical simulations”. *Fluids* 4.2, p. 99.

Zhang, J., Benoit, M., and Ma, Y. (2022). “Equilibration process of out-of-equilibrium sea-states induced by strong depth variation: Evolution of coastal wave spectrum and representative parameters”. *Coastal Engineering* 174, p. 104099.

Zhang, J., Ma, Y., Tan, T., Dong, G., and Benoit, M. (2023a). “Enhanced extreme wave statistics of irregular waves due to accelerating following current over a submerged bar”. *Journal of Fluid Mechanics* 954, A50.

Zhang, N., Yan, S., Ma, Q., Zhang, Y., and Zheng, X. (2023b). “A numerical study on focused wave interactions with a submerged flexible membrane using SPH”. *ISOPE International Ocean and Polar Engineering Conference*. ISOPE, ISOPE–I–23–170.

Zhang, N., Yan, S., Zheng, X., and Ma, Q. (2020). “A 3D hybrid model coupling SPH and QALE-FEM for simulating nonlinear wave-structure interaction”. *International Journal of Offshore and Polar Engineering* 30.01, pp. 11–19.

Zhang, S., Chen, L., Ning, D., and Teng, B. (2021b). “Multi-Bragg reflections over a periodic submerged structure”. *Proceedings of the 36th International Workshop on Water Waves and Floating Bodies*.

Zheng, Y., Lin, Z., Li, Y., Adcock, T., Li, Y., and Van Den Bremer, T. (2020). “Fully nonlinear simulations of unidirectional extreme waves provoked by strong depth transitions: The effect of slope”. *Physical Review Fluids* 5.6, p. 064804.

Zheng, Z., Li, Y., and Ellingsen, S. Å. (2023). “Statistics of weakly nonlinear waves on currents with strong vertical shear”. *Physical Review Fluids* 8.1, p. 014801.

Zhu, D. and Dong, Y. (2020). “Experimental and 3D numerical investigation of solitary wave forces on coastal bridges”. *Ocean Engineering* 209, p. 107499.